Available online at www.sciencedirect.com

ScienceDirect

Geochimica et Cosmochimica Acta 269 (2020) 63–100

Geochimica et Cosmochimica Acta

www.elsevier.com/locate/gca

Chemical reactions, porosity, and microfracturing in shale during weathering: The effect of erosion rate

Xin Gu [a,⇑], Daniella M. Rempe [b], William E. Dietrich [c], A. Joshua West [d], Teng-Chiu Lin [e], Lixin Jin [f], Susan L. Brantley [g]

[a] Department of Geosciences, The Pennsylvania State University, University Park, PA 16802, USA
[b] Jackson School of Geosciences, University of Texas at Austin, Austin, TX 78712, USA
[c] Department of Earth and Planetary Science, University of California, Berkeley, CA 94709, USA
[d] Department of Earth Sciences, University of Southern California, Los Angeles, CA 90089, USA
[e] Department of Life Science, National Taiwan Normal University, Taipei 11677, Taiwan
[f] Department of Geological Sciences, University of Texas at El Paso, El Paso, TX 79968, USA
[g] Earth and Environmental Systems Institute, Department of Geosciences, The Pennsylvania State University, University Park, PA 16802, USA

Received 2 March 2019; accepted in revised form 28 September 2019; available online 08 October 2019

Abstract

The rate of chemical weathering has been observed to increase with the rate of physical erosion in published comparisons of many catchments, but the mechanisms that couple these processes are not well understood. We investigated this question by examining the chemical weathering and porosity profiles from catchments developed on marine shale located in Pennsylvania, USA (Susquehanna Shale Hills Critical Zone Observatory, SSHCZO); California, USA (Eel River Critical Zone Observatory, ERCZO); and Taiwan (Fushan Experimental Forest). The protolith compositions, protolith porosities, and the depths of regolith at these sites are roughly similar while the catchments are characterized by large differences in erosion rate (1–3 mm yr^{-1} in Fushan $\gg$ 0.2–0.4 mm yr^{-1} in ERCZO $\gg$ 0.01–0.025 mm yr^{-1} in SSHCZO). The natural experiment did not totally isolate erosion as a variable: mean annual precipitation varied along the erosion gradient (4.2 m yr^{-1} in Fushan > 1.9 m yr^{-1} in ERCZO > 1.1 m yr^{-1} in SSHCZO), so the fastest eroding site experiences nearly twice the mean annual temperature of the other two.

Even though erosion rates varied by about 100×, the depth of pyrite and carbonate depletion (defined here as regolith thickness) is roughly the same, consistent with chemical weathering of those minerals keeping up with erosion at the three sites. These minerals were always observed to be the deepest to react, and they reacted until 100% depletion. In two of three of the catchments where borehole observations were available for ridges, these minerals weathered across narrow reaction fronts. On the other hand, for the rock-forming clay mineral chlorite, the depth interval of weathering was wide and the extent of depletion observed at the land surface decreased with increasing erosion/precipitation. Thus, chemical weathering of the clay did not keep pace with erosion rate. But perhaps the biggest difference among the shales is that in the fast-eroding sites, microfractures account for 30–60% of the total porosity while in the slow-eroding shale, dissolution could be directly related to secondary porosity. We argue that the microfractures increase the influx of oxygen at depth and decrease the size of diffusion-limited internal domains of matrix, accelerating weathering of pyrite and carbonate under high erosion-rate conditions. Thus, microfracturing is a process that can couple physical erosion and chemical weathering in shales.

Keywords: Shale; Chemical weathering; Porosity; Erosion; Microfracture

⇑ Corresponding author.
E-mail addresses: xug102@psu.edu (X. Gu), rempe@jsg.utexas.edu (D.M. Rempe), bill@eps.berkeley.edu (W.E. Dietrich), joshwest@usc.edu (A.J. West), tclin@ntnu.edu.tw (T.-C. Lin), ljin2@utep.edu (L. Jin), sxb7@psu.edu (S.L. Brantley).

https://doi.org/10.1016/j.gca.2019.09.044
0016-7037/

1. INTRODUCTION

In general, chemical weathering occurs when CO_2- and O_2-charged meteoric fluids interact with basic, electron-rich rocks. At shallow depths, such reactions are mediated by biota to produce the soils that globally nurture terrestrial ecosystems. Since the 1800s, scientists have studied how weathering transforms rock into regolith, where regolith here is defined as all weathered material (see Brantley and Lebedeva, 2011; Riebe et al., 2017 and references therein). More recently, research has focused on quantifying the rates of weathering for incorporation into mathematical models of regolith formation (e.g., Minasny et al., 2008; Brantley and Lebedeva, 2011; Anderson et al., 2019). The rate of chemical weathering can be quantified from the solute flux (usually at annual to decadal timescales) or from the rate of deepening (advance) of the regolith-protolith interface (usually at geologic timescales). The regolith-protolith interface is typically defined from observations of depletions of elements or transformations of minerals (Brantley and White, 2009). In eroding systems, researchers often argue that weathering advance rates may keep up with rates of erosion so that the thickness of regolith roughly remains constant (e.g., Pavich, 1986; Stallard, 1995; Jacobson et al., 2003; Riebe et al., 2001, 2003; von Blanckenburg et al., 2004; West et al., 2005; Hren et al., 2007; Larsen et al., 2014; Behrens et al., 2015; Emberson et al., 2016). In this paper, we address what mechanisms might cause acceleration of the weathering advance rate for one rock type (shale) when subjected to faster rates of physical erosion.

Fletcher et al. (2006) proposed that weathering and erosion might be coupled through porewater chemistry and oxidation-driven fracturing. Molnar et al. (2007) emphasized tectonic processes that fracture the upper brittle crust in tectonically active areas and accelerate chemical weathering. St Clair et al. (2015) proposed that fractures induced by topographic stress can accelerate the infiltration of rock by meteoric fluids that are not in chemical equilibrium with surrounding rocks, therefore facilitating chemical weathering. Rempe and Dietrich (2014) suggested that chemical weathering is controlled by the slow drainage of groundwater through unaltered rock under hills, and emphasized that channel incision and erosion rate could therefore be coupled to the rate at which the weathering front advances into the fresh bedrock.

One shared aspect of all these models is the importance of matrix and fracture porosity and how it evolves when bedrock is exhumed. This is because porosity affects fluid flow rates and provides the mineral-water interfacial area for weathering reactions (Rossi and Graham, 2010; Jin et al., 2011, 2013; Navarre-Sitchler et al., 2013; Bazilevskaya et al., 2015; Goodfellow et al., 2016). Mineral-water reactions such as dissolution or oxidation of primary minerals can promote fracturing (Eppes and Keanini, 2017). Such reactions also can promote precipitation of secondary clays and Fe (hydr)oxides that seal pores and fractures (Meunier et al., 2007). Many examples of the coupling between weathering and fracturing have been reported in crystalline rocks (see Navarre-Sitchler et al., 2015 and the references therein). However, the relationship between weathering, porosity evolution, and fracturing in fine-grained sedimentary rocks such as shale has not received much attention (with some exceptions including Chigira, 1990; Morin et al., 1997; Oyama and Chigira, 1999; Jin et al., 2013; Worthington et al., 2016; Lerouge et al., 2018).

In this study, we investigated chemical weathering and the development of porosity in shale in three catchments characterized by vastly different erosion rates (Fig. 1): the Susquehanna Shale Hills Critical Zone Observatory (SSHCZO) in central Pennsylvania, USA (Rose Hill Formation), with erosion rates of 0.01–0.025 mm yr^{-1} (West et al., 2013); the Eel River Critical Zone Observatory (ERCZO) in Northern California, USA (Coastal Belt of the Franciscan Formation), with erosion rates of 0.2–0.4 mm yr^{-1} (Fuller et al., 2009); and the Fushan Experimental Forest in northeast Taiwan (Kankou Formation, Oligocene to Miocene), with erosion rates of 1–3 mm yr^{-1} (Siame et al., 2011). In addition to changes in erosion rate, mean annual temperature and rates of precipitation also increased across the three sites, as summarized in Table 1.

We infer that the weathering advance rates also differ at the three sites markedly, and we seek to understand why. For example, the rates of weathering and erosion have been inferred to be within about a factor of 3 of one another in SSHCZO (0.01–0.025 mm yr^{-1}). If a weathering rate of that magnitude was paired with the erosion rate at Fushan (1–3 mm yr^{-1}), no soil would remain after 0.3–1 kyr, assuming the thickness of soil is 1 m. Instead, the residence times of the soil at SSHCZO vary from 12 ky to 43 ky, depending upon landscape position (Ma et al., 2010, 2013; West et al., 2013). In fact, all three shale landscapes are underlain by thick weathered material. Thus, there is an unknown phenomenon that accelerates weathering in the higher eroding sites so that the weathering advance rates at depth can increase until Fushan > ERCZO > SSHCZO. To identify this process, we test the hypothesis that the pore network may control some of the coupling. Specifically, we measure bulk chemical composition and mineralogy to quantify the chemical weathering profiles. In addition, we analyze the very small pores and microfractures and probe the porosity evolution in the shales by using neutron scattering, scanning electron microscopy (SEM), and mercury intrusion porosimetry (MIP).

2. STUDY SITES

Observatory sites are ideal for exploring changes of shale during weathering and their relation to erosion because of the availability of complementary datasets. For this reason, we investigated two shale-dominated observatories that are part of the US Critical Zone Observatory (CZO) network. The third site in Taiwan is not designated as an observatory and does not have the same intensity of observations related to weathering and soil formation, but nonetheless has been well characterized in terms of hydrology, geochemistry, geomorphology, and

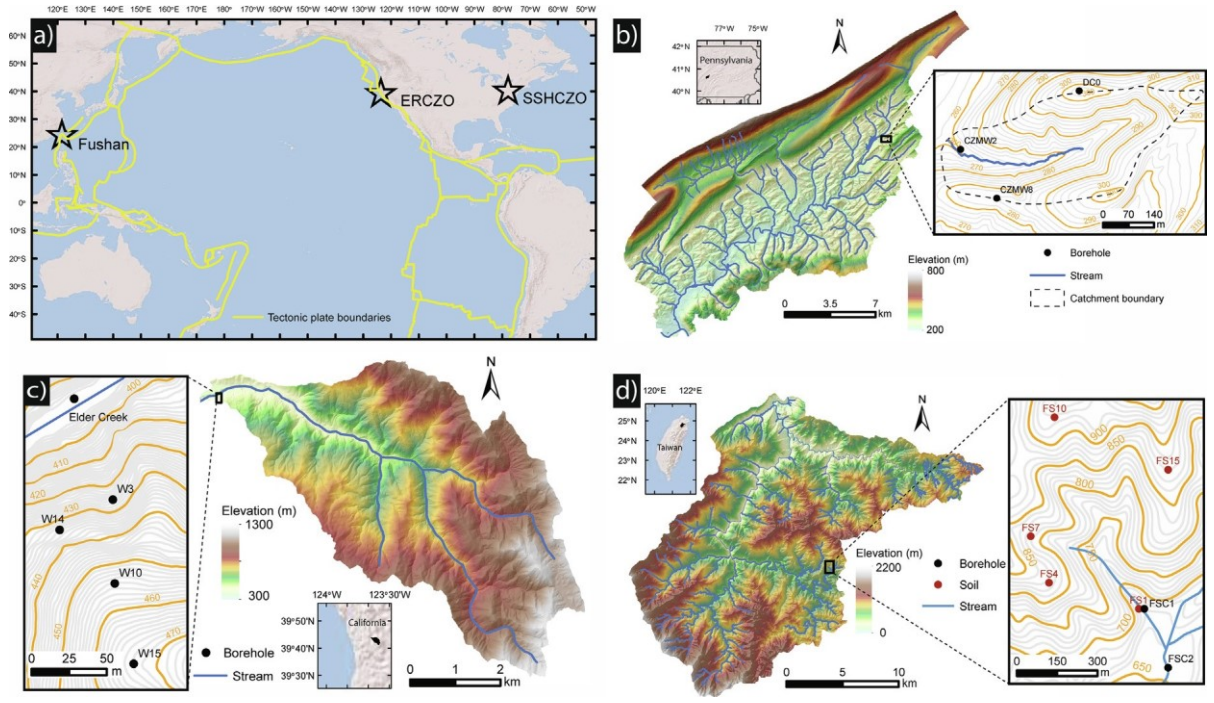

Fig. 1. Map of study sites: Susquehanna Shale Hills Critical Zone Observatory (SSHCZO) in Pennsylvania, USA; Eel River Critical Zone Observatory (ERCZO) in California, USA; Fushan Experimental Forest (Fushan) in northeast Taiwan. a) ERCZO and Fushan are located near tectonic plate boundaries (yellow lines) and have higher erosion rates than SSHCZO. b) The Shale Hills subcatchment (0.08 km^2 area) at SSHCZO is located at the headwater of Shaver's Creek. c) The ''Rivendell" hillslope (0.004 km^2 area) at ERCZO is located near the outlet of the Elder Creek catchment. d) Experimental watershed 1 (0.37 km^2 area) at Fushan is located at the headwater of Hapen Creek, an upstream tributary of the Nanshi River.

ecology to a greater extent that most other locations with similarly high erosion rates. The lithology of the three sites is also similar as discussed further below.

2.1. SSHCZO

The Susquehanna Shale Hills Critical Zone Observatory (SSHCZO) is a >100 km^2 watershed located in the Valley and Ridge physiographic province of the Appalachian Mountains in central Pennsylvania, USA (Fig. 1b). We studied one subcatchment within the observatory known specifically as Shale Hills. The 0.08 km^2 V-shaped forested, soil-mantled Shale Hills catchment has a local relief of 30 m, side slopes with gradients of 8–30°, and an ephemeral stream that flows west-southwest (West et al., 2013). The axis of the catchment is aligned in an east-west orientation. The catchment is underlain by the Rose Hill Formation, a member of the Silurian Clinton Group, which consists primarily of shale with minor interbedded limestone and sandstone units, especially near the outlet of the catchment (Jin et al., 2010; Sullivan et al., 2016). Although the Rose Hill Formation is often considered a ''shale", the lithology has been slightly metamorphosed during burial and exhumation to the extent that pencil cleavage has developed. Sullivan et al. (2016) reports that bedding at SSHCZO is oriented NE-SW, with dip angles ranging from 40° to 88° to the northwest. The climate at SSHCZO is characterized as humid continental: warm to hot summers and cold winters, and well distributed precipitation throughout the year. A mean annual precipitation (MAP) of 107 cm and mean annual air temperature (MAT) of 10 °C was reported at the nearby State College Weather Station (USC00368449 location, NOAA) over the past 30 years.

Rates of weathering, erosion, and exhumation have been estimated for the SSHCZO area. Measurements of meteoric ^{10}Be and uranium disequilibrium isotopes at Shale Hills documented that the long-term average erosion rates on the hillslopes inferred over the 10^4–10^5 yr time scale range from 0.01-0.025 mm yr^{-1} (West et al., 2013) while the rates of production of soil range from 0.015-0.065 mm yr^{-1} (Ma et al., 2010, 2013). These values are similar to rates of Appalachian rock exhumation over the 10^7–10^8 yr time scale (Roden and Miller, 1989; Spotila et al., 2004). These similarities indicate that the central Appalachian landscape, where SSHCZO is located, is characterized by weathering and erosion rates that are roughly equivalent within error. However, variations in regolith thickness and residence time mean that weathering rate is not everywhere equivalent to erosion rate, at least partly because of perturbations during the Last Glacial Maximum (Ma et al., 2010, 2013; West et al., 2013).

In Shale Hills, we collected five core fragments from a 30-m deep borehole (CZMW8) drilled into the southern ridge in 2013 and two rock chips from a soil profile excavated on a ridge in a parallel subcatchment (Missed Grouse Gulch) located ~0.25 km to the north (Fig. S1). Both

Table 1
Catchment characteristics.

Site	Latitude (°)	Longitude (°)	Mouth elevation (m)	Relief (m)	Slope (°)	Bedding Dip (°)	MAT (°C)	MAP (cm)	Climate	E (mm yr^{-1})	Formation
Shale Hills at SSHCZO	N 40.667	W 77.903	297	30	15–20	40–88	10	107	Humid continental	0.01–0.025[a]	Rose Hill Formation
Rivendell at ERCZO	N 39.730	W 123.643	392	78	~30	~90	10	190	Mediterranean	0.2–0.4[b]	Coastal Belt of the Franciscan Complex
Experimental Watershed 1 at Fushan	N 24.761	E 121.555	670	430	~28	~90	18	424	Humid subtropical	1–3[c]	Kankou Formation

[a] Erosion rate (E) estimated from meteoric ^{10}Be measurements (West et al., 2013).
[b] Erosion rate (E) estimated from ^{10}Be measurements (Fuller et al., 2009).
[c] Erosion rate (E) estimated from ^{10}Be measurements in the nearby Lanyang Hsi (Siame et al., 2011).

subcatchments are developed on Rose Hill shale. Cored materials from borehole CZMW8, recovered through wireline coring, were air-dried and stored at room temperature. The pore network of the rock fragments and chips were assessed using neutron scattering, SEM, and MIP. Samples were collected from Missed Grouse Gulch because the soil pits there were excavated to a depth of 1.5 m with a trackhoe, an excavation which was not allowed in the Shale Hills catchment. The two catchments are nonetheless essentially identical, and many aspects of weathering and erosion have been studied in the Missed Grouse as a comparison to Shale Hills (West et al., 2014; Hasenmueller et al., 2017). The bulk chemistry of the samples from the borehole and soil pit have been reported in Sullivan et al. (2016) and Hasenmueller et al. (2017), respectively. Additional geochemical and mineralogical analyses on these samples were measured in this study.

2.2. ERCZO

The Eel River Critical Zone Observatory (ERCZO) site is located within the 17 km^2 Elder Creek watershed, a tributary to the South Fork of the Eel River in Northern California within the steep, forested Northern California Coast Ranges (USA, Fig. 1c). The samples from ERCZO are from an intensively instrumented and sampled hillslope or zero-order catchment named ‘‘Rivendell”. Rivendell is a forested, soil-mantled, unchanneled catchment with a steep north-facing hillslope (~32°) adjacent to Elder Creek. The site extends from Elder Creek (at 392 m above sea level, asl) to 470 m asl at the ridge (Salve et al., 2012). The catchment is underlain by Coastal Belt of the Franciscan Complex, a subduction complex ranging in age from Jurassic to Miocene or younger, which consists primarily of slightly metamorphosed marine argillite with interbedded sandstone deposited as turbidites. The bedding is oriented parallel to the hillslope axis with near-vertical dip. The climate at ERCZO is characterized as Mediterranean, with warm dry summers and cool wet winters. MAP is ~190 cm and MAT is 10 °C (Salve et al., 2012). Fuller et al. (2009) estimated the contemporary basin-averaged erosion rates of Elder Creek are around 0.2 mm yr^{-1}, while Pleistocene erosion rates approached 0.4 mm yr^{-1}. Dated marine terraces at a similar latitude as the Rivendell site indicates uplift rates of approximately 0.4 mm yr^{-1} (Merritts and Bull, 1989).

We selected 64 rock chips and 3 bulk soils from along the full length of five boreholes drilled using a track-mounted rig along the hillslopes at Rivendell in 2007–2010 (Fig. 1c). The rock chips are from three distinct hydrologic zones identified by researchers from ERCZO: the chronically water-unsaturated zone, seasonally satu- rated zone, and chronically saturated zone (Kim et al., 2014). A full description of the boreholes was reported in Rempe (2016).

2.3. Fushan

Experimental Watershed 1 at Fushan Experimental Forest (Fushan) is a catchment located within the Ha-pen Nature Preserve in the Snow Mountain Range of northeastern

Taiwan (Fig. 1d). The 0.37 km^2 catchment is forested and soil-mantled and has steep slopes (~28° on average). The elevation ranges from about 670–1100 m asl (Lin et al., 2011). The catchment is underlain by the Kankou Formation (Eocene to Oligocene age), which consists primarily of metamorphosed marine argillite with interbedded silt and fine sandstone (Lin et al., 1996). At Fushan, bedding is oriented NE-SW, with dip angles ranging from 63° to 88° to the southeast. The climate at Fushan is characterized as humid subtropical, with hot humid summers and cool rainy winters. MAP is 424 cm and MAT is 18 °C (Lin et al., 2011).

Erosion rates estimated from measurements of total suspended load plus bedload trapped in the Fushan watershed weirs between 1998 and 2000 are 0.4 mm yr^{-1} in Watershed 1 (studied here) and 0.9 mm yr^{-1} in the nearby Watershed 2 (Jen et al., 2006). These values are in the same range as erosion rates calculated from ^{10}Be in quartz from river sands in the nearby Lanyang Hsi, of 2 ± 1 mm yr^{-1} (Siame et al., 2011). Exhumation rates (1.6 ± 0.3 mm yr^{-1}) were estimated on the 10^7–10^8 yr time scale from a single sample from a nearby site on the northern margin of the I-Lan Basin using apatite fission-track ages (Clift et al., 2008). In the main Central Range in Taiwan, uplift and exhumation are particularly rapid (in some cases >5 mm yr^{-1}; Hsu et al., 2016), commensurate with very high sediment fluxes (Dadson et al., 2003). Fushan sits to the north of the Central Range, with somewhat slower erosion rates than some parts of the rest of the Central Range because of the dynamics of extension in the Okinawa Backarc Basin and I-lan Plain (Clift et al., 2008). Nonetheless, erosion rates are still very high in the global context.

Considerably fewer samples were available to us from Fushan. We analyzed nine rock chips from drilled borehole FSC1 and the deepest rock chip from borehole FSC2. Both boreholes are 15 m deep and are adjacent to the stream channel (Fig. 1d). A full description of the boreholes was reported in Chang (2000). We also analyzed six rock chips and six bulk soils from a soil pit dug near borehole FSC1 (FS1, Fig. 1d). Nine rock chips were collected in the catchment where visibly unweathered bedrock was exposed, e.g., along the incised bank of the channel in the valley. Bulk soils were also collected via hand augering along ridges (FS4, FS7, FS10, and FS15 in Fig. 1d).

3. MATERIALS AND METHODS

Samples were analyzed by a suite of geochemical and mineralogical measurements as well as porosity measurements. The latter measurements included electron microscopy, neutron scattering, and MIP, as described in the following sections.

3.1. Geochemical and mineralogical characterization

Air-dried rock chips and bulk soils were pulverized using a mortar and pestle to pass through a 100-mesh sieve (<150 μm). Major element chemistry of the pulverized sample was determined on an initial mass of around 0.1 g by lithium metaborate fusion and inductively coupled plasma-atomic emission spectroscopy (ICP-AES; Perkin- Elmer Optima 5300DV ICP-AES) at the Laboratory for Isotopes and Metals in the Environment of the Pennsylva- nia State University. Loss on ignition (LOI) was deter- mined by the difference in sample mass before (initial mass: 1 g) and after combustion at 900 °C for 1 h. The ele- mental loss and gain during weathering was calculated as the mass transfer coefficient:

$$\tau_{j,w} = \frac{C_{j,w} C_{i,p}}{C_{j,p} C_{i,w}} - 1 \qquad (1)$$

where $\tau_{j,w}$ is calculated from the concentration of an element or mineral of interest, $C_{j,w}$, and the concentration of the same element or mineral in the parent (unweathered bedrock, or protolith), $C_{j,p}$, normalized by similar concentrations of an immobile element or mineral (i). For all analyses, chemistry was presented on an ''as received" basis (in other words, not for the ashed sample). The immobile species is generally an element from a highly insoluble mineral (e.g., Zr in zircon or Ti in anatase or rutile). In this study, we used Ti as the immobile element for all three sites. By assuming (i) the parent material is sufficiently homogenous and well characterized, and (ii) species i is immobile, these ''tau" values can be used to quantify the elemental loss or gain: when $\tau = 0$, element j is neither enriched nor depleted with respect to species i in the parent; when $\tau < 0$, the element has been lost relative to immobile species i in parent, and $\tau > 0$ indicates the species has been added to the sample relative to parent material (Brimhall and Dietrich, 1987; Anderson et al., 2002).

Total carbon and sulfur concentrations were determined on pulverized samples (<150 lm) using a LECO SC632 Carbon/Sulfur Determinator. Inorganic carbon concentrations were measured in pulverized samples by reaction with hydrochloric acid (1 N) with subsequent measurement of released CO_2 in headspace on a LI-COR CO_2-H_2O Analyzer (LI-7000) as reported in Bazilevskaya et al. (2015).

Minerals were identified by X-ray diffraction (XRD) of the pulverized samples (<150 lm) with a PANalytical Empryean X-Ray Diffractometer (PANalytical Ltd., The Netherlands) at 45 kV and 40 mA with a Cu Ka radiation at the Material Characterization Laboratory of the Pennsylvania State University. Stepwise scanning measurements were performed at a rate of 4° min^{-1} in the range of 5–70° 2h. The relative mineral percentages were estimated semi-quantitatively using the USGS RockJock program (Eberl, 2003). The clay mineralogies in samples from SSHCZO and ERCZO have been reported by Jin et al. (2010) and Kim et al. (2014), respectively. Thus, only the sample from Fushan was further characterized for clay minerology. Clay and fine-silt fractions (<20 μm) were separated, treated with (i) K saturation with a 1 M KCl solution dried at room temperature and followed by heat treatments at 110 °C, 300 °C, and 550 °C in a muffle furnace; and (ii) Mg saturation with a 1 M $MgCl_2$ solution dried at room temperature followed by treatment with ethylene glycol at 60 °C and analyzed by XRD (Harris and White, 2008).

3.2. Electron microscopy

Representative rocky material from protolith and regolith from each catchment was imaged by scanning electron microscope (SEM) at the Material Characterization Laboratory of the Pennsylvania State University. To prepare sections for SEM imaging, the rock chips were cut using a low-speed diamond saw, polished with sandpaper and diamond paste and mounted on SEM stubs using carbon paste. Several sections were further polished by argon (Ar) beam ion milling (Leica EM TIC 3X) to minimize surface damage. The sections were coated with iridium (~5 nm thick) or carbon (~10 nm thick) to reduce charging. Images with low magnification (<×10,000) were obtained using an Environmental SEM (FEI Quanta 200 or FEI Quanta 250) with an accelerating voltage of 10–15 kV and a spot size of 4 to 5 in backscatter mode. Selected areas were probed by energy dispersive X-ray spectra (EDS) on the SEM with an accelerating voltage of 15–20 kV and a spot size of 6 to 7 using an Oxford EDS detector. The images at high magnification (>×10,000) were collected by a field-emission SEM (FEI Nova NanoSEM 630) with an accelerating voltage of 8–10 kV, landing energy in the range of 4–5 kV, with a spot size of 2 to 3 using a vCD detector (low-voltage, high-contrast detector).

3.3. Neutron scattering

Our work emphasizes the contribution of porosity measurable at the scale of thin sections. Although larger fractures with lengths of cm to tens of cm are commonly observed in core materials and in boreholes scanned by optical televiewer (see for example, Sullivan et al., 2016), we do not discuss those here. Here we use the term pore very inclusively – recognizing that pores in thin sections with high aspect ratio may best be described as microfractures.

Neutron scattering is the primary tool used here because of the very small nature of pores in shale (Anovitz and Cole, 2015). For this scattering, a sample thin section is placed in a beam of neutrons and neutrons are scattered by interaction with nuclei. The intensity of the elastic scattered neutrons, $I(Q)$, is measured as a function of the momentum transfer, Q, which is defined by $Q = 4\pi\lambda^{-1}\sin(\theta/2)$. Here λ is the incident wavelength and θ is the scattering angle, and the measured dimensions are in the order of Q^{-1}. In rock samples, the scattering mainly occurs at pore-grain interfaces (Radlinski, 2006); thus, a statistically representative interpretation of pore features (i.e. fractal characteristics, surface area, pore size distribution) can be derived from $I(Q)$ profiles (Mildner and Hall, 1986; Allen, 1991; Hinde, 2004).

We used contrast matching on both raw and epoxy-impregnated thin sections to assess fluid-accessible porosity in shale (see Appendix A). The epoxy-impregnated thin sections were prepared by Spectrum Petrographics using epoxy with very low viscosity (Epotek 301) under vacuum after drying the specimen at 60 °C overnight. Thin sections were cut on raw or epoxy-impregnated samples through the center of the rock chips perpendicular to the bedding plane, mounted on quartz slides, and double polished to around 150 μm thickness. The actual thickness was measured by a digital micrometer (Mitutoyo, USA).

To complete the contrast-matching experiment, thin-sectioned rock samples were detached from the quartz slides through acetone soaking. After drying at 60 °C overnight, the thin sections were saturated in a contrast-matching fluid (an H_2O-D_2O mixture) in a quartz-sample-quartz ''gasketted sandwich" for at least one week. Excess liquid in the sandwich was removed through a syringe prior to neutron scattering experiments. The SLD values were calculated using the NIST neutron activation and scattering calculator (https://www.ncnr.nist.gov/resources/activation/) based on the mineral composition estimated by XRD.

The small-angle neutron scattering (SANS) and ultra-small-angle neutron scattering (USANS) measurements were performed at the National Institute of Standards and Technology (NIST) Center for Neutron Research (NCNR). SANS data were collected in three different configurations, with the sample–detector distances of 1 m and 4 m using 8.4 Å neutrons, and at 13 m with lenses using 8.09 Å neutrons on NG3 or NGB 30 m SANS instrument (Glinka et al., 1998). USANS data were collected using a double crystal diffractometer with a wavelength $\lambda = 3.48$ Å on BT5 instrument (Barker et al., 2005). The SANS and USANS measurements were conducted by placing the thin sections normal to the incident beam at ambient conditions. The cross section was defined by cadmium plates with 12.7 mm (1/2 inch) or 6.35 mm (1/4 inch) diameter depending on the size of thin sections.

Both sets of measurements were reduced to an absolute basis using NIST procedure (Kline, 2006). The scattering from shale cut perpendicular to bedding produces azimuthally asymmetric and elliptical contours on the detector. We used recently developed methods to correct the USANS measurements (Gu and Mildner, 2016) and calculate the entire scattering (i.e. scattering averaged on all orientations) from the anisotropic pattern (Gu and Mildner, 2018).

We used the polydisperse spherical pore (PDSP) model to determine the porosity and the pore size distribution (PSD) from the scattering data (Hinde, 2004; Gu et al., 2015). The PSD is the relative fraction of pores within a narrow range of pore dimension. The pore geometry is far more complex than the sphere model allows, and thus the pore dimensions reported here are approximations. However, as all the scattering data were treated through the same procedure, the systematic changes in the PSD are considered robust. To calculate PSDs, the intensity-momentum data were fit to the PDSP model to calculate porosity (ϕ) versus the dimension of the scatterer (D, at log scale). PSDs are plotted as logarithmically differential pore volume distribution ($\frac{d\phi}{d\log(D)}$ vs. $\log(D)$) because of the large range of pore size.

The pore space of microfracture, which is defined as fractures less than 0.1 mm wide and up to a few millimeters in length (Anders et al., 2014), was also estimated on back-scattered electron (BSE) images (~10 images per sample with ~70× to ~500× magnification) as the percentage of the microfracture area normalized to the total area of cross

section of thin sections. The microfracture area was calculated as a product of total fracture length in the cross section and the mean aperture of fractures measured using ImageJ software (Abramoff et al., 2004).

3.4. Mercury intrusion porosimetry

Porosity, surface area, and pore throat distribution of selected shale samples from Shale Hills and Fushan were also measured by MIP with a Micromeritics Auto Pore V 9620 mercury porosimeter (Micromeritics, Norcross, GA) using a maximum pressure of 413.7 MPa at the Material Characterization Laboratory of the Pennsylvania State University. MIP of the samples from ERCZO were conducted by a commercial laboratory (Thermo Fisher) with maximum pressure 200 MPa. Prior to measurements, the rock chips were gently crushed to centimeter size, heated at 105 °C overnight and then degassed at 6.6 Pa evacuation pressure for 30 minutes to remove moisture. The bulk volume was measured through mercury immersion at 3.7 kPa, and the pore volume was measured by intruded mercury at discrete pressure steps up to maximum pressure. The pore throat size was calculated through Washburn's equation:

$$r = \frac{2c\cos h}{P} \quad (2)$$

where r is the corresponding pore throat radius, P is the capillary pressure, c is the surface tension of mercury, and h is the contact angle between mercury and the porous medium. We assumed $h = 130$ and $c = 0.485$ N m^{-1}. These calculations resulted in a pore throat range from 3 nm to 330 mm. The breakthrough capillary pressure, at which a continuous filament of mercury breaks through the medium, was estimated by identifying the inflection point on the cumulative mercury intrusion (or cumulative porosity) versus pressure curve (Thompson et al., 1987).

The permeability was estimated through an empirical equation (Katz and Thompson, 1985; Comisky et al., 2007; Nelson, 2009):

$$k \approx 4.48 d_c^2 \phi^2 \quad (3)$$

where k is the permeability in millidarcies, d_c is the pore throat size in micrometers corresponding to the breakthrough capillary pressure calculated from Eq. (2), and ϕ is the porosity determined by MIP. Eq. (3) is only used to estimate approximate permeability values to show how changes in pore network structure might affect permeability in regolith as compared to protolith. It is well known that such empirical equations generally do not accurately reflect permeability.

4. RESULTS

4.1. Distribution and characteristics of regolith

SSHCZO. Some of the observations summarized for SSHCZO are derived from earlier publications. Recognizing that the definition of soil is not universally agreed upon, but generally includes all material that is mobile over some time scale, we defined soil at Shale Hills as material that can be augered by hand. The thickness of hand-augerable material varies from 0.2–0.3 m on the ridge to 1.5–3 m in the valley (Jin et al., 2010). The layer below soil is weathered and fractured bedrock. Previously, all the rocky material below the soil that was fractured and weathered was referred to as ''saprock" by Jin et al. (2011), and saprolite is not observed at SSHCZO. Beneath the saprock is protolith: protolith is largely unaltered although cores returned from drilling show occasional fractures with oxidation halos.

The regolith-protolith interface is defined as where the rock begins to chemically lose a detectable proportion of its pyrite and/or carbonate. The water table varies in depth across the catchment (Brantley et al., 2013; Sullivan et al., 2016). At the north and south ridge boreholes, the water table is around 20–25 mbls (meters below the land surface) or 15–20 mbls respectively, whereas under the valley the water table ranges from above the land surface (i.e. in the creek) or to depths of around 0.5–1.5 mbls during the dry season. Under the ridge, the depth of the regolith-protolith interface is 1–2 m above the water table, while under the valley, the depth of the regolith-protolith interface is 6–7 m deeper than the water table. Throughout the catchment, the top layer of weathered rock (saprock) is highly fractured (typically to depths of 5–8 mbls), and most fractures are aligned parallel to bedding, as imaged in the borehole walls scanned by optical televiewer (Sullivan et al., 2016). The depth interval of seasonal fluctuation of the water table varies from 1-3 m under the ridge to 0.5–1.5 m under the valley.

ERCZO. Four layers have been identified to characterize the weathered profiles at ERCZO from land surface to depth: soil, saprolite, weathered bedrock, and protolith (Rempe, 2016). The soil thickness generally ranges between 0.3 m and 0.5 m and does not exceed 0.75 m across the site. The saprolite (also identified as the C-horizon) exhibits remnant structures of bedrock (i.e. bedding), but is soil-like. The saprolite is mechanically weak (can be excavated with a shovel) and contains significant soil particles in fractures. The saprolite thickness varies from 0.25 m to 4.5 m and transitions to weathered bedrock that consists of matrix blocks bounded by fractures of varying sizes. The rock material around these fractures is visually observed to have been oxidized. The thickness of weathered and fractured bedrock increases upslope, ranging from 1.75 m to 19.25 m.

At ERCZO, the transition from weathered to fresh bedrock has been identified as the point where oxidation along most fracture surfaces can no longer be observed visually. This roughly corresponds to the inferred transition from the seasonally water-saturated to the chronically-saturated zone. The depth interval representing the seasonal fluctuation of the water table varies from 2 m to 20 m and is larger upslope than at the lower portions of the hillslope. Despite the long dry season at ERCZO, a large amount of water is stored as seasonally exchanged rock moisture mainly in saprolite and weathered bedrock: the annual average rock moisture storage across the entire hillslope is 284 mm (Rempe, 2016; Rempe and Dietrich, 2018).

Fushan. Much less information about regolith structure is available for the Fushan site. However, it is known that

the thickness of soil varies from 0.4-1.0 m across the site and varies roughly inversely with the slope gradient (Lin et al., 1996). Two boreholes in the valley (FSC1 and FSC2, Fig. 1d) reveal a highly weathered, highly fractured, brownish rock material at depths of around 12–13 mbls, beneath which is a less-weathered, less-fractured, black-appearing shale. The water table near the valley is shallower and shows less fluctuation (1.4–3.2 mbls) than the water tables observed upslope (4.3–7.5 mbls) (Chang, 2000). As discussed below, most boreholes were not drilled deep enough to intersect parent material. However, in the bedrock exposures that were observed in the channel, the blacker shale containing higher organic carbon was collected as the least-weathered samples, i.e., the samples that most resembled parent.

4.2. Observations of protolith

The bulk chemistry and minerology of the three shale formations are discussed in Appendix B. In this section, we emphasize the mineral composition and fabric of shale protolith at microscopic scale based on SEM imaging and X-ray elemental mapping.

SSHCZO. The protolith from SSHCZO consists mostly of discrete, silt-sized grains of quartz, chlorite, plagioclase (mainly albite) and other minerals (carbonate, apatite, pyrite, Ti oxides) embedded in a matrix of illite (Fig. 2a). Most quartz, chlorite and plagioclase grains are 1–10 μm in size (Fig. 2a), while a few quartz grains larger than 10 μm (up to 50 μm) were observed. Most pores are elongated or wedge shaped but almost no microfractures are observed in the protolith. The pores are located both along the boundary of silt-sized grains (marked by yellow arrow in Fig. 2b) and within the illite matrix (marked by white arrow in Fig. 2c). The geometry of pores is thus defined by the arrangement of clay aggregates and the angular shape of silt-sized grains. Micron-sized pores were more commonly observed along rigid grains, especially of plagioclase. These pores appear to have initiated at smaller pores and then propagated along weak contacts at the rigid grain-illite matrix interface, as expected for a shale experiencing dilatancy during unloading (Desbois et al., 2017). Presumably, pores along rigid grains could be precursors of the types of microfractures that are observed in the ERCZO and Fushan shales and described below; however, the pores in SSHCZO are typically less than 5 μm in length and generally do not propagate through the illite matrix.

ERCZO. XRD documents that the shale from ERCZO contains 10 times the percentage of plagioclase as compared to shale from SSHCZO and 1.5 times the percentage in Fushan (Table 2). Unlike the shale from SSHCZO where illite is well-dispersed throughout the matrix, illite at ERCZO often occurs as discrete particles or flakes that are microns to tens of microns in size (Fig. 2d). In the shale from ERCZO, most quartz, chlorite and plagioclase are 5–20 μm in size (Fig. 2d), and micron-sized, wedge-shaped pores are located along these grains (marked by yellow arrow in Fig. 2e). In contrast to the X-ray elemental maps for Shale Hills, some of those for ERCZO are imaged without a distinctive color, indicating the existence of very fine-grained particles. These particles are visible under high resolution SEM and commonly contain intercrystalline pores (Fig. 2f).

Fushan. As discussed in the next section and Appendix B, a protolith sample is not available at Fushan. To characterize the texture, we chose the bottom-most sample from the borehole near the valley (FSC1 in Fig. 1d). Like ERCZO, the shale from Fushan contains a large amount of plagioclase (11 wt.% as determined by XRD, as compared to 24 wt.% at ERCZO and just 2 wt.% at SSHCZO, Table 2). Most plagioclase grains are 10–30 μm in size, and most quartz and chlorite are 3–20 μm in size (Fig. 2g). The structure of the illite matrix of the shale at Fushan (Fig. 2g) is similar to that at SSHCZO (Fig. 2a). The amount of illite at Fushan (33 wt.% determined by XRD, Table 2) is lower than that at SSHCZO (42 wt.% determined by XRD, Table 2) but higher than the 16 wt.% value observed at ERCZO. Micron-sized, angular-shaped pores were commonly observed in thin section of protolith from Fushan (marked by brown arrow in Fig. 2h, 2i). These pores were likely related to dissolution of carbonate (see Appendix B for details), attesting to the fact that our sample of ‘‘parent” was not truly unaltered.

4.3. Geochemical and mineralogical changes during shale weathering

SSHCZO. The weathering profiles at SSHCZO are well described (Jin et al., 2010; Brantley et al., 2013; Sullivan et al., 2016; Hasenmueller et al., 2017). The deepest reactions under the northern ridge are pyrite oxidation and carbonate dissolution, which coincide roughly with the water table, while near the valley the pyrite oxidation front is deeper than the water table (Jin et al., 2010; Brantley et al., 2013). The pyrite oxidation front has been inferred both from the loss of total sulfur and because pyrite, sometimes observed under SEM as framboids in the protolith, is never observed above the oxidation front in the saprock. Instead, in the oxidized samples, Fe (hydr)oxide pseudomorphs after pyrite are observed (Fig. 3, Appendix C). No sulfate mineral was observed under SEM at any of the three sites, except rare occurrences of accessory barite at SSHCZO.

The carbonate front, defined by the concentration profile of inorganic carbon (IC) in borehole CZMW8 (the southern ridge), also is co-located near the pyrite front. Ca depletes at that depth but the depletion front is less distinctive than that of pyrite (Fig. 4) as noted previously by Sullivan et al. (2016). This lack of clear Ca depletion is attributed to the inference that only 40% of Ca resides in $CaCO_3$ in this carbonate-poor part of the watershed, while the rest is present in plagioclase or clay minerals (a part of Ca dissolved from carbonate could also have been retained in clay minerals by cation exchange). Variations in carbonate minerals in the protolith are expected given the sedimentary layering in the catchment (see, for example, the Ca-rich layer at about 6 mbls in the borehole near the catchment outlet, CZMW2, in Fig. 4). In general, the carbonate content of the protolith increases toward the outlet of the catchment (Sullivan et al., 2016).

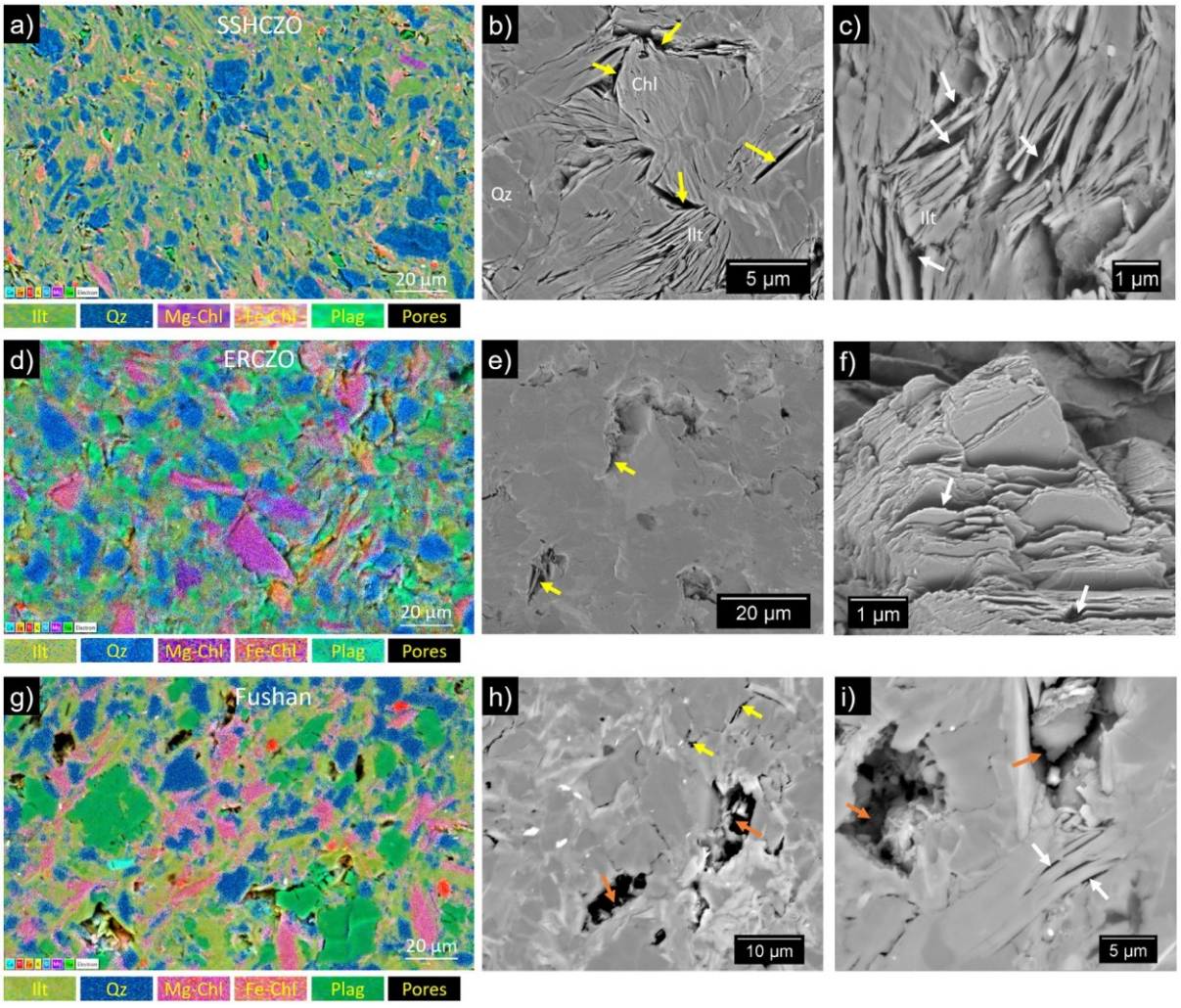

Fig. 2. X-ray elemental maps (a, d, g) and BSE images (b, c, e, f, h, i) of argon-ion-milled sections of unweathered shale from SSHCZO (borehole CZMW8, 23.8 mbls, the top panels a-c), ERCZO (ERCZO_W10-75, 22.9 mbls, the middle panels d-f) and Fushan (Fushan_FSC1_2, 14.8 mbls, the bottom panels g-i). Images display the mineral fabric (spatial distribution and orientation) and pore morphology. The elemental map reflects a mixed backscattered electron and energy-dispersive spectroscopy signal. The small pores (<10 nm) observable under SEM are mainly intercrystalline or intracrystalline within phyllosilicates (white arrows). Larger pores are commonly observed along the boundary between silt-sized grains (yellow arrows). Dissolution features are observed in shale from Fushan (brown arrows). Color legend in left corner of elemental panels reports the dominant element. These data were then interpreted to indicate dominant minerals as shown: Ilt: illite, Qz: quartz, Mg-Chl: Mg-rich chlorite, Fe-Chl: Fe-rich chlorite, Plag: plagioclase.

Compared to the sharp depletion of pyrite and carbonate (represented by sulfur and inorganic carbon content, respectively), depletions of chlorite, plagioclase, and illite (represented by Mg, Na, and K, respectively) occur much more gradually across depth (chlorite, plagioclase) or much closer (illite) to the land surface, as described below (Fig. 4).

Depletion of chlorite has been attributed to vermiculitization through oxidative dissolution (Sullivan et al., 2016), and the weathering products of chlorite appear to be mixed-layer chlorite-vermiculite and/or hydroxy-interlayered vermiculite, or mixtures of these phases (Jin et al., 2010). The degree of vermiculitization of chlorite was semi-quantitatively estimated through the relative intensities of the (0 0 2) reflection at ~7.1 Å and (0 0 1) reflection at 14.1–14.3 Å of chlorite (Weaver, 1955; Rich, 1968). The possible interference of the estimation from the 001 reflection of kaolinite at 7 Å can be neglected (Rich, 1968) because the concentration of kaolinite is low throughout the whole profile at SSHCZO (Table 2). The degree of vermiculitization increases sharply at the pyrite oxidation front (Fig. 4). The Mg:Al ratio of ‘‘chlorite” (here the quotation marks refer to true chlorite as well as the weathering products of chlorite) grains determined by SEM-EDS decreases during weathering (Fig. S2a), consistent with loss of Mg from chlorite vermiculitization/dissolution. We infer that chlorite becomes fully vermiculitized in the soil layer at least in the upper hillslopes since oxidation of the ferrous iron in silicates (mostly observed in chlorite) goes to >90% completion in the soil layer there (Yesavage et al., 2012; Sullivan et al., 2016). The total amounts of chlorite

Table 2
Semi-quantitative mineralogy for samples from the three catchments measured by XRD.[a]

Sample Type	Sample ID	Depth (mbls)	Qz	Ill	Plag	Chl (total)	Carb	Kln	Sme	Fe (hydr) oxides	Other	C-V
Bulk soil from a soil pit under ridge at SSHCZO	SSHCZO_RT-A-3	0.05	46	30	1	9	BDL[b]	8	NS[c]	3	4	0.3
	SSHCZO_RT-C-3	0.3	51	32	1	7	BDL	4	NS	2	3	0.6
Rock chip from a soil pit under ridge at SSHCZO	SSHCZO_RT-50	0.5	32	51	2	10	BDL	BDL	NS	1	4	0.6
	SSHCZO_RT-130	1.3	36	46	1	12	BDL	BDL	NS	1	4	0.6
Bulk soil from borehole CZMW8 at SSHCZO	SSHCZO_CZMW8-0-21in	0.3	44	39	1	11	BDL	1	NS	1	3	0.8
Rock chip from borehole CZMW8 at SSHCZO	SSHCZO_CZMW8-21in-4ft	0.9	41	42	1	12	BDL	1	NS	1	2	0.6
	SSHCZO_CZMW8-19-21ft	5.9	35	43	2	15	BDL	BDL	NS	1	4	1.0
	SSHCZO_CZMW8-27-28ft	8.4	36	47	1	11	BDL	1	NS	1	3	0.8
	SSHCZO_CZMW8-30ft	9.2	35	45	1	14	BDL	2	NS	BDL	3	0.8
	SSHCZO_CZMW8-39-40ft	12	34	46	BDL	15	BDL	3	NS	1	1	0.9
	SSHCZO_CZMW8-50ft	15.4	37	43	1	16	BDL	1	NS	BDL	2	1.8
	SSHCZO_CZMW8-53ft	16.4	31	46	2	19	BDL	1	NS	BDL	2	3.7
	SSHCZO_CZMW8-61-62ft	18.8	33	42	3	16	BDL	BDL	NS	BDL	6	5.0
	SSHCZO_CZMW8-70-71ft	21.5	34	46	1	15	BDL	BDL	NS	BDL	4	2.2
	SSHCZO_CZMW8-95ft	29	38	38	4	17	BDL	1	NS	BDL	3	5.1
	SSHCZO_CZMW8-100-101ft	30.6	33	44	2	16	BDL	BDL	NS	BDL	5	4.5
Rock chip from borehole CZMW2 at SSHCZO	SSHCZO_CZMW2-3-4ft	1.1	39	37	2	10	1	4	NS	3	4	0.8
	SSHCZO_CZMW2-7-8ft	2.3	35	34	2	14	4	6	NS	5	2	1.3
	SSHCZO_CZMW2-12-13ft	3.8	41	37	2	11	1	3	NS	2	4	1.7
	SSHCZO_CZMW2-21-22ft	6.6	27	33	1	15	20	BDL	NS	2	3	4.5
	SSHCZO_CZMW2-22-33ft	6.9	34	41	2	14	3	1	NS	1	5	4.5
	SSHCZO_CZMW2-32-33ft	9.9	33	43	1	15	5	BDL	NS	BDL	3	4.9
	SSHCZO_CZMW2-42-43ft	13	33	41	1	15	5	BDL	NS	BDL	4	5.1
	SSHCZO_CZMW2-47-48ft	14.5	29	41	3	15	4	BDL	NS	BDL	8	5.3
Parent of SSHCZO[d]			36 (7)	42 (4)	2 (1)	16 (1)	3.3 (2.9)	BDL				4.5 (1.0)
Bulk soil from borehole W3 at ERCZO	ERCZO_W3-soil	0.3	28	12	32	18	BDL	2	7	1	1	0.8
	ERCZO_W3-2	0.7	27	17	14	19	BDL	4	17	1	1	0.7
Rock chip from borehole W3 at ERCZO	ERCZO_W3-6	1.8	27	17	21	22	BDL	3	7	1	1	0.7
	ERCZO_W3-12	3.7	29	16	21	19	BDL	4	10	BDL	2	0.4
	ERCZO_W3-19	5.9	24	18	16	19	BDL	5	18	1	1	0.3
	ERCZO_W3-25	7.6	24	15	19	21	1	2	15	BDL	2	3.2
	ERCZO_W3-35	10.7	25	15	25	20	2	2	9	BDL	2	3.8
Rock chip from a soil pit near borehole W10 at ERCZO	ERCZO_W10-2	0.5	30	14	13	20	BDL	2	19	1	1	1.2

Rock chip from borehole W10 at ERCZO	ERCZO_W10-17	5.2	27	18	13	21	BDL	5	15	BDL	1	1.1
	ERCZO_W10-26	7.9	20	23	19	24	BDL	BDL	10	1	3	0.3
	ERCZO_W10-35	10.7	28	13	24	21	BDL	4	10	BDL	1	0.5
	ERCZO_W10-45	13.7	22	16	23	19	BDL	4	13	1	1	0.5
	ERCZO_W10-50	15.2	23	17	23	19	BDL	4	11	BDL	2	1.4
	ERCZO_W10-55	16.8	24	15	27	20	BDL	2	10	BDL	2	3.4
	ERCZO_W10-70	21.3	25	15	20	20	3	2	11	BDL	4	3.8
	ERCZO_W10-75	22.9	25	17	26	20	BDL	2	8	BDL	3	2.9
Rock chip from borehole W14 at ERCZO	ERCZO_W14-5	2.7	26	17	14	20	BDL	4	16	1	1	0.7
	ERCZO_W14-16	4.9	21	16	22	20	BDL	4	16	1	1	0.3
	ERCZO_W14-30	9.1	25	18	22	19	BDL	2	14	1	1	0.3
	ERCZO_W14-45	13.7	24	17	22	21	BDL	2	12	1	1	0.5
	ERCZO_W14-60	18.3	26	16	20	21	BDL	4	13	1	1	0.6
	ERCZO_W14-75	22.9	24	17	29	20	2	BDL	7	BDL	2	3.8
Bulk soil from borehole W15 at ERCZO	ERCZO_W15-soil	0.1	34	7	20	15	BDL	5	17	1	2	0.4
Rock chip from borehole W15 at ERCZO	ERCZO_W15-2	0.5	29	7	19	13	BDL	10	15	1	6	0.2
	ERCZO_W15-31	9.4	24	16	22	23	BDL	1	13	1	1	1.2
	ERCZO_W15-16	12.3	27	5	30	13	BDL	9	10	1	5	0.5
	ERCZO_W15-66	20.3	26	18	19	23	BDL	1	13	BDL	1	1.4
	ERCZO_W15-20	22.9	26	17	15	25	BDL	4	12	BDL	1	3.5
	ERCZO_W15-85	25.9	28	22	18	20	BDL	4	7	BDL	2	3.7
	ERCZO_W15-22	34.1	23	22	21	21	1	BDL	8	BDL	4	3.3
Rock chip from borehole Elder Creek at ERCZO	ERCZO_Elder Crk 19–22 in	0.5	27	12	24	21	1	2	12	BDL	1	4.3
	ERCZO_Elder Crk 6–7 ft	2.0	25	15	27	18	2	2	10	BDL	1	3.5
Parent of ERCZO[e]			25 (1)	16 (3)	24 (3)	20 (1)	1.3 (0.9)	1.7 (0.9)	10 (2)			3.4 (0.7)
Rock chip from soil core FS1 at Fushan	Fushan_FS1O	0.05	46	31	3	17	BDL	2	NS	1	1	2.0
	Fushan_FS1A	0.25	50	31	1	15	BDL	2	NS	1	2	1.9
	Fushan_FS1C	1	44	34	2	17	BDL	1	NS	1	2	1.7
	Fushan_FS1R	1.4	45	33	3	17	BDL	BDL	NS	1	1	2.8
Rock chip from borehole FSC1 at Fushan	Fushan_FSC1_16	1.5	42	34	5	16	BDL	2	NS	BDL	1	1.5
	Fushan_FSC1_14	3.4	33	32	8	26	BDL	BDL	NS	BDL	1	2.7
	Fushan_FSC1_13	4.4	87	13	BDL	BDL	BDL	BDL	NS	BDL		
	Fushan_FSC1_12	5.5	43	27	13	16	BDL	1	NS	BDL	1	2.0
	Fushan_FSC1_10	7.35	44	26	6	18	BDL	4	NS	1	1	1.3
	Fushan_FSC1_8	9.4	40	34	4	18	BDL	3	NS	1	1	1.3
	Fushan_FSC1_6	11.5	30	BDL	2	55	BDL	4	NS	1	8	2.2
	Fushan_FSC1_4	13.4	35	32	10	21	BDL	BDL	NS	BDL	1	2.5
	Fushan_FSC1_2	14.8	38	28	14	19	BDL	BDL	NS	BDL	1	2.7

(*continued on next page*)

Table 2 (*continued*)

Sample Type	Sample ID	Depth (mbls)	Qz	Ill	Plag	Chl (total)	Carb	Kln	Sme	Fe (hydr) oxides	Other	C-V
Outcrop at Fushan	Fushan_FSR1		42	24	17	15	1	BDL	NS	BDL	1	3.1
	Fushan_FSR2		30	38	6	24	BDL	2	NS	BDL	1	1.3
	Fushan_FSR3		31	34	9	22	BDL	2	NS	1	1	1.7
	Fushan_FSR4		35	32	13	19	BDL	BDL	NS	1	1	1.8
	Fushan_FSR6		35	32	11	20	BDL	BDL	NS	1	1	1.8
	Fushan_FSR7		32	37	10	20	BDL	BDL	NS	BDL	1	2.0
	Fushan_FSR8		34	29	17	18	BDL	BDL	NS	1	1	2.2
	Fushan_FSR10		36	32	12	20	BDL	BDL	NS	1	1	2.1
	Fushan_FSR12		34	37	7	21	BDL	BDL	NS	1	1	1.6
Parent of Fushan[f]			34 (3)	33 (4)	11 (4)	20 (2)	1	BDL				1.9 (0.5)

[a] Weight percentage of minerals were determined by Rockjock and normalized to 100% (Eberl, 2003). Mineral codes as follows: Qz (quartz), Ill (illite), PLag (plagioclase), Chl (including chlorite and vermiculite), Cal (calcite), Kln (kaolinite), and Sme (smectite).

[b] Concentration lower than 0.5 wt.% was marked as below detection limit (BDL).

[c] Smectite was not selected (NS) because the swelling mineral was not detected or too low to quantify through the ethylene glycol test on clay and fine-slit fractions.

[d] The parent concentration was averaged through protolith (n = 12) from three boreholes (DC1, CZMW2, and CZMW8) across the catchment. The mineral composition of samples from DC1 and CZMW2 were reported by Jin et al. (2010) and Brantley et al. (2013). The quoted uncertainty is one standard deviation from the mean.

[e] The parent at ERCZO was the average of the protolith from five bore holes (W3, W10, W14, W15, and Elder Creek). The quoted uncertainty is one standard deviation from the mean.

[f] The parent at Fushan was averaged over shale sample from outcrops where visibly unweathered bedrock was exposed. The parent concentration of carbonate was estimated from the outcrop sample (Fushan_FSR1, see Appendix B). The quoted uncertainty is one standard deviation from the mean.

and vermiculite determined by XRD gradually decreases toward the land surface, consistent with ongoing dissolution of ‘‘chlorite” (Table 2).

Illite shows little to no depletion in the saprock but becomes significantly depleted in the soil (Fig. S3). The concentrations of organic carbon (OC) in the protolith and saprock at SSHCZO are close to the detection limit (0.08 wt.%) of the LECO Carbon/Sulfur Determinator (Table S1).

ERCZO. Similar to SSHCZO, the deepest reactions at ERCZO are pyrite oxidation and carbonate dissolution (Fig. 5). Under the hill slopes at ERCZO and ridges at SSHCZO, these reaction fronts roughly coincide with the depth intervals of the fluctuating water table. Like the SSHCZO, the pyrite oxidation front has been inferred both from the loss of total sulfur and because pyrite is observed under SEM as framboids at depth whereas, above the oxidation front, no pyrite framboids are observed. Instead, in the oxidized samples, Fe (hydr)oxide pseudomorphs after pyrite are observed (Fig. 3, Appendix C).

Calcium (Ca) and inorganic carbon (IC) both show a sharp depletion at the same depth and are thus inferred to reflect the dissolution of carbonate. Ca is not depleted to the same extent as IC: the depletion in Ca continues toward the surface beyond the carbonate dissolution zone (Fig. 5). The rest of the Ca resides in other Ca-bearing minerals such as apatite, Ca adsorbed on clay minerals (Kim et al., 2014) and Ca in plagioclase that remain in the weathering rock until dissolution commences at shallower depths than carbonate. Loss of plagioclase, which is documented in depletion fronts of Na in three profiles (not observed in W15), generally proceeds to a depletion extent at the land surface that is similar to that observed at SSHCZO. As is also observed at SSHCZO, vermiculitization of chlorite initiates at the same depth as pyrite oxidation (Fig. 5). However, the extent of dissolution of chlorite/vermiculite is more limited in ERCZO than in SSHCZO, since the total amounts of chlorite and vermiculite remain almost constant as a function of depth in the ERCZO profiles determined by XRD (Table 2). Similar to SSHCZO, illite shows depletion in the bulk soil at ERCZO (Fig. 5, Table 2). The concentrations of OC start at approximately 0.7 ± 0.1 wt.% in protolith and do not show a clear trend with depth (Table 3).

Finally, samples from borehole W15 exhibit a greater variation in composition than other boreholes at ERCZO at the depths inferred to represent protolith. This is especially true with respect to Na and Ca. For example, in Fig. 5, several zones of the material from depths inferred to represent protolith in W15 are enriched in plagioclase but depleted in clay minerals and Ti. These zones are associated with bedrock heterogeneity and the presence of small interbeds of sandstone within the turbidite sequence.

Fushan. The small sample set and high variability in parent at Fushan precludes definitive interpretations. However, the carbonate content of the one sample of outcrop material was larger than every other sample (Appendix B), and carbonate dissolution features (as shown in Fig. 2) were observed in all samples except the outcrop sample (Fushan_FSR1). We therefore assumed that the parent material for all samples originally contained the same

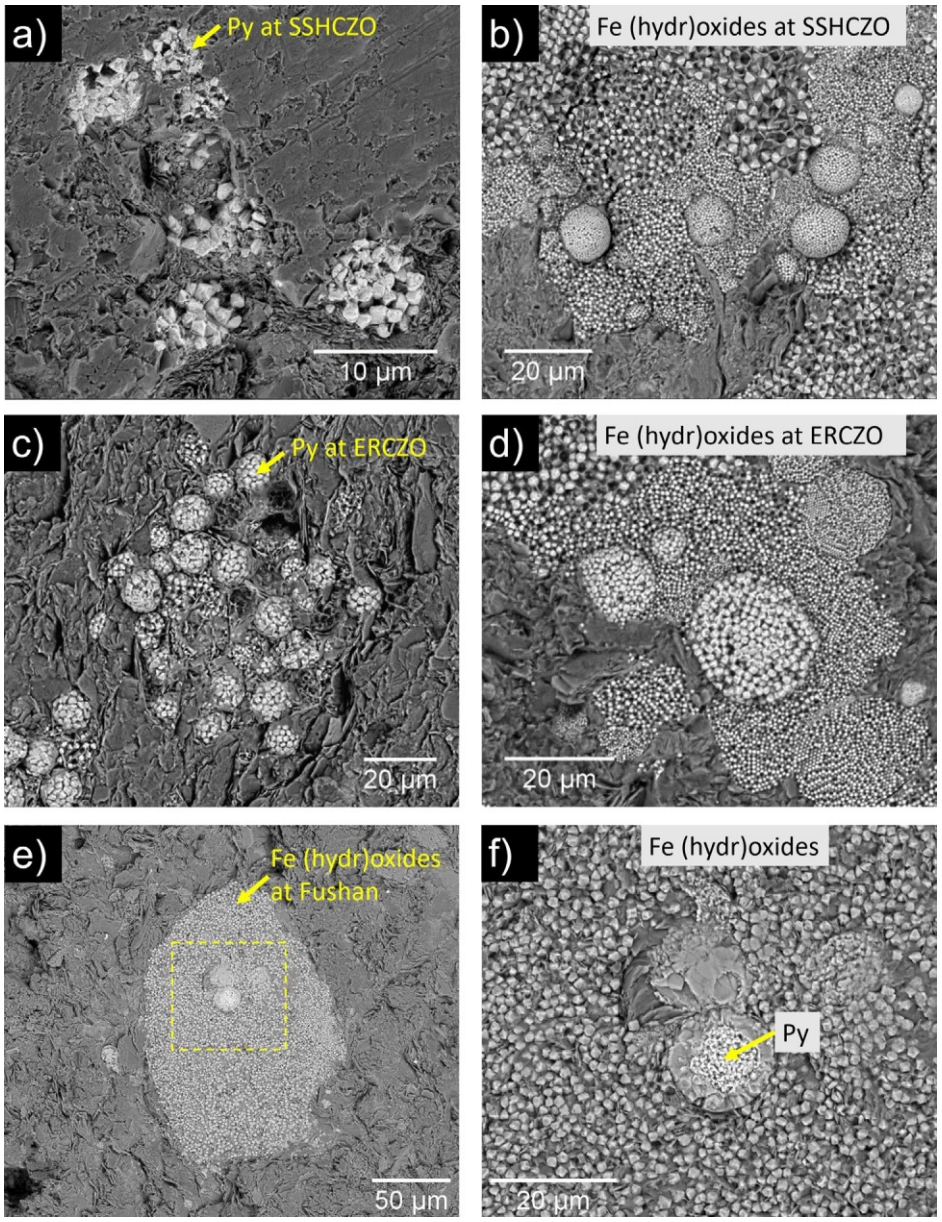

Fig. 3. BSE images showing pseudomorphic transformation of pyrite into Fe (hydr)oxide. Pyrite framboids in samples below the pyrite depletion front were observed in: a) SSHCZO (CZMW8-61–62, 18.8 mbls), and c) ERCZO (ERCZO_W10-55, 16.8 mbls). Framboid-like features observed in samples above the pyrite depletion front consist of Fe (hydr)oxide instead of Fe sulfide in b) SSHCZO (CZMW8-50.4, 15.4 mbls), and d) ERCZO (ERCZO_W10-45, 13.7 mbls). In the sample from the borehole at Fushan (Fushan_FSC1_2, 14.8 mbls), similar framboidal features are observed and consist mostly of Fe (hydr)oxides (e). Pyrite was observed (f) in the center as shown in the zoom-in view of the dashed box in e (notice pyrite is brighter than surrounding Fe (hydr)oxides). Pyrite and Fe (hydr)oxides were distinguished by EDS.

amount of carbonate as observed in the outcrops but was completely depleted in the rest of the borehole and in soil pits (Fig. 6).

In contrast to SSHCZO and ERCZO where sulfur is observed at higher concentrations below the oxidation depth, the concentrations of sulfur in all the shale samples from Fushan, even in most outcrop samples (except in one outcrop sample Fushan_FSR6, see Appendix C), are low (<0.01 wt.%). However, like the SSHCZO and ERCZO, Fe (hydr)oxide and occasional pyrite framboids were observed that are almost identical to those observed at the other two sites (Fig. 3). We thus inferred that pyrite framboids were originally present in protolith. This inferred presence of pyrite in the protolith at this site is consistent with prior work on the Kankou Formation (Lin et al., 2001). We therefore used the observed concentration of Fe (hydr)oxide framboids to calculate an inferred fraction of pyrite in the true parent prior to weathering (Appendix

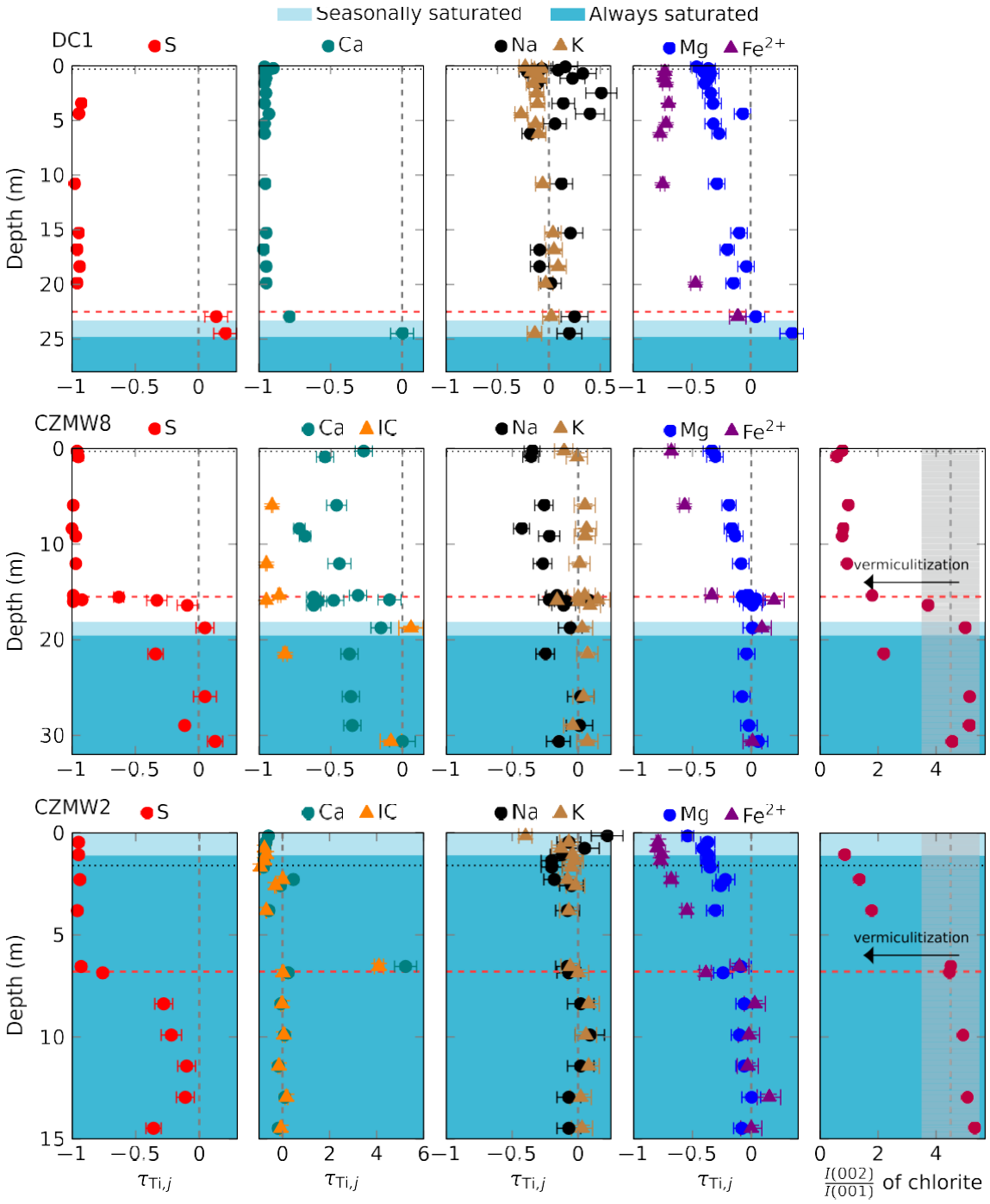

Fig. 4. Geochemical profiles at SSHCZO. The first four columns of panels are plots of s for S, inorganic carbon (IC), Ca, Na, K, Mg and ferrous iron (Fe^{2+}) in non-sulfide minerals, calculated assuming Ti as the immobile element in boreholes DC1, CZMW2 and CZMW8 (see Fig. 1b for the locations of these boreholes). The elemental measurements of samples from DC1, CZMW2 and CZWM8 were reported in Jin et al. (2010), Brantley et al. (2013) and Sullivan et al. (2016), respectively. The IC concentrations for CZMW8 are reported in Table S1. The IC concentrations for CZMW2 were calculated as the difference between total carbon concentration (reported in Brantley et al., 2013) and a constant organic carbon concentration (0.1 wt.%, Table S1). The Ca and IC concentrations of the parent were determined as an average over all concentrations in protolith in each borehole (see text). Other elements of the parent were averaged over the concentrations in protolith from all boreholes (see Appendix B). The horizontal dashed red line depicts the pyrite depletion front, which separates the protolith and regolith (see text). The horizontal dashed black line depicts the interface between mobile soil and weathered rock. The last column shows the degree of vermiculitization by normalizing the X-ray diffraction peak intensity of chlorite 002 reflection (~7.1 Å) to the peak intensity of chlorite 001 reflection (14.1–14.3 Å) on random powder mounts: the lower the ratio, the higher the degree of vermiculitization. The dashed vertical line represents the mean value for the parent (see data in Table 2), and the gray area shows two standard deviations. Not enough samples from the DC1 core were available to analyze IC nor the degree of vermiculitization.

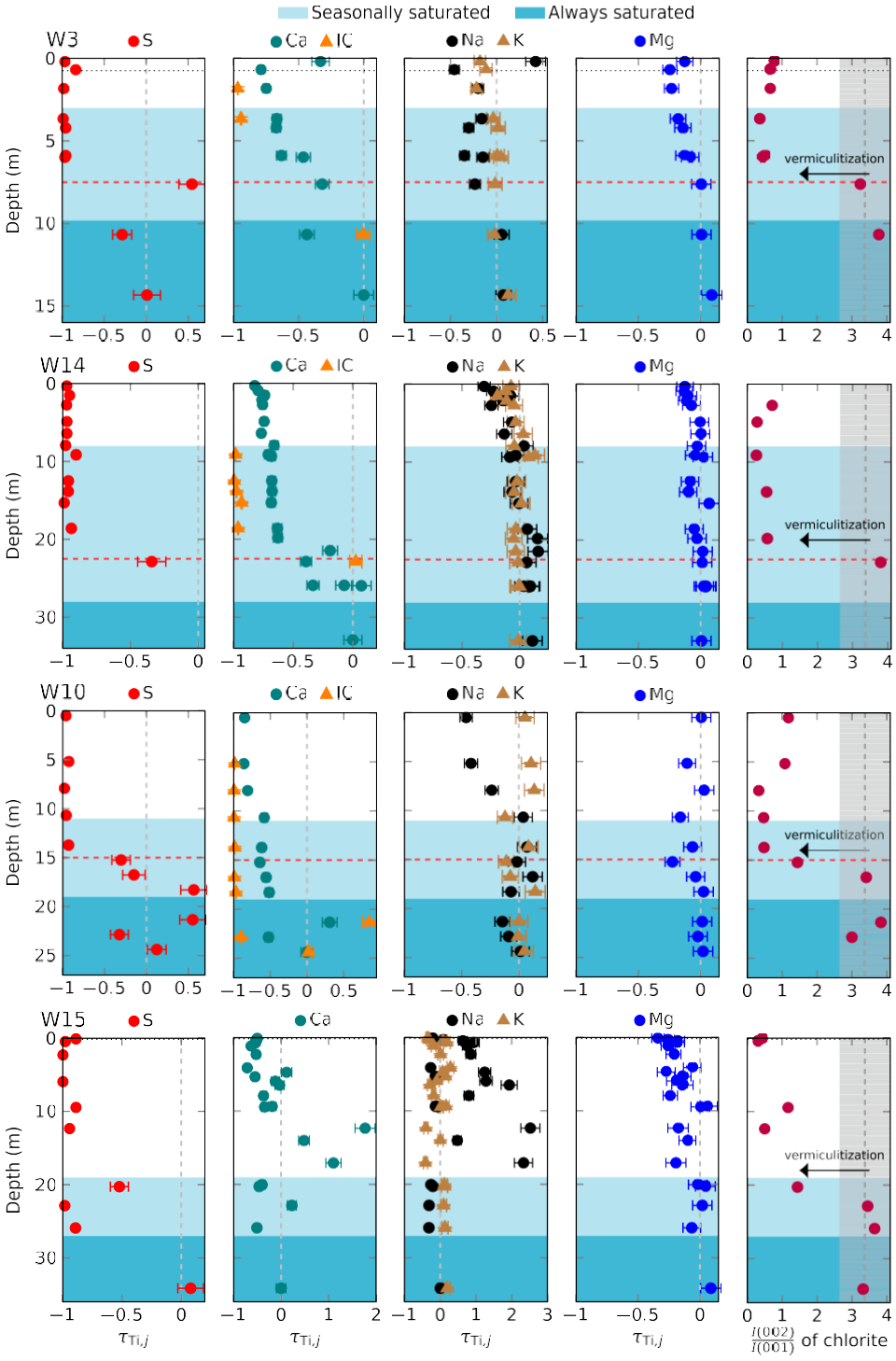

Fig. 5. Geochemical profiles at ERCZO. The first four columns of panels are plots of s for S, inorganic carbon (IC), Ca, Na, K, and Mg, calculated assuming Ti as the immobile element in boreholes W3, W14, W10, and W15 (see Fig. 1c for the locations of these boreholes). The elemental data are reported in Table 3. The parent concentrations were the average of the protolith from all the boreholes (see Appendix B). The dashed vertical line in the last column represents the mean value for the parent (see data in Table 2), and the gray area shows two standard deviations. The variation of concentrations of Na and Ca in borehole W15 indicates several zones in W15 are enriched in plagioclase but depleted in clay minerals and Ti. The description of the labels can be found in the caption of Fig. 4.

Table 3
Elemental concentrations (weight percent, ppm for Zr) of samples from ERCZO and Fushan.

Sample Type	Sample ID	Depth (mbls)	Al[a]	Ca[a]	Fe[a]	K[a]	Mg[a]	Mn[a]	Na[a]	P[a]	Si[a]	Ti[a]	Zr[a]	S[b]	TC[b]	IC[c]	LOI[d]
Bulk soil from borehole W3 at ERCZO	ERCZO_W3-soil	0.2	9.01	0.76	4.54	1.50	1.41	0.10	2.11	0.09	29.31	0.46	185	BDL[e]	0.43	NM [f]	6.72
	ERCZO_W3-2[g]	0.7	9.32	0.37	5.09	1.74	1.32	0.18	0.87	0.10	24.67	0.50	141	0.016	3.40	NM	14.39
Rock chip from borehole W3 at ERCZO	ERCZO_W3-6	1.8	9.45	0.48	5.46	1.68	1.46	0.12	1.39	0.11	26.95	0.55	149	BDL	0.27	0.005	NM
	ERCZO_W3-12	3.7	9.20	0.56	5.22	1.83	1.38	0.15	1.29	0.10	27.37	0.48	130	BDL	0.37	0.007	NM
	ERCZO_W3-13	4.2	9.66	0.56	5.44	1.98	1.48	0.13	1.10	0.09	26.60	0.50	138	BDL	0.40	NM	9.30
	ERCZO_W3-19	5.9	9.78	0.62	5.21	1.92	1.47	0.07	1.01	0.09	26.25	0.49	128	BDL	0.38	NM	9.80
	ERCZO_W3-25	7.6	9.84	1.22	5.68	1.99	1.80	0.12	1.25	0.11	26.08	0.51	136	0.156	0.63	NM	8.05
	ERCZO_W3-35	10.7	9.35	0.96	5.34	1.89	1.73	0.08	1.65	0.10	26.82	0.49	129	0.069	0.66	0.125	NM
	ERCZO_W3-47	14.3	9.22	1.52	5.21	1.94	1.66	0.10	1.50	0.12	26.85	0.44	150	0.087	0.90	NM	NM
Rock chip from a soil pit near borehole W10 at ERCZO	ERCZO_W10-2	0.5	10.20	0.19	5.99	2.15	1.82	0.08	0.89	0.08	25.97	0.52	188	0.004	0.36	NM	8.34
Rock chip from borehole W10 at ERCZO	ERCZO_W10-17	5.2	9.83	0.17	5.66	2.13	1.52	0.05	0.91	0.07	25.60	0.49	119	0.007	0.48	0.002	8.27
	ERCZO_W10-26	7.9	10.13	0.23	5.45	2.20	1.77	0.13	1.20	0.06	25.56	0.49	133	BDL	0.20	BDL	8.95
	ERCZO_W10-35	10.7	9.11	0.49	5.55	1.68	1.42	0.04	1.61	0.12	26.96	0.49	128	0.004	0.74	BDL	NM
	ERCZO_W10-45	13.7	9.27	0.40	5.78	1.85	1.42	0.04	1.48	0.09	26.91	0.43	110	0.006	0.72	0.002	NM
	ERCZO_W10-50	15.2	9.11	0.42	4.75	1.70	1.31	0.04	1.52	0.08	25.83	0.49	132	0.067	0.49	NM	NM
	ERCZO_W10-55	16.8	9.26	0.54	4.93	1.81	1.66	0.07	1.77	0.08	27.08	0.50	123	0.083	0.88	BDL	NM
	ERCZO_W10-60	18.3	10.00	0.59	5.44	2.25	1.79	0.09	1.48	0.10	26.55	0.50	149	0.154	0.63	0.004	NM
	ERCZO_W10-70	21.3	9.48	1.57	5.46	1.94	1.74	0.14	1.34	0.10	25.99	0.49	135	0.150	0.85	0.233	7.69
	ERCZO_W10-75	22.9	9.20	0.60	5.34	2.02	1.77	0.09	1.50	0.09	26.45	0.52	124	0.069	0.45	0.013	NM
	ERCZO_W10-80	24.4	9.92	1.15	5.41	1.96	1.69	0.11	1.54	0.09	26.38	0.48	131	0.105	0.69	0.124	NM
Rock chip from borehole W14 at ERCZO	ERCZO_W14-1[h]	0.3	9.99	0.36	5.75	1.88	1.57	0.15	1.14	0.10	26.52	0.52	141	BDL	1.81	NM	7.80
	ERCZO_W14-3[h]	0.9	9.72	0.41	5.58	1.77	1.54	0.11	1.25	0.10	27.23	0.51	147	NM	NM	NM	7.00
	ERCZO_W14-5[h]	1.5	9.31	0.51	3.73	1.58	1.56	0.09	1.46	0.11	27.66	0.50	140	0.005	1.52	NM	6.60
	ERCZO_W14-7[h]	2.1	9.79	0.47	5.29	1.78	1.58	0.09	1.39	0.09	27.29	0.51	136	NM	NM	NM	6.90
	ERCZO_W14-9[h]	2.7	10.00	0.50	5.83	1.98	1.71	0.08	1.27	0.10	26.12	0.53	134	BDL	0.59	NM	7.80
	ERCZO_W14-16	4.9	9.72	0.49	5.56	1.84	1.68	0.09	1.44	0.09	26.72	0.49	128	BDL	0.58	NM	7.60
	ERCZO_W14-21[h]	6.4	10.00	0.45	5.75	2.02	1.73	0.09	1.37	0.07	26.39	0.50	123	BDL	0.98	NM	7.30
	ERCZO_W14-26[h]	7.9	9.48	0.63	5.66	1.78	1.60	0.10	1.57	0.12	27.13	0.47	131	BDL	0.51	NM	6.80
	ERCZO_W14-30	9.1	9.40	0.53	4.87	2.06	1.54	0.08	1.43	0.07	26.05	0.46	119	0.009	0.40	0.002	7.87
	ERCZO_W14-31[h]	9.4	9.78	0.59	5.40	2.01	1.68	0.09	1.38	0.07	26.90	0.47	125	NM	NM	NM	7.10
	ERCZO_W14-41[h]	12.5	9.31	0.60	5.29	1.84	1.53	0.09	1.48	0.09	27.42	0.48	129	0.004	0.54	BDL	7.30
	ERCZO_W14-45[h]	13.8	9.48	0.63	5.39	1.86	1.56	0.07	1.48	0.10	27.17	0.50	137	0.004	0.54	0.003	7.20
	ERCZO_W14-50[h]	15.3	9.67	0.61	5.46	1.96	1.83	0.09	1.56	0.10	27.01	0.49	129	BDL	0.16	0.008	6.50
	ERCZO_W14-61	18.6	9.26	0.68	5.25	1.80	1.57	0.07	1.61	0.09	27.79	0.47	132	0.006	0.56	0.005	6.40
	ERCZO_W14-65[h]	19.8	9.42	0.69	4.99	1.77	1.60	0.07	1.74	0.09	27.71	0.47	136	NM	NM	NM	6.40
	ERCZO_W14-70[h]	21.5	9.36	1.48	4.97	1.78	1.66	0.08	1.73	0.09	27.17	0.47	132	NM	NM	NM	6.50
	ERCZO_W14-75	22.9	9.12	1.16	5.22	1.89	1.72	0.08	1.65	0.10	26.79	0.49	128	0.063	0.89	0.128	NM
	ERCZO_W14-85[h]	25.9	9.52	1.28	5.31	1.92	1.79	0.09	1.62	0.10	26.94	0.49	135	NM	NM	NM	6.20
	ERCZO_W14-85.2[h]	26.0	9.13	1.96	5.08	1.84	1.70	0.10	1.62	0.09	26.77	0.47	129	NM	NM	NM	6.90
	ERCZO_W14-108[h]	32.9	9.15	1.85	4.95	1.84	1.66	0.10	1.68	0.09	26.80	0.47	143	NM	NM	NM	6.90

Bulk soil from borehole W15 at ERCZO	ERCZO_W15-soil	0.1	8.47	0.55	4.41	1.16	1.05	0.10	1.15	0.06	26.58	0.45	168	0.010	3.39	NM	14.17
Rock chip from borehole W15 at ERCZO	ERCZO_W15-1[h]	0.3	8.08	0.41	4.85	1.33	1.27	0.09	1.71	0.05	29.75	0.49	234	NM	NM	NM	6.10
	ERCZO_W15-1.5[h]	0.5	8.19	0.33	4.08	1.75	1.18	0.05	2.15	0.04	30.52	0.41	179	BDL	0.89	NM	4.90
	ERCZO_W15-2.25[h]	0.7	8.42	0.29	3.60	1.69	1.02	0.05	2.23	0.03	30.78	0.36	146	NM	NM	NM	5.00
	ERCZO_W15-3.75[h]	1.1	7.92	0.25	3.75	1.27	1.03	0.05	2.21	0.04	31.51	0.40	192	NM	NM	NM	4.70
	ERCZO_W15-7.5[h]	2.3	7.67	0.31	3.63	1.50	1.04	0.05	2.23	0.04	31.76	0.38	193	BDL	0.74	NM	4.40
	ERCZO_W15-13.5[h]	4.1	9.96	0.24	5.53	2.42	1.57	0.07	1.12	0.07	26.42	0.48	130	NM	NM	NM	8.10
	ERCZO_W15-15.5[h]	4.7	8.29	0.72	3.18	1.58	0.96	0.06	2.70	0.04	30.95	0.38	155	NM	NM	NM	4.30
	ERCZO_W15-17.5[h]	5.3	9.55	0.36	4.85	2.08	1.39	0.05	1.26	0.07	27.75	0.46	129	NM	NM	NM	7.50
	ERCZO_W15-19.5[h]	5.9	7.70	0.48	3.73	1.13	0.90	0.04	2.31	0.06	31.64	0.32	141	BDL	0.19	NM	4.90
	ERCZO_W15-21[h]	6.5	6.94	0.46	3.00	0.77	0.83	0.05	2.57	0.04	33.46	0.28	128	NM	NM	NM	3.70
	ERCZO_W15-26[h]	7.9	8.03	0.41	3.77	1.24	1.02	0.05	2.20	0.05	31.05	0.38	176	NM	NM	NM	5.30
	ERCZO_W15-30.75[h]	9.4	9.89	0.69	5.78	2.27	1.84	0.09	1.37	0.09	26.00	0.50	137	NM	NM	NM	7.50
	ERCZO_W15-31	9.4	9.14	0.56	5.85	1.99	1.75	0.07	1.47	0.12	26.21	0.50	126	0.011	0.76	NM	NM
	ERCZO_W15-40.5[h]	12.3	7.02	1.37	2.44	0.68	0.83	0.05	3.23	0.05	33.15	0.29	185	BDL	0.19	NM	3.10
	ERCZO_W15-46[h]	14.0	8.65	1.17	4.77	1.83	1.45	0.06	2.17	0.07	28.27	0.46	134	NM	NM	NM	5.80
	ERCZO_W15-56[h]	17.1	6.86	1.06	2.61	0.68	0.83	0.05	3.12	0.05	33.49	0.29	164	NM	NM	NM	2.80
	ERCZO_W15-65.75[h]	20.0	9.72	0.53	5.49	2.26	1.77	0.07	1.22	0.10	26.68	0.52	133	NM	NM	NM	7.30
	ERCZO_W15-66	20.3	9.36	0.45	5.22	2.17	1.79	0.07	1.24	0.10	27.03	0.49	129	0.046	0.64	NM	NM
	ERCZO_W15-75[h]	22.9	9.82	1.06	5.69	2.17	1.79	0.06	1.11	0.10	25.96	0.50	129	BDL	0.70	NM	7.90
	ERCZO_W15-85	25.9	9.87	0.44	5.42	2.30	1.69	0.04	1.13	0.08	26.49	0.52	122	0.011	0.68	NM	NM
	ERCZO_W15-112[h]	34.1	10.09	0.82	5.51	2.25	1.82	0.10	1.54	0.10	26.17	0.48	125	0.102	0.72	NM	6.80
Rock chip from borehole Elder Creek at ERCZO	ERCZO_Elder Crk 19–22 in	0.5	9.26	1.17	5.06	1.80	1.65	0.08	1.61	0.10	27.53	0.49	135	0.079	0.69	NM	NM
	ERCZO_Elder Crk 4–5 ft	1.4	9.16	1.41	5.22	1.81	1.69	0.09	1.50	0.10	26.88	0.50	130	0.079	0.74	NM	NM
	ERCZO_Elder Crk 6–7 ft	2.0	9.05	1.41	5.19	1.78	1.69	0.09	1.51	0.10	26.78	0.49	143	0.078	0.78	NM	NM
Parent of ERCZO[g]			9.4 (0.3)	1.2 (0.4)	5.2 (0.2)	1.9 (0.1)	1.7 (0.1)	0.10 (0.02)	1.55 (0.1)	0.10 (0.01)	26.6 (0.4)	0.49 (0.01)	134 (8)	0.10 (0.03)	0.7 (0.1)	0.13 (0.07)	–
Rock chip from soil core FS1 at Fushan	Fushan_FS1O	0.05	9.31	0.01	5.06	2.65	1.33	0.05	0.13	0.03	28.28	0.49	NM	0.005	0.16	NM	NM
	Fushan_FS1A	0.25	9.05	0.01	4.50	2.57	1.16	0.02	0.13	0.03	29.12	0.50	NM	0.004	0.12	0.008	NM
	Fushan_FS1B1	0.4	9.42	0.01	5.04	2.78	1.00	0.02	0.12	0.06	28.09	0.53	NM	0.007	0.12	NM	NM
	Fushan_FS1B2	0.6	10.00	0.01	5.58	2.68	1.12	0.02	0.13	0.05	26.97	0.49	NM	0.009	0.26	NM	NM
	Fushan_FS1C	1	9.84	0.01	4.60	2.91	1.19	0.02	0.14	0.04	27.49	0.53	NM	0.004	0.16	NM	NM
	Fushan_FS1R	1.4	9.58	0.01	4.67	2.93	1.32	0.07	0.19	0.04	28.75	0.53	NM	BDL	0.16	0.007	NM

(*continued on next page*)

Table 3 (*continued*)

Sample Type	Sample ID	Depth (mbls)	Al[a]	Ca[a]	Fe[a]	K[a]	Mg[a]	Mn[a]	Na[a]	P[a]	Si[a]	Ti[a]	Zr[a]	S[b]	TC[b]	IC[c]	LOI[d]
Rock chip from borehole FSC1 at Fushan	Fushan_FSC1_16	1.5	9.85	0.05	4.20	2.95	1.22	0.04	0.40	0.04	29.44	0.49	190	BDL	BDL	NM	NM
	Fushan_FSC1_14	3.4	11.02	0.06	6.66	2.94	2.06	0.05	0.59	0.08	25.84	0.48	169	BDL	0.19	NM	NM
	Fushan_FSC1_13	4.4	2.43	0.00	0.76	1.82	0.00	0.01	0.05	0.02	42.42	0.06	47	0.033	BDL	NM	NM
	Fushan_FSC1_12	5.5	9.30	0.14	4.15	2.65	1.20	0.02	0.86	0.05	29.75	0.50	180	BDL	0.14	NM	NM
	Fushan_FSC1_10	7.35	9.26	0.13	4.63	2.49	1.10	0.02	0.54	0.06	29.92	0.48	178	BDL	0.08	NM	NM
	Fushan_FSC1_8	9.4	10.95	0.11	5.30	3.25	1.28	0.04	0.29	0.06	27.07	0.53	192	BDL	0.09	NM	NM
	Fushan_FSC1_6	11.5	8.74	2.43	15.4	0.10	3.90	0.05	0.14	1.12	19.26	0.09	145	BDL	0.27	NM	NM
	Fushan_FSC1_4	13.4	10.21	0.17	5.35	2.92	1.59	0.02	0.63	0.06	27.30	0.47	NM	BDL	0.36	NM	NM
	Fushan_FSC1_2	14.8	9.26	0.19	4.72	2.61	1.59	0.03	0.88	0.06	29.26	0.50	NM	BDL	0.42	0.006	NM
Rock chip from borehole FSC2 at Fushan	Fushan_FSC2_1	15	2.18	0.01	0.38	1.57	0.06	0.01	0.10	0.01	41.88	0.05	NM	0.140	0.08	NM	NM
Outcrop at Fushan	Fushan_FSR1		8.79	0.57	4.22	2.42	1.25	0.07	1.13	0.05	29.78	0.47	NM	0.006	0.43	0.108	NM
	Fushan_FSR2		11.57	0.00	4.91	3.56	1.41	0.02	0.41	0.04	26.81	0.51	341	BDL	0.28	NM	NM
	Fushan_FSR3		10.74	0.00	4.57	3.23	1.39	0.03	0.63	0.05	28.06	0.50	223	BDL	0.34	NM	NM
	Fushan_FSR4		10.39	0.13	4.88	3.02	1.39	0.04	0.92	0.06	28.72	0.50	198	0.004	0.29	NM	NM
	Fushan_FSR6		9.81	0.02	5.64	2.97	1.13	0.05	0.89	0.07	27.98	0.49	198	0.626	0.36	NM	NM
	Fushan_FSR7		11.48	0.01	4.78	3.59	1.47	0.03	0.67	0.06	26.76	0.56	195	0.009	0.35	NM	NM
	Fushan_FSR8		9.27	0.34	4.31	2.63	1.27	0.07	1.17	0.05	29.88	0.50	202	0.005	0.29	NM	NM
	Fushan_FSR10		10.28	0.04	4.52	3.04	1.42	0.01	0.86	0.05	28.94	0.48	202	0.006	0.43	NM	NM
	Fushan_FSR12		10.72	0.00	4.86	3.20	1.46	0.05	0.43	0.03	27.72	0.50	182	BDL	0.25	NM	NM
Parent of Fushan[h]			10.3 (0.9)	0.5	4.7 (0.4)	3.1 (0.4)	1.4 (0.1)	0.04 (0.02)	0.8 (0.3)	0.05 (0.01)	28.3 (1.1)	0.50 (0.02)	212 (48)	0.15 (0.05)	0.33 (0.06)	0.11 (0.06)	NM

[i]The parent at ERCZO were the average of the protolith from boreholes W3, W10, W14, W15, and Elder Creek borehole. The quoted uncertainty is one standard deviation from the mean.
[j]The parent at Fushan was averaged over the outcrop samples. The parent concentration of Ca and IC was estimated from outcrop sample FSR1 (see Appendix B). The parent concentration of S was estimated from the area fractions of the Fe (hydr)oxide framboids in thin sections of the bottom-most shale (see Appendix C). The quoted uncertainty is one standard deviation from the mean.

[a] Measured by ICP-AES and reported on an ''as received" basis.
[b] Sulfur (S) and total carbon (TC) measured by a Carbon/Sulfur Determinator with detection limit 0.08% and 0.004% for TC and S, respectively.
[c] Inorganic carbon (IC) measured by a LI-COR CO_2-H_2O Analyzer with detection limit 0.001%. The concentration of organic carbon (OC) are the difference between TC and IC.
[d] Loss on ignition (LOI) measured by combustion (900 °C).
[e] Below detection limit (BDL).
[f] Not measured (NM).
[g] The notation gives the well site (e.g. 3) followed by the depth (e.g. 2) so W3-2 is 2 feet below surface at well 3.
[h] Major element chemistry data provided by B. Houlton, University of California, Davis.

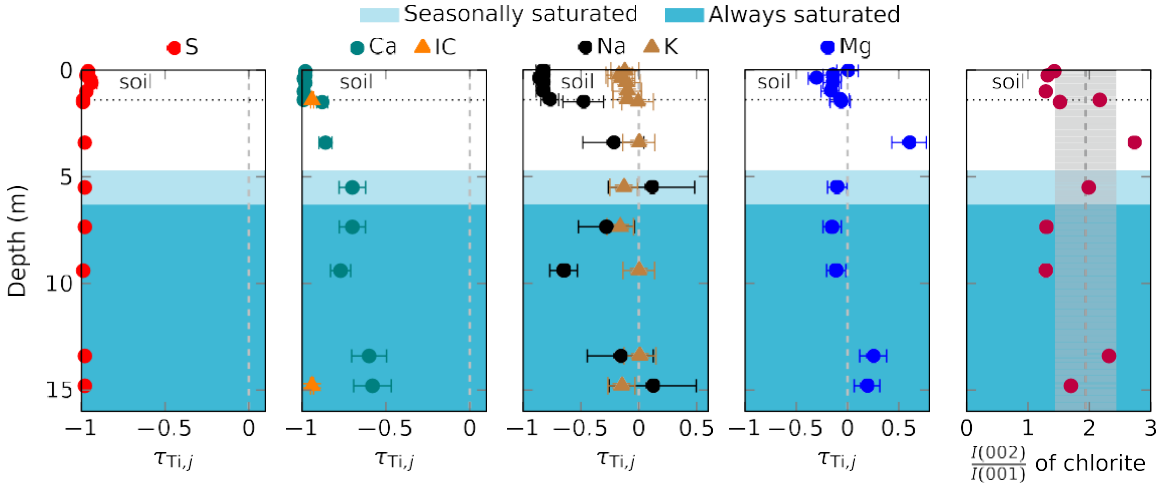

Fig. 6. Geochemical profiles of rock chips from Fushan. The first four columns of panels are plots of s for S, inorganic carbon (IC), Ca, Na, K, and Mg, calculated assuming Ti as the immobile element. The samples below soil-saprock interface were collected from borehole FSC1 near the valley and other samples were rock chips collected from a soil pit (FS1) nearby (see Fig. 1d for the locations). Sample FSC1_6 from 11.5 mbls and sample FSC1_13 from 4.4 mbls are from sandy interbeds and therefore are excluded in the plots. The elemental data are reported in Table 3. The parent concentrations were set equal to the average of the outcrop samples (see Appendix B). The dashed vertical line in the last column represents the mean value for the samples from the outcrop (see data in Table 2), and the gray area shows two standard deviations. The description on the labels can be found in the caption of Fig. 4.

C). Based on this estimation of sulfur concentration of parent, all the shale samples from Fushan were almost completely depleted (>95% loss) in pyrite (Fig. 6).

The depletion of plagioclase initiates at ~5 mbls under the valley. Depletion almost went to 100% in the bulk soil and in rock chips recovered from soil collected in the valley.

In all rock chips recovered from core from the valley, chlorite shows limited or no depletion (Fig. 6). On the other hand, samples of bulk soil in the valley in Fushan were more depleted in Mg compared to the rock chips collected from the same depth (Fig. S3), demonstrating that chlorite weathering is occurring in the granular soil at Fushan.

Illite shows very little depletion in either bulk soil or rock chips recovered from the soils under the valley at Fushan. However, the extent of depletion of illite in bulk soil collected from the ridge was observed to be greater than the extent of depletion under the valley (Fig. S3).

The concentrations of OC in the rock chips recovered from depth shallower than ~10 mbls are significantly lower than the samples from deeper depth and from outcrops (Table 3).

4.4. Porosity changes during shale weathering

Matrix porosity. As discussed above, the scattering intensity for dry samples (blue dots in Fig. 7) is a measure of the total porosity. The total porosities in protolith from SSHCZO and ERCZO and the bottom-most shale from the Fushan valley borehole are all less than the total porosities measured in weathered samples at each site (Fig. 7; no porosity measurement was conducted on the Fushan outcrop sample). Thus, porosity increases with weathering in all the shales.

The differences in scattering intensities between sets of samples before and after contrast matching, and raw (unimpregnated) samples (red circles in Fig. 7) reflect the fraction of the porosity that was not invaded by fluid during H_2O-D_2O saturation, i.e. ϕ_{inacc}. After weathering, the scattering from water-inaccessible porosities (red dots in Fig. 7) remained almost the same in all samples, while the scattering from total porosities (blue dots in Fig. 7) significantly increased. Thus, the increase in porosity during weathering was related to development of water-accessible porosity (Table 4).

The difference in scattering intensity between contrast matched ($I_{wet,\ raw}$) and contrast matched, epoxy impregnated ($I_{wet,epoxy\text{-}im}$) samples reflects the fraction of the porosity that was invaded by epoxy: these pores are relatively large since they are both water and epoxy accessible (ϕ_{epoxy}). The scattering from epoxy-porosities (the difference between brown and red dots in Fig. 7) was significantly higher in the weathered samples from ERCZO and Fushan than those from SSHCZO (Table 4).

Pore size distribution analysis. More information about fine structure can be obtained through analysis of pore size distributions (PSD) (Fig. 7, right panel). The PSDs of the unweathered shale samples are similar: a major, sharp peak around 2 to 3 nm and a minor and broader peak around 10^3 to 10^4 nm. The pores smaller than ~10 nm are likely associated with phyllosilicates, as observed in other organic-poor shales (Kuila and Prasad, 2013; Gu et al., 2016). These pores are found between crystals (intercrystalline pores) or within crystals or aggregates (intracrystalline and interlayer pores). The pores larger than 10 nm are attributed to interparticle pores, e.g., pores along rigid grains as shown in Fig. 2.

The shape of PSDs from SSHCZO did not change dramatically during weathering, although the water-accessible porosity increased from 3.0% (unweathered) to 6.0% (weathered). This increase occurred over the same depth

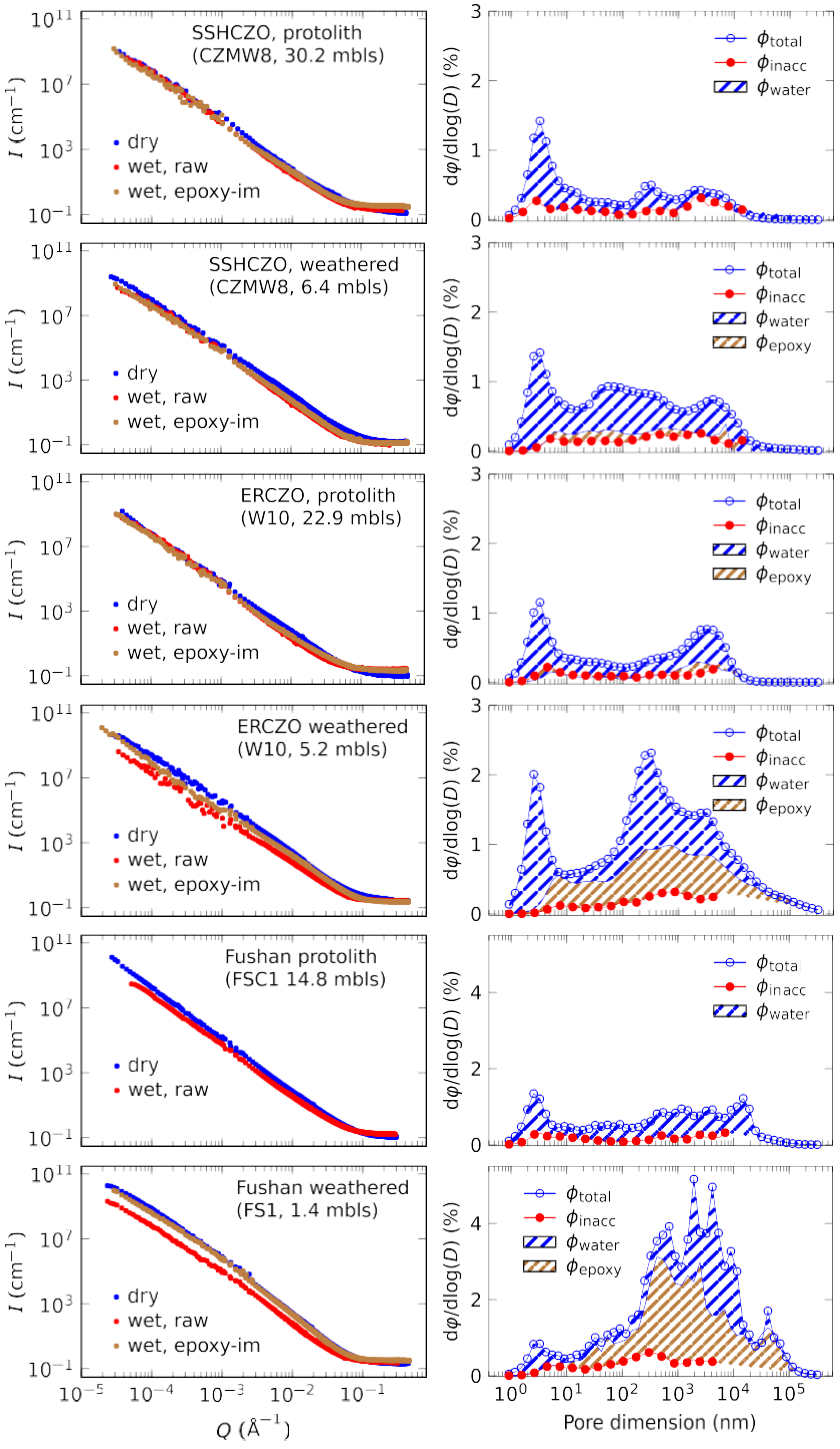

Fig. 7. Neutron scattering curves (left panel) and pore size distributions (PSD, right panel) derived from combined neutron scattering data (on the left) and imaging data for protolith and weathered samples from SSHCZO, ERCZO and Fushan (rows from top to bottom). As discussed in the text, the ‘‘unweathered” sample for Fushan, the bottom-most shale sample from a borehole, has already been chemically weathered (depleted in carbonate and pyrite). The neutron scattering intensity (I) was plotted as a function of momentum transfer (Q). These scattering intensity curves reflect sample porosity and are thus labelled as ‘‘dry” for the samples before contrast matching, as ‘‘wet, epoxy-in” for contrast matched, epoxy-impregnated samples, and as ‘‘wet, raw” for contrast matched, raw samples. The negative of the slopes of these log-log plots reflect the fractal features of pore-solid interface of shale (Mildner and Hall, 1986; Allen, 1991). Each plotted symbol in the PSD indicates the % of the total sample volume that falls in a specific size range of pores as calculated using the polydisperse sphere porosity model. Integration under the curve yields the total porosity of the sample. Notice that the total porosity of protolith is always lower than that of weathered shale from the same site. Pores are classified by the fluid accessibility: (i) epoxy-accessible pores ($/_{epoxy}$), (ii) epoxy-inaccessible but water-accessible pores ($/_{water}$), and (iii) fluid-inaccessible pores ($/_{inacc}$). See Appendix A for a full description.

Table 4
Summary of pore structure characteristics derived from neutron scattering for samples from SSHCZO, ERCZO and Fushan.

Sample Type	Sample ID	Depth (mbls)	Characteristics of total porosity			Classes of porosity[d]				Characteristics of nano-porosity (<10 nm)[f]			
			ϕ_{total} (%)[a]	SSA_{total} ($m^2 g^{-1}$)[b]	d (nm)[c]	ϕ_{inacc} (%)	ϕ_{epoxy} (%)	ϕ_{water} (%)	ϕ_f (%)[e]	ϕ_{total} (%)	SSA_{total} ($m^2 g^{-1}$)	ϕ_{inacc} (%)	SSA_{inacc} ($m^2 g^{-1}$)
Rock chip from a soil pit under ridge at SSHCZO	SSHCZO_RT-50	0.5	11.4 (2.3)	23.3 (5.8)	7.5	1.6 (0.3)	1.1 (0.4)	8.7	0.5	2.7	20.7	0.3	1.4
	SSHCZO_RT-130	1.3	10.4 (1.9)	25.5 (5.5)	6.3	1.8 (0.3)	NM[g]	NM	0.4	2.9	23.2	0.3	1.4
Rock chip from borehole CZMW8 at SSHCZO	SSHCZO_CZMW8-21	6.4	8.1 (1.1)	18.3 (4.2)	6.8	2.1 (0.5)	0.4 (0.1)	5.6	<0.1	2.2	16.5	0.4	1.7
	SSHCZO_CZMW8-49	14.9	7.1 (1.5)	12.4 (4.0)	8.9	1.8 (0.4)	NM	NM	<0.1	1.6	11.4	0.2	1.0
	SSHCZO_CZMW8-53	16.2	5.0 (1.1)	12.8 (3.8)	6.0	1.0 (0.2)	NM	NM	<0.1	1.8	11.8	0.2	1.0
	SSHCZO_CZMW8-65	19.8	5.0 (0.9)	12.6 (3.7)	6.1	1.6 (0.3)	<0.2	1.8	<0.1	1.8	11.8	0.5	3.6
	SSHCZO_CZMW8-99	30.2	4.5 (1.0)	13.2 (4.0)	5.3	1.5 (0.5)	<0.2	1.9	<0.1	1.9	12.5	0.4	3.0
Rock chip from borehole W3 at ERCZO	ERCZO_W3-6	1.8	12.5 (1.1)	14.7 (3.9)	13.1	1.7 (0.5)	7.5 (2.3)	3.3	4.6	1.9	13.8	0.4	1.7
	ERCZO_W3-12	3.7	10.2 (1.2)	12.2 (3.2)	12.9	2.1 (0.5)	4.9 (1.5)	3.2	3.6	1.2	10.5	0.3	1.1
	ERCZO_W3-35	10.7	5.8 (0.8)	10.8 (3.2)	8.2	2.9 (0.5)	<0.2	0.9	<0.1	1.6	10.0	0.3	1.4
Rock chip from borehole W10 at ERCZO	ERCZO_W10-17	5.2	11.8 (1.5)	23.4 (7.0)	7.7	1.6 (0.6)	5.1 (1.5)	5.1	3.3	2.3	22.1	0.5	2.4
	ERCZO_W10-35	10.7	12.1 (1.2)	27.4 (7.4)	6.8	2.1 (0.5)	NM	NM	NM	2.4	26.3	0.4	2.3
	ERCZO_W10-45	13.7	11.3 (1.3)	31.5 (7.2)	5.5	1.9 (0.6)	5.8 (1.7)	3.6	3.1	3.0	30.1	0.6	3.5
	ERCZO_W10-50	15.2	9.5 (1.4)	32.1 (8.6)	4.6	2.1 (0.5)	3.7 (1.1)	3.7	2.8	3.0	30.9	0.7	4.4
	ERCZO_W10-55	16.8	6.1 (0.8)	14.6 (4.0)	6.4	1.5 (0.3)	NM	NM	2.2	1.5	13.9	0.2	1.1
	ERCZO_W10-75	22.9	4.7 (0.8)	10.6 (2.8)	6.8	1.2 (0.3)	<0.2	2.0	0.1	1.2	10.1	0.2	0.8
Rock chip from borehole W14 at ERCZO	ERCZO_W14-16	4.9	10.7 (1.4)	23.5 (7.2)	7.0	2.0 (0.6)	3.2 (1.0)	5.5	2.6	2.3	22.7	0.6	2.9
	ERCZO_W14-30	9.1	8.3 (1.1)	20.4 (5.5)	5.5	2.2 (0.6)	4.6 (1.4)	1.5	2.7	2.2	21.7	0.7	3.3
	ERCZO_W14-75	22.9	4.0 (0.8)	15.3 (4.2)	4.0	1.4 (0.3)	<0.2	2.4	0.1	1.7	16.3	0.4	1.7
Rock chip from borehole W15 at ERCZO	ERCZO_W15-16	4.9	7.6 (0.7)	21.2 (7.4)	5.5	1.6 (0.4)	NM	NM	NM	1.9	20.5	0.1	0.5
	ERCZO_W15-31	9.4	5.5 (1.0)	16.0 (4.2)	5.2	2.3 (0.4)	NM	NM	1.2	1.9	15.3	0.6	3.2
	ERCZO_W15-85	25.9	3.0 (0.7)	8.8 (3.9)	5.3	2.0 (0.3)	<0.2	0.9	<0.1	1.0	9.3	0.3	1.6
Rock chip from soil core FS1 at Fushan	Fushan_S1O	0.05	19.8 (3.1)	7.3 (1.1)	41.9	NM	NM	NM	3.8	0.4	5.3	NM	NM
	Fushan_S1A	0.25	21.6 (2.5)	8.6 (1.8)	38.6	3.0 (0.6)	8.8 (2.3)	10.0	6.5	1.3	6.4	0.4	1.5
	Fushan_S1B1	0.4	15.1 (1.8)	6.8 (1.6)	33.9	NM	NM	NM	NM	1.0	5.2	NM	NM
	Fushan_S1B2	0.6	21.6 (3.2)	10.2 (2.6)	32.4	NM	NM	NM	NM	1.4	8.4	NM	NM
	Fushan_S1C	1.0	18.4 (2.8)	7.2 (1.8)	39.1	NM	NM	NM	4.1	0.8	6.1	NM	NM
	Fushan_S1R	1.5	18.5 (2.4)	7.2 (1.8)	39.8	2.4 (0.6)	5.8 (1.6)	10.3	3.2	1.5	6.0	0.1	0.5

(*continued on next page*)

Table 4 (*continued*)

Sample Type	Sample ID	Depth (mbls)	Characteristics of total porosity			Classes of porosity[d]				Characteristics of nano-porosity (<10 nm)[f]		
			I_{total} (%)[a]	SSA_{total} ($m^2\ g^{-1}$)[b]	d (nm)[c]	I_{inacc} (%)	I_{epoxy} (%)	I_{water} (%)	I_f (%)[e]	I_{total} (%)	SSA_{total} ($m^2\ g^{-1}$)	I_{inacc} (%)	SSA_{inacc} ($m^2\ g^{-1}$)
Rock chip from borehole FSC1 at Fushan	Fushan_FSC1_4	13.4	12.7 (1.6)	17.1 (3.5)	11.4	1.7 (0.4)	4.5 (1.2)	6.5	1.8	2.1	15.4	0.5	2.9
	Fushan_FSC1_2	14.8	5.9 (0.9)	4.9 (1.8)	18.5	1.7 0.3)	NM	NM	<0.1	0.8	4.2	0.1	0.4
Rock chip from borehole FSC2 at Fushan	Fushan_FSC2_1	15.0	1.7 (0.3)	0.8 (0.3)	31.1	1.3 (0.3)	NM	NM	<0.1	0.1	0.6	0.1	0.6

[a] The total porosity (I_{total}) and specific surface area (SSA_{total}) were derived from a combination of neutron scattering and imaging data using the polydisperse sphere (PDSP) model as described in the text. The quoted uncertainty is one standard deviation from the mean.

[b] The default unit of SSA exported from scattering data is $length^{-1}$. Here, the SSA was calculated by assuming the bulk density is 2.6 g cm^{-3}.

[c] The average pore dimension (d) is calculated as $4/_{total}$=SSA_{total}.

[d] Different classes of porosities were calculated using Eqs. (A1)–(A3).

[e] Fracture porosity estimated from SEM images.

[f] Proportion of porosity and SSA of pores smaller than 10 nm by diameter derived from neutron scattering data. The water-inaccessible porosity and SSA were determined on the contrast matched samples (see text for details).

[g] NM designates parameters that were not measured.

interval where chlorite dissolved (Fig. 8). In the weathered shale from ERCZO and Fushan, however, broad peaks centered around 10^3 to 10^4 of nm in pore dimensions become dominant in weathered samples (Fig. 7). This broad peak primarily consists of epoxy-accessible pores. As shown in Fig. 9 and discussed in the next section, this peak is mainly attributed to microfractures.

The changes in the different types of porosity in rock chips with depth for the three sites are illustrated in Fig. 9. In all three sites, the water-inaccessible porosities (I_{inacc}) remain relatively constant and similar to the protolith, but the water-accessible porosities (I_{water}) gradually increase upward; in addition, the epoxy-accessible porosities (I_{epoxy}) at ERCZO and Fushan are much higher than at SSHCZO.

Mercury Intrusion Porosity (MIP). At SSHCZO, the porosity measured by MIP gradually increased from 1.6 ± 0.5% in protolith to 5.5 ± 1.0% in weathered rock (Table 5). However, the breakthrough critical pressures, as well as the inferred pore throat sizes (critical pore throat sizes), did not change significantly from protolith to weathered rock at SSHCZO (Fig. 10a, Table 5), despite the threefold increase in porosity. Based on the empirical estimation previously given as Eq. (3), the increase of permeability in weathered rock at SSHCZO can mainly be explained by the increase of porosity. The permeability values of protolith (0.1–0.3 nD) at SSHCZO estimated through MIP data according to Eq. (3) are also consistent with the permeability value measured in a hydraulic conductivity test on intact rock from SSHCZO (~0.25 nD, Kuntz et al., 2011).

At ERCZO, the porosity measured by MIP for relatively unweathered sample ERCZO_W15-85 was twice to three times smaller than those of other samples that were recovered from shallower depth (Fig. 10b, Table 5). Similarly, the critical pore throat sizes of the weathered sample are 1.1–1.7 times higher than that of the relatively unweathered sample (Fig. 10b, Table 5).

At Fushan, both the porosity and the critical pore throat size measured by MIP increased upward toward the surface during weathering: the porosity and the critical pore throat size of the rock chip recovered from soil was 6 and 9 times higher than that of the bottom-most shale from Fushan, respectively. Such values are consistent with an increase in permeability (estimated through Eq. (3)) of more than three orders of magnitude (Fig. 10c, Table 5).

The total porosity — derived from neutron scattering and BSE imaging as described in Methods — is consistently higher than the porosity measured by MIP on the same sample. This is observed when the porosity measured by neutron scattering and BSE imaging is not the same porosity measured by MIP. For example, the minimum pore throat size measured by MIP is ~3 nm, while the minimum pore size measured by the combination of neutron scattering and imaging is ~1 nm. Therefore, small pores in shale such as interlayer space in clay minerals can be detected by neutron scattering but not by MIP. Assuming a body- to-throat pore-size aspect ratio of 3.5 as estimated for sandstone (Radlinski et al., 2004), the pore size measurable by MIP is ~10 nm. Consistent with this, the fluid-accessible

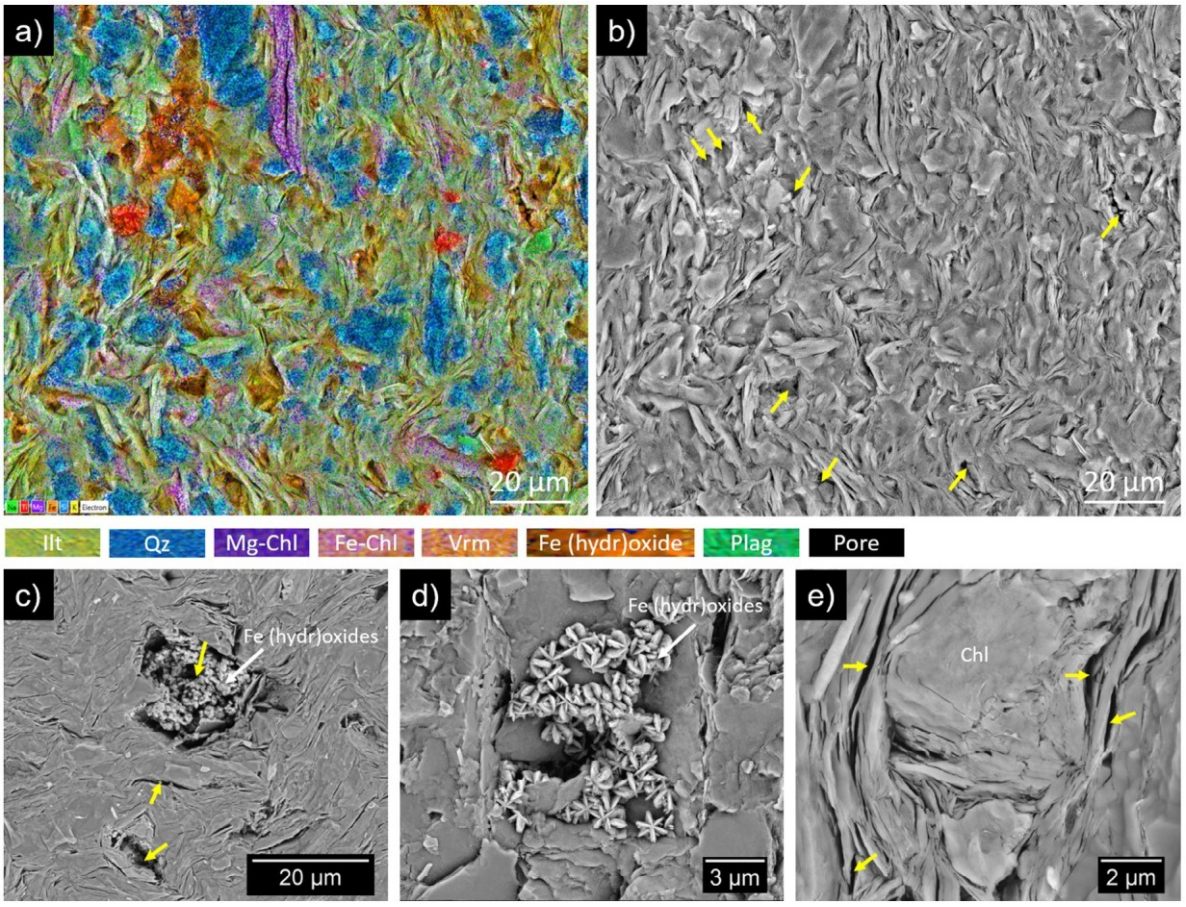

Fig. 8. X-ray elemental maps (a) and BSE images (b-e) of argon-ion-milled sections of weathered shale from SSHCZO (borehole CZMW8, 5.5 mbls) displaying the mineral dissolution and pore morphology. The elemental map (a) reflects a mixed backscattered electron and energy-dispersive spectroscopy signal. BSE image of the same area is shown in b. The yellow arrows mark examples of pore space. Micron-sized pores (yellow arrows) are likely generated through dissolution of chlorite, since the pores in b are primarily associated with chlorite and the weathering products of chlorite (e.g. vermiculite and Fe (hydr)oxide, shown in orange and brown in a). Fe (hydr)oxides (white arrows) were observed precipitated in the pore space in a flower-like morphology as shown in (c) and (d). Ilt: illite, Qz: quartz, Mg-Chl: Mg-rich chlorite, Vrm: vermiculite, Fe-Chl: Fe-rich chlorite, Plag: plagioclase.

porosity ($/_{epoxy}$ þ $/_{water}$) with pore size larger than 10 nm measured by the combination of neutron scattering and imaging matches the porosity measured by MIP (Fig. 10d).

Microfractures. For the protolith (or least weathered rocks for Fushan, e.g., the bottom-most borehole sample and the outcrop sample) at all three sites, a very small number of microfractures are observed under SEM (fracture porosity < 0.1%; Table 4). Likewise, only a few microfractures were observed in SEM images made for both weathered and unweathered samples (Fig. 9) recovered from the CZMW2, CZMW8 and DC1 boreholes at SSHCZO.

In contrast, microfractures are well developed in all rock chips sampled from the regolith above the pyrite depletion front at ERCZO and Fushan to the land surface (Fig. 9). At both ERCZO and Fushan, open microfractures were observed frequently while microfractures with Fe (hydr)oxide cement were observed less frequently (Fig. 9f, i, Table 4). The microfracture porosities directly measured from SEM images are in good agreement with the epoxy-accessible porosities ($/_{epoxy}$) derived from neutron scattering (Table 4).

5. DISCUSSION

5.1. Comparison of chemical weathering profiles as a function of erosion rate

One of the challenges of working across three different shale catchments that span such a large range in erosion rates is that drilling and sampling was not equivalent across all of them. For example, boreholes did not reach parent material and no borehole was drilled on a ridge at Fushan, in contrast to the availability of such boreholes at SSHCZO and ERCZO. Data on weathering mineralogy and chemistry from subsurface cores are scarce from rapidly eroding sites like Fushan, so although we face limitations when comparing the three sites, the sites nonetheless allow an evaluation of a range of erosional forcing across relatively similar shale bedrock that has been difficult to consider previously and that would be impossible based on other existing observatory sites or networks. Throughout, we emphasize similarities we see among the sites and extrapolate where it is defensible to the other sites.

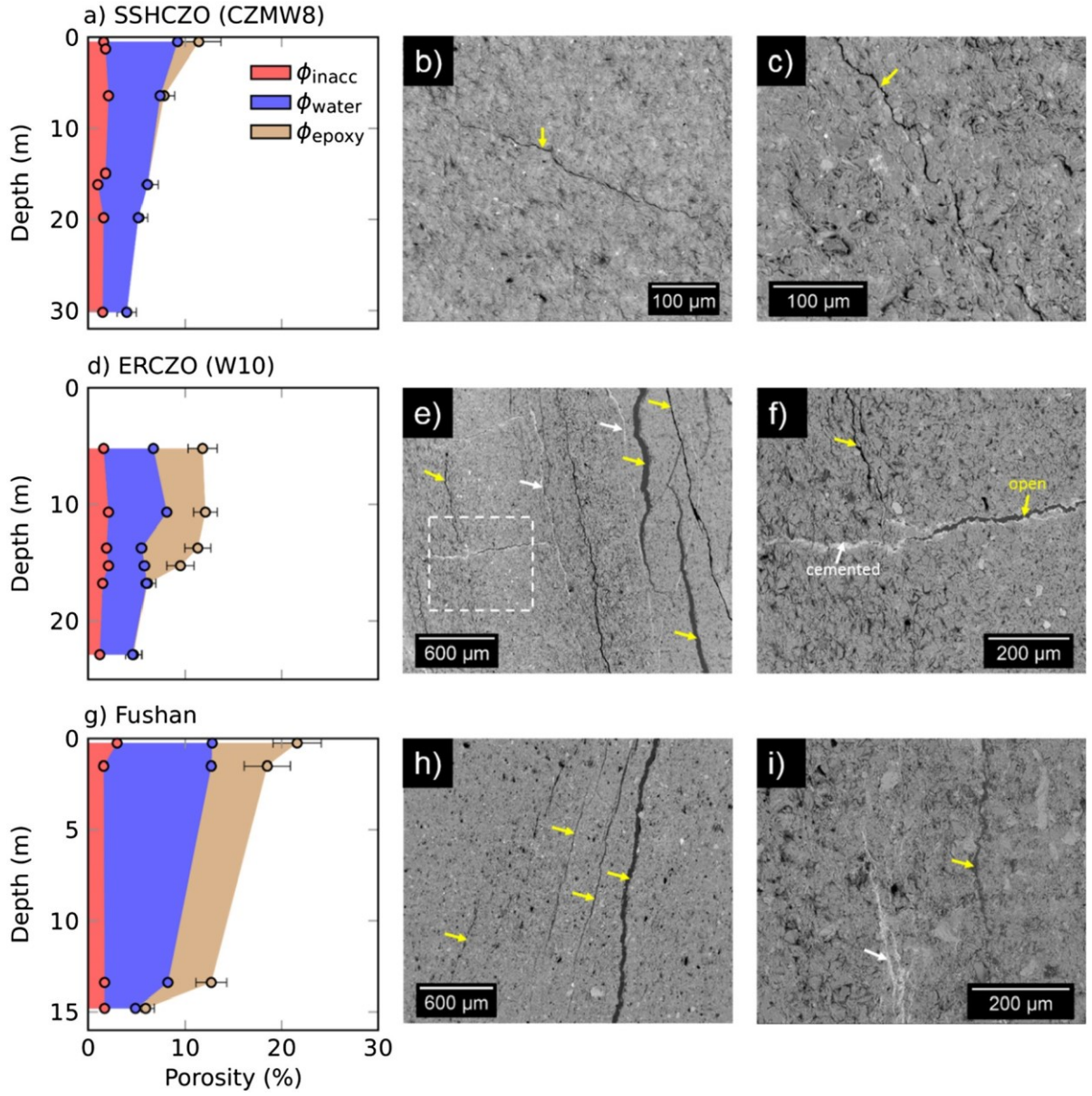

Fig. 9. The first column: change of porosity with depth for the various shale samples at a) SSHCZO, d) ERCZO and g) Fushan. The top two samples at SSHCZO are rock chips from a ridgetop soil core. The samples above 2 mbls at Fushan are rock chips from a soil core near the valley (FS1). All other samples were collected from boreholes. The second and third column: BSE images of weathered shales from SSHCZO (b, c), ERCZO (e, f) and Fushan (h, g) showing development of microfractures. b, c): Rock fragments collected from borehole CZMW8 at SSHCZO at 6.4 mbls (b) and 14.9 mbls (c). The microfractures is more isolated and is less commonly observed at SSHCZO as compared to other two sites. e, f): Rock chip collected from borehole W10 at 15.2 mbls at ERCZO. f: Microfractures cemented by Fe (hydr)oxides as shown in the zoom-in view of the dashed box in (e). h, i): Rock chip collected from 13.4 mbls from borehole FSC1 at Fushan. The yellow arrows mark examples of the open microfractures and the white arrows mark examples of the microfractures cemented by Fe (hydr)oxide. The rock chips were impregnated with epoxy, and the open microfractures are filled with epoxy (black in the images).

The weathering profiles at the three sites are similar in terms of the relative sequence of mineralogical transformation: pyrite and carbonate are the first two minerals to react and they react at such similar depths that it is not always possible to determine which one reacts first given the sample availability. In addition, at each site, the last of the rock-forming minerals observed to react is illite; this min- eral mostly begins to deplete in the soil at all three sites. The depletion profile for plagioclase and chlorite initiates between the pyrite and illite fronts under the ridges, in the two watersheds where ridge cores are available (Fig. 11a).

Nature and depth of the pyrite oxidation fronts. Another similarity at SSHCZO and ERCZO is the observation that the depth interval over which pyrite and carbonate react under the ridge is relatively narrow (1–2 meters) in compar-

Table 5
Summary of pore structure characteristics derived from MIP for samples from SSHCZO, ERCZO and Fushan.

Sample Type	Sample	Depth (mbls)	Bulk density (g cm^{-3})	Apparent density (g cm^{-3})	Porosity (%)	SSA (m^2 g^{-1})	P_c (MPa)[a]	d_c (nm)[b]	Calculated permeability (nD)[c]
Rock chip from a soil pit under ridge at SSHCZO	SSHCZO_RT-50	0.5	2.563	2.752	6.9	6.4	66	19	7.6
	SSHCZO_RT-130	1.3	2.577	2.744	6.1	6.6	89	14	3.3
Rock chip from borehole CZMW8 at SSHCZO	SSHCZO_CZMW8-21	6.4	2.620	2.755	4.9	5.9	86	14	2.2
	SSHCZO_CZMW8-49	14.9	2.630	2.745	4.2	4.5	88	14	1.6
	SSHCZO_CZMW8-53	16.2	2.684	2.747	2.3	2.8	120	10	0.3
	SSHCZO_CZMW8-65	19.8	2.711	2.746	1.3	0.3	62	20	0.3
	SSHCZO_CZMW8-99	30.2	2.718	2.751	1.2	0.8	99	13	0.1
Rock chip from borehole W14 at ERCZO	ERCZO_W14-9	2.7	2.480	2.642	6.1	3.6	63	20	6.6
	ERCZO_W14-60	18.3	2.460	2.662	7.6	2.6	46	27	18.9
Rock chip from borehole W15 at ERCZO	ERCZO_W15-26	7.9	2.466	2.636	6.5	4.8	75	17	5.1
	ERCZO_W15-85	25.9	2.652	2.719	2.5	1.4	76	16	0.7
Rock chip from soil core FS1 at Fushan	Fushan_S1A	0.25	2.230	2.753	19.0	7.4	20	62	629.1
Rock chip from borehole FSC1 at Fushan	Fushan_FSC1_2	14.8	2.561	2.649	3.3	5.4	169	7	0.3

[a] The breakthrough capillary pressure, estimated by identifying the inflection point on the cumulative porosity versus pressure curve (Fig. 9a–c).
[b] The critical pore throat size corresponding to the breakthrough capillary pressure, calculated from Eq. (2). Given the uncertainties of contact angle, the relative uncertainty of critical pore throat size is estimated as 10%.
[c] The permeability was calculated through Eq. (3).

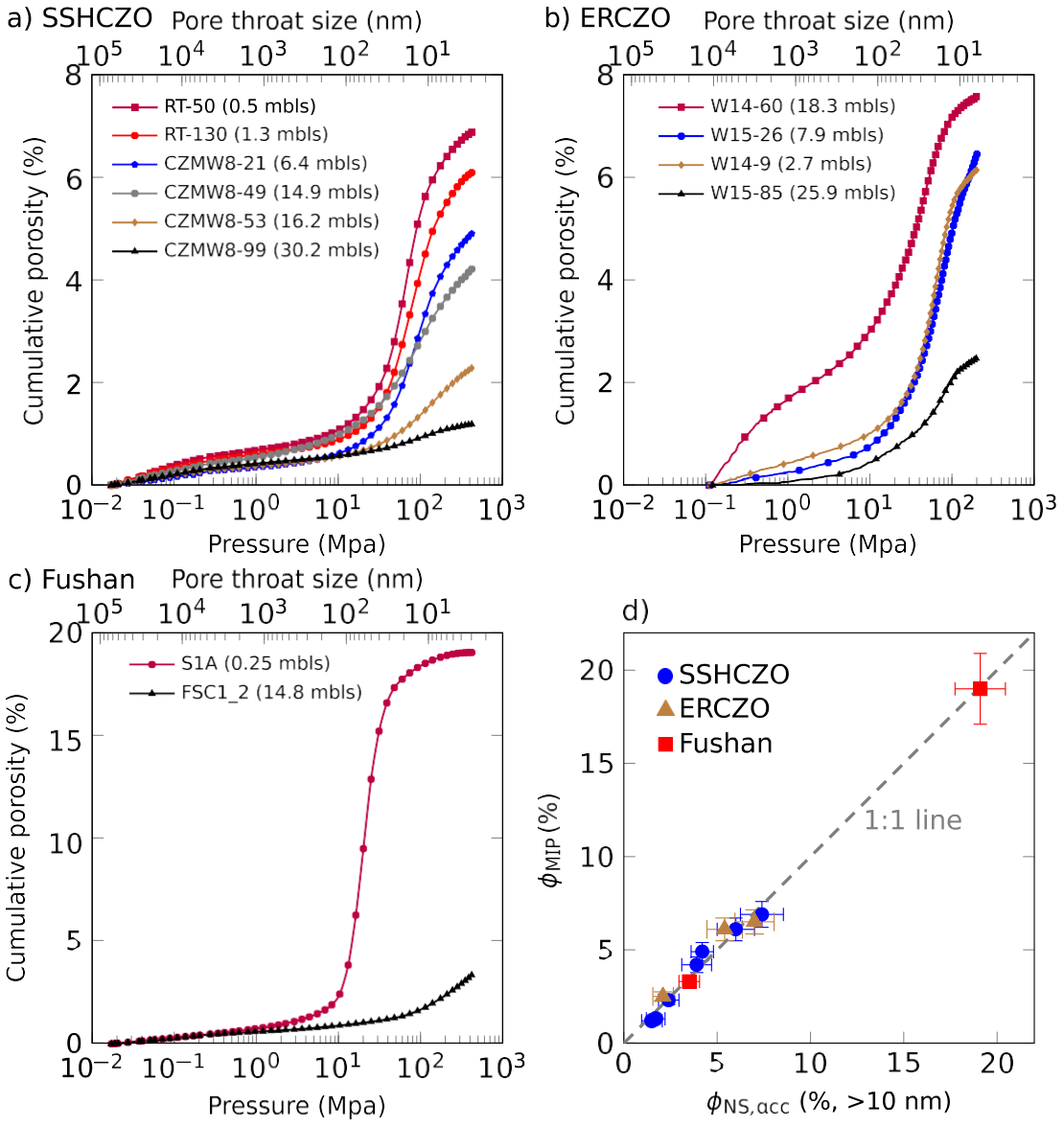

Fig. 10. Cumulative porosity as a function of mercury intrusion pressure (low axis) and pore throat size (upper axis) for the samples from a) SSHCZO, b) ERCZO and c) Fushan. d) Comparison between porosity determined by MIP ($/_{MIP}$) and fluid-accessible porosity determined by neutron scattering and imaging with pore size larger than 10 nm ($/_{NS;acc}$). Fluid-accessible porosity was calculated as the difference between total porosity and water-inaccessible porosity reported in Table 4. The error bars represent one standard deviation calculated through propagation of uncertainties reported in Table 4. Neutron scattering measurements for samples W15-26 and W14-9 at ERCZO were not available, thus the values of the measurements on two samples from the same borehole with similar depth (W15-31 and W14-16, respectively) were used. The relative uncertainties of MIP measurements were assumed to be 10%.

ison to the total depth of pyrite- and carbonate-depleted regolith (generally up to tens of meters at ridge crests). We were unable to assess the thickness of the reaction front under the ridge at Fushan because of lack of samples. Sharp reaction fronts form when the rate of reaction is relatively fast compared to the rate of transport of solutes through the reaction front (Lebedeva et al., 2010), and can occur when water flowpaths transition from vertical to horizontal because of a large contrast in permeability (Brantley et al., 2017). This is consistent with the observation that the reaction fronts of pyrite and carbonate mark a transition in porosity and, presumably, permeability.

Another similarity for SSHCZO and ERCZO is the observation that the pyrite front is co-located within or just above the interval of variation in depth of the water table under the ridges. This is likely not a coincidence but is instead explained because this zone of water fluctuation is where oxygenated gas is entrained into groundwater, promoting oxidation reactions, as described for other settings (e.g. Jones, 1985; Legout et al., 2007; Ayraud et al.,

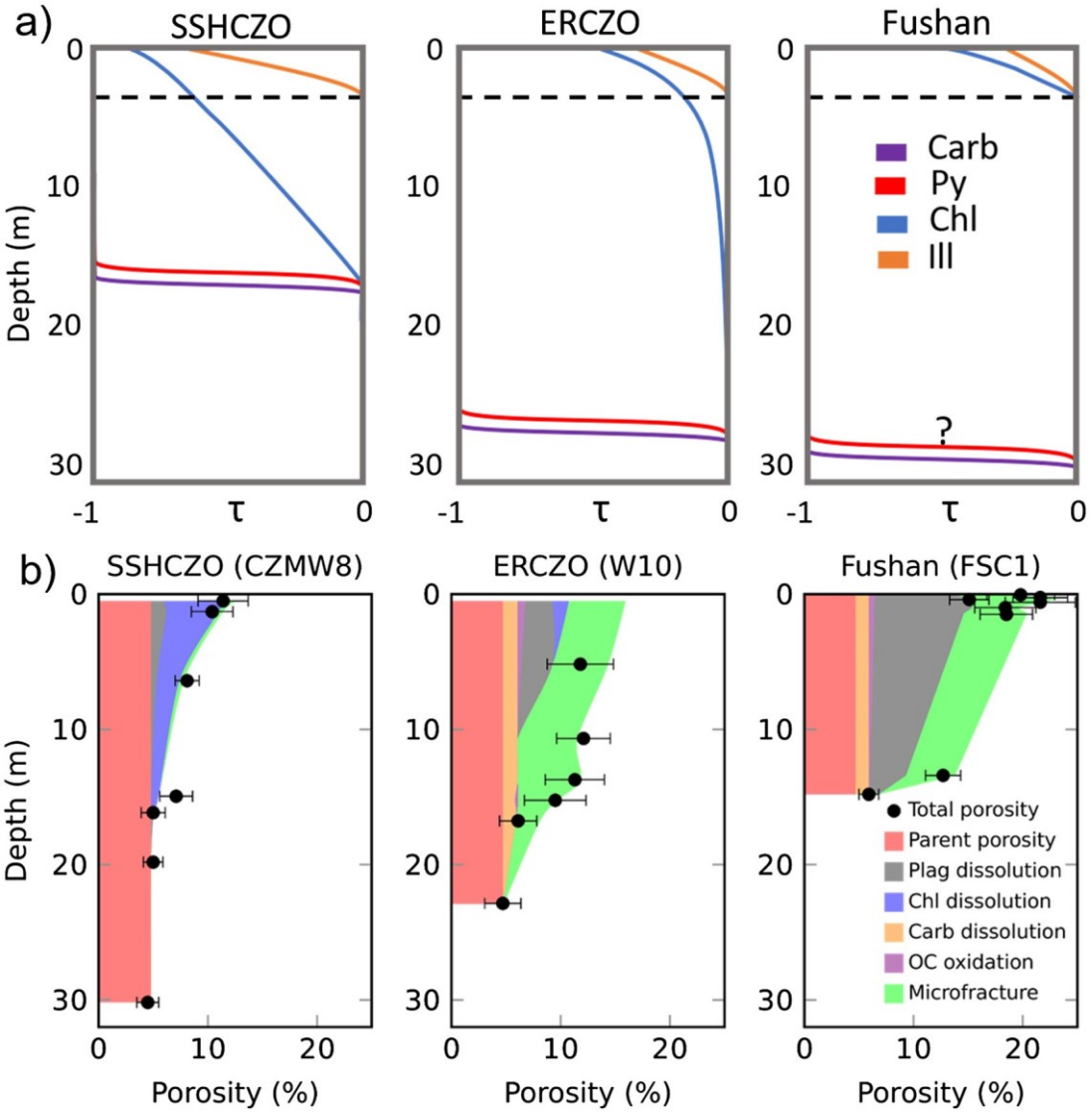

Fig. 11. (a) Schematics of the chemical weathering profiles under the ridges. The dashed line shows the saprock-soil interface. Tau (s) is a normalized concentration (Brimhall and Dietrich, 1987; Anderson et al., 2002). The depth of soil has been exaggerated in all profiles relative to the other layers. Profiles are shown for borehole CZMW8 at SSHCZO, and for W15 at ERCZO. Carbonate and pyrite at Fushan are completely depleted in all shale samples from the boreholes (15 m deep) located in the valley, and no samples from a borehole under a ridge were available. As discussed in text, it is not always possible to determine whether pyrite or carbonate depletion is the deepest, but carbonate depletion is shown here as deepest for simplicity. (b) Porosity evolution in rock chips during shale weathering as calculated for the three shales (see text). The total porosities of shales (black dots) were measured through neutron scattering and BSE imaging as described in text. The parent porosities are the averaged porosities of protolith at each location and porosities at other depths were estimated using Eq. (4). The volume fraction of microfractures were assumed equivalent to epoxy-accessible porosities ($/_{epoxy}$ in Table 4). The borehole at SSHCZO (CZMW8) is located under a ridge, the borehole at ERCZO (W10) is located on a hill slope and the borehole at Fushan (FSC1) is located under the valley. The top two samples at SSHCZO are rock chips from ridgetop soil and samples above 2 mbls at Fushan are rock chips from a soil core. All other samples are from boreholes.

2008). Co-location of pyrite oxidation with the depth of the variation in the water table under the ridge cannot be tested in Fushan because no borehole was drilled under the ridge.

The depths of pyrite oxidation in the stream channels in the three locations differ. Under the stream channels in the sites with lowest and highest erosion rates (Shale Hills at SSHCZO and Fushan), pyrite is depleted to meters beneath the outlet. In contrast, pyrite was observed in the bedrock outcropping in the bed of Elder Creek at the base of Rivendell (Fig. S4). Apparently, the pyrite weathering fronts record differences in drainage of oxygenated water through the bedrock at the base of the outlet in each location. At SSHCZO, Sullivan et al. (2016) argued that a significant fraction of the incoming precipitation at SSHCZO exits as subsurface flow well above the regional water table (termed by Sullivan et al. as interflow) and that this water is

oxygenated. They argued that interflow mixes with deeper O_2-poor groundwater under the catchment outlet to depths of 5–8 m but that pyrite nonetheless dissolves at meters of depth under the outlet. Similarly, Chang (2000) found that fast-moving subsurface flow, like the interflow invoked at Shale Hills by Sullivan et al., plays an import role in the generation of runoff at Fushan. At the outlet of Rivendell (at ERCZO) where it is truncated by Elder Creek, the bedrock underlying the stream is not intensely fractured and no evidence for shallow subsurface flow (interflow) has been observed. Instead, runoff exits hillslopes only as groundwater (Salve et al., 2012, Rempe and Dietrich, 2018). These hydrological differences may explain the differences in pyrite weathering the stream channels of each catchment, by determining the extent of reaction with O_2-bearing fluids in the subsurface.

Comparison of clay transformations. Chlorite is known to react and proceed through a transformation that progressively releases Mg and Fe during weathering. For example, Aspandiar and Eggleton (2002) showed that chlorite altered to corrensite in saprock, corrensite altered to vermiculite in saprolite, and vermiculite altered to kaolinite in fine saprolite in a weathering profile of basalt in Australia. They also found that the volume change from chlorite to vermiculite was small (1.4%), that Fe was released to significant extent during the vermiculite-kaolinite transformation, and that released Fe was precipitated in pore space as goethite.

It is likely that such sequential transformations of chlorite are also occurring at our three study sites but weathering does not proceed as far under fast erosion. Under ridges at SSHCZO and ERCZO, vermiculitization of chlorite is revealed by XRD analysis (Figs. 4, 5) to initiate at the same or shallower depths as pyrite depletion initiates. Mg loss occurs during this transformation and the Mg depletion (Figs. 4, 5) occurs across a depth interval (tens of meters) that is wider than the reaction front for pyrite (a few meters). These observations show a consistent pattern of lower extent of chlorite weathering with higher erosion rate: (1) weathering results in a greater depletion of Mg in chlorite grains at SSHCZO and ERCZO than at Fushan; (2) secondary minerals formed from chlorite are observed at SSHCZO and ERCZO but not at Fushan (Fig. S2); (3) pores generated through vermiculite dissolution are observed at SSHCZO but not at ERCZO nor Fushan; and 4) flower-like iron (hydr)oxides, likely precipitated from Fe released during vermiculite dissolution, are observed in the pore space at SSHCZO but not at ERCZO nor Fushan (Fig. 8c, d). Thus, the depletion of Mg and Fe and the nature of secondary minerals generated varied across the three catchments. The result is that unlike weathering of pyrite and carbonate, in which the depletion completes at tens of meters deep under ridges at all three sites, the extent of chlorite weathering observed at the land surface follows the order SSHCZO > ERCZO > Fushan.

In contrast to chlorite that was observed to begin to weather in saprock at SSHCZO and ERCZO, depletion of illite was not observed in any of the three sites in rock chips recovered from boreholes nor from the soil, and was only detected to occur in disaggregated soil particles (Figs. 4–6, Table 2). It is possible that dissolution of illite contributes directly to disaggregating the rock to form soil because illite is the matrix mineral in the shales (Fig. 2). Similar to weathering of chlorite, the extent of illite weathering observed at the land surface follows the order SSHCZO > ERCZO > Fushan.

5.2. Relating porosity, microfractures, pore throat size, weathering, and infiltration

As connected pore space grows, permeability can increase and fluid infiltration can accelerate. Fluid flow in turn promotes chemical weathering (Lebedeva et al., 2010; Maher and Chamberlain, 2014). Porosity generation also tends to decrease rock strength, promoting physical weathering and disaggregation into smaller particles that are more weatherable and more erodible. As a result, porosity generation influences both erosion rates at the land surface and regolith formation rates at depth.

Here, we consider what causes changes in porosity in the shales as they weather. We partition the porosity measured in shale rock chips to (i) the parent porosity (ϕ_p), (ii) porosity generated through microfracturing (ϕ_f), and (iii) porosity generated through the net result of primary mineral dissolution and secondary mineral precipitation (ϕ_j). The parent porosities (ϕ_p) were assumed equal to the averaged porosities of assumed protolith at each site. The porosity generated through microfracturing (ϕ_f) was assumed to be equivalent to the epoxy-accessible porosities (ϕ_{epoxy} in Table 4). The porosity generated through primary mineral dissolution and secondary mineral precipitation (ϕ_j) was calculated assuming the shales weather isovolumetrically using:

$$\phi_j = -\varepsilon_{ij} V_j - V_k \qquad (4)$$

We completed these calculations based on the analyses of rock fragments/chips (not for the granular soil), and thus the assumption of isovolumetric weathering is defensible. In addition, the observation of pseudomorphism for the pyrite to Fe (hydr)oxide transformation attests to isovolumetric reaction. Here, the porosity generated by mineral j (ϕ_j) as it weathers to secondary mineral k was calculated from V_j and V_k, the volume fractions of mineral j in parent rock and mineral k in weathered rock and the appropriate tau value for mineral j in weathered rock. For congruent reactions, e.g., carbonate dissolution, $V_k = 0$. The transformation of chlorite to vermiculite, pyrite to Fe (hydr)oxide, and plagioclase to kaolinite was assumed to be isovolumetric following observations from the literature for similar systems (White et al., 2001; Aspandiar and Eggleton, 2002). As shown in Fig. 11b, the summation of initial parent porosity, porosity generated through mineral dissolution, and porosity from microfractures is roughly in agreement with the total porosity measured with neutron scattering and BSE imaging for each site (black dots in Fig. 11b). This observation also lends credence to the assumption of isovolumetric weathering.

The figures show that the reactions that generate most of the porosity differ at the three sites (Fig. 11b). At SSHCZO,

nearly all porosity (other than protolith porosity) was generated in the rock fragments/chips by chemical dissolution, especially for chlorite. At ERCZO, in contrast, chemical dissolution (mainly carbonate and plagioclase) contributed less than 40% of the total porosity and the rest was generated by formation of microfractures (as shown in the SEM images in Fig. 9). At Fushan, plagioclase dissolution and microfracturing contributed 40–60% and 30–50% of the generation of porosity, respectively (the rest is attributed to dissolution of carbonate and oxidation of organic matter).

Although the porosity in rock fragments/chips at SSHCZO increased two- to three-fold from protolith to weathered rock, the critical pore throat size measured by MIP remained constant (Table 5). It is therefore likely that pore throats continue to limit fluid flow into the shale matrix even in the weathered shale. In contrast, if we consider the deepest and lowest porosity sample from borehole W15 at 25.9 mbls as protolith, the average porosity and the critical pore throat size in weathered rock at ERCZO are 2.7 and 1.3 times higher than those in protolith, respectively. At Fushan, both the porosity and the critical pore throat size of rock chips increased more than fivefold during weathering (Fig. 10, Table 5). It is likely that the increase in inferred pore throat size in weathered rock at ERCZO and especially at Fushan is caused by the microfracturing. Apparently, in shales that exhume slowly in temperate climates such as the shale in SSHCZO, microfractures do not form (or form and heal at the same rate), the pore throat size remains constant, and little meteoric fluids enters the low-porosity matrix. The rock matrix only opens up to significant water flow when the matrix-forming clay minerals begin to dissolve (in the disaggregated soil). On the other hand, in shales that exhume at a higher rate in a wetter climate, microfractures open and pore throat size increases at depth, allowing more meteoric fluid to interact with matrix grains and decreasing the size of diffusion-limited internal matrix domains (Zachara et al., 2016).

5.3. Possible causes of microfracturing

These arguments are consistent with microfractures as the dominant microstructural feature that accelerates chemical weathering in ERCZO and Fushan. But this inference begs the question: why do the microfractures form? Microfractures are produced in shale when the stress experienced by the rock exceeds the local strength of the rock matrix. Such failure is a complex function of the mineral and organic carbon content, the fabric, and the geological history (Ougier-Simonin et al., 2016). Fracture propagation at near-surface depths usually occurs at stresses lower than critical stresses, i.e. lower than the tensile stress or fracture toughness (Anderson, 2019). Propagation can thus be described as subcritical cracking, and this type of cracking is time-dependent and environment-sensitive (Atkinson, 1984; Eppes and Keanini, 2017). The first order controls on subcritical cracking are the magnitude of applied stress (topographic, tectonic, and environmental) and the numbers and sizes of inherent flaws in the rock — pores, grain boundaries, or mineral cleavage planes. A second order set of controls on fractures is the set of environmental factors that weaken the chemical bonds at fracture tips. For example, the rate of subcritical cracking typically increases with increasing water content (both humidity and liquid water content) and temperature (Waza et al., 1980; Wells et al., 2005; Heap et al., 2009).

Given the differences in topographic, tectonic, and environmental conditions in the three shale study sites, several reasons could explain differences in microfracturing. These are explored below.

Characteristics intrinsic to the shale. One characteristic that is intrinsic to the shales and possibly important in terms of microcracking is the nature of the clay minerals. Specifically, the relative abundance of phyllosilicates could explain the presence or absence of microcracking. In this regard, the high concentration of micrometer-sized phyllosilicates at SSHCZO (>40%) is likely to enhance the shale's ability to self-seal or -heal after microfracturing. Using an ideal packing model, Bourg (2015) predicted that shale with more than 1/3 clay mineral content has a greater tendency to self-seal because the clay matrix is the load-bearing phase. In fact, the shale from SSHCZO contains more than 40% illite, while the shale from ERCZO contains ~ 27% micron-sized phyllosilicates (illite + kaolinite + smectite), and the shale from Fushan contains ~33% illite (Table 2). Thus, the Rose Hill shale from SSHCZO is more likely to self-seal than shale from the other sites.

The differences in smectite content might also affect microfracturing in these rocks. Hydration-dehydration cycling of smectite causes volume changes, and both Fushan and ERCZO shales have slightly more smectite than SSHCZO (Kim et al., 2014; Table 2). However, swelling minerals have also been observed to accelerate self-sealing rather than accelerate cracking under confinement (Davy et al., 2007; Zhang and Rothfuchs, 2008). Therefore, the existence of swelling minerals does not necessarily point to more microfracturing at ERCZO and Fushan. The lower overall clay abundance may be a better explanation for the microfracturing.

Tectonic and erosional history. The shales at Fushan and ERCZO experienced more tectonic deformation than SSHCZO prior to exposure, and this may contribute to formation of microfractures. Exhumation can also create residual stresses because of the elastic response of rock to unloading (Nadan and Engelder, 2009). The magnitude of this stress is a function of the magnitude and orientation of tectonic stresses, the geologic history, the mechanical properties of the rock, and the local topography (Leith et al., 2014; Slim et al., 2015). In addition, the elastic response of rock to unloading is time dependent (Ten Cate and Shankland, 1996) and the slow rate of erosion at SSHCZO could allow relaxation of stresses developed during exhumation. Thus, the faster the rocks are exhumed, the more residual stresses might be maintained.

Quantitative modelling of such stresses at these three sites is beyond the scope of this paper, but the high residual tensile stresses expected to develop during rapid exhumation in the two fast-eroding sites could conceivably cause the microfracturing (Leith et al., 2014). Likewise, the differ-

ential stress induced topographically at ERCZO and Fushan with the steeper slopes and greater relief could be high enough to fracture intact bedrock (Molnar et al., 2007). However, as Moon et al. (2017) have pointed out, how topography influences fracture opening is sensitive to the magnitude and orientation of tectonic stress relative to the topographic stress. Further investigation on the stress field beneath these landscapes is needed to elucidate the fracturing mechanism.

5.4. Coupling between weathering and erosion

As shown in Fig. 11a, the depletion profiles of pyrite and carbonate are completely developed (i.e., the minerals become 100% depleted) at all three sites regardless of erosion rate. The extent of weathering of rock-forming clays (illite and chlorite) at the land surface, on the other hand, decreases with increasing erosion rate. The difference in dissolution kinetics of minerals in shale likely explains why the weathering profiles of minerals differ. Many authors have pointed out that in landscapes with high erosion rate, the chemical weathering rate might be limited by dissolution kinetics while in landscapes with low erosion rates, weathering rate might be limited by the supply of fresh materials through erosion (Stallard and Edmond, 1983; West et al., 2005; Lebedeva et al., 2007, 2010; Ferrier and Kirchner, 2008; Gabet and Mudd, 2009, etc.). In geochemical transport models it has been shown that the extent of weathering of a reactive mineral at the land surface can decrease with increasing erosion rate (White et al., 2008; Lebedeva et al., 2010). This is consistent with our observations here for chlorite and illite. The dissolution rates of pyrite and carbonate are several orders of magnitude higher than silicate minerals; therefore, it is likely that the weathering of pyrite and carbonate, both of which are characterized by completely depleted weathering profiles in the regolith, is not limited by dissolution kinetics, while the weathering of clay (chlorite and illite) is limited by dissolution kinetics. Thus, the observations for the four minerals in the weathering profiles across our watersheds (Fig. 11a) are consistent with general features of predicted profiles (see for example, Lebedeva et al., 2010).

The incompletely developed and completely developed profiles shown in Fig. 11a can also be related directly to weathering-derived release of solutes out of catchments (Brantley and White, 2009). As shown in Fig. 12, the theoretical relationship between solute flux from different minerals and erosion rate depends on the dissolution rate of the minerals. Specifically, for minerals weathering in an erosion transport-limited regime (such as pyrite and carbonate) where the weathering rate is not limited by the reaction rate, the weathering profiles become completely developed (i.e., minerals are 100% depleted at the land surface) and the weathering rate is directly proportional to the erosion rate; in contrast, for minerals weathering in the kinetic-limited regime (such as chlorite and illite) where the weathering rate is limited by mineral reaction kinetics, the weathering profiles become incompletely developed and the weathering rate is not able to keep up with the erosion rate (Fig. 12). These generalizations are consistent with

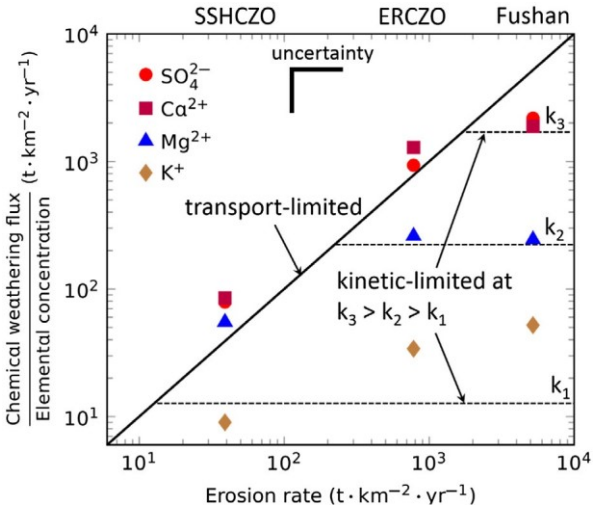

Fig. 12. Chemical weathering flux as a function of erosion rate in regimes limited by erosive removal of material (labelled ''transport-limited") and by weathering kinetics (labelled ''kinetic-limited"). The diagrams are reproduced from the analytical solutions of a reactive transport model (Lebedeva et al., 2010). The slanted, solid line on the diagram indicates the transport-limited regime where the chemical weathering fluxes normalized to elemental concentration in protolith for all solubilized elements are identical to erosion rate (1:1 line) and do not depend upon the rate constant for mineral dissolution. In contrast, the horizontal, dashed lines indicate the kinetic-limited regime where the chemical weathering fluxes are not able to keep up with erosion rate. Three different generalized chemical weathering fluxes are shown as described by rate constants $k_3 > k_2 > k_1$. Solute fluxes (normalized to elemental concentration in protolith) for SO_4^{2-}, Ca^{2+}, Mg^{2+} and K^+ estimated from stream water chemistry are plotted as solid dots as a function of erosion rate for the three study sites (data summarized in Table S2). The erosion rate ($t\ km^{-2}\ yr^{-1}$) at each site was calculated as the product of erosion rate (mm yr^{-1}, Table 1) and bulk density of protolith (assuming to be 2.6 g cm^{-3}). Pyrite (sulfate) and carbonate (Ca) plot in the transport-limited regime, and chlorite (Mg) and illite (K) plot in the kinetic-limited regime. These observations are consistent with completely developed profiles for fast-reacting pyrite and carbonate, and incompletely developed profiles for slow-dissolving chlorite and illite in regolith at all three sites (Fig. 11a). The data also are consistent with faster rates of dissolution for chlorite than illite ($k_2 > k_1$). The figure is schematic in that only estimates of rate constants (not measured values) are plotted.

observations of high weathering fluxes for carbonate and pyrite in rapidly eroding terrains (Torres et al., 2016), but fluxes from weathering of silicate minerals that do not track with erosion rate because of kinetic limitation (Jacobson et al., 2003; West et al., 2005).

Why do the weathering advance rates and chemical weathering fluxes of pyrite and carbonate increase with erosion rate? The natural experiment described here is not perfect because we did not isolate the effect of erosion from that of climate. One reason for the acceleration of weathering could be that weathering rates increase with precipitation (White and Blum, 1995). However, White and Blum (1995) observed that weathering rates only increase linearly with precipitation; thus, the higher rainfall at ERCZO and

Fushan (Table 1) is likely to explain some, but not all the acceleration. Temperature could also enhance the weathering rate. However, for minerals weathering in an erosion transport-limited regime, the temperature effect is minimal (West et al., 2005; West, 2012; Maher and Chamberlain, 2014). Another answer could be that the faster rates of weathering advance at the faster eroding sites are caused by the increasing density of microfractures as we have observed in this study (Fig. 9). Specifically, the microfractures in ERCZO and Fushan could accelerate the propagation of the weathering front by enhancing permeability and thus the infiltration of oxygenated meteoric water into the deep shale. Such increased infiltration likely i) increases the concentration of oxygen in the fracture porefluids and ii) decreases the size of the internal domains of matrix characterized by diffusion-limited nanoporosity (Zachara et al., 2016). Increasing weathering advance rates with increasing fracture density is expected on theoretical grounds (Lebedeva and Brantley 2017).

If the higher density of microfractures is caused by the higher erosion rate at Fushan and ERCZO and the higher fracture density explains the faster weathering advance rates, then the increasing rates of weathering of pyrite and carbonate from SSHCZO to ERCZO to Fushan are ultimately the result of the more tectonically active geological setting of the latter two sites. In other words, in this case the higher tectonic activity might ultimately explain density of microfractures. But an additional factor could be that the fractures are not annealed during the small residence times in the weathering depth intervals in fast eroding sites whereas microfractures anneal as fast as they open in catchments such as SSHCZO. Regardless, microfractures are likely to be an important determinant of the weathering rates of shale catchments.

6. CONCLUSIONS

In this study, we investigated the characteristics of weathering of shales of similar composition at three sites experiencing different rates of erosion. Regardless of the differences in climate and erosion rate, the chemical weathering patterns are remarkably similar: pyrite and carbonate are 100% depleted down to tens of meters below the soil; illite is not depleted to great extent in the weathered bedrock, but begins to deplete significantly in the soil layer; and the initiation of the depletion profiles for chlorite and plagioclase lies between the pyrite and illite fronts. Thus, oxidation of pyrite and dissolution of carbonate marks the beginning of overall weathering and dissolution while illite remains unreactive until it enters the chemically reactive soil. In contrast, the mechanisms causing most of the porosity formation are different at these three sites: most porosity in rock chips was generated through chemical weathering (primarily chlorite dissolution) at SSHCZO whereas plagioclase weathering dominates porosity generation at Fushan and contributes significantly at ERCZO. In addition, more than 1/3 of the generated porosity is contributed by microfracturing at ERCZO and Fushan.

Microfractures, possibly related to prior tectonic deformation, high rigid grain concentration, and rapid exhumation at the ERCZO and Fushan sites, may couple rates of chemical erosion to physical erosion. Further study of the role of these microfractures in regulating the propagation of the regolith-bedrock interface is needed to model the interplay between climate, tectonics, and weathering.

ACKNOWLEDGEMENTS

Access to the small-angle neutron scattering instruments was provided by the Center for High Resolution Neutron Scattering, a partnership between the National Institute of Standards and Technology and the National Science Foundation under Agreement No. DMR-1508249. XG acknowledges help and advice on neutron scattering from David F.R. Mildner, David Cole, and Gernot Rother. XG and SLB acknowledge funding from DOE OBES DE-FG02-OSER15675 and NSF Critical Zone Observatory grants NSF, United States 12-39285 and 13-31726 for support for working on the Susquehanna Shale Hills Critical Zone Observatory in The Pennsylvania State University, United States Stone Valley Forest, which is funded by the Penn State College of Agriculture Sciences and the Department of Ecosystem Science and Management, and is managed by the staff of the Forestlands Management Office. WED and DMR acknowledge support from the Keck Foundation, National Science Foundation Grant NSF, United States 1331930 for the Eel River Critical Zone Observatory, the Angelo Coast Range Reserve and the University of California Reserve System, and the National Center for Airborne Laser Mapping. Ben Houlton, Randy Dahlgren, and Scott Mitchell (University of California, Davis) are thanked for sharing NSF-funded elemental analysis data for the Eel River CZO. The Taiwan Forestry Research Institute (TFIR) is thanked for help organizing sampling and allowing access to the Fushan site. SLB acknowledges M. Lebedeva for insights and three reviewers are thanked for their comments.

APPENDIX A. ASSESSING FLUID-ACCESSIBLE POROSITY BY NEUTRON SCATTERING

Combined small-angle neutron scattering (SANS) and ultra-small-angle neutron scattering (USANS) enables the characterization of the pore structure from ~1 nm to ~10 μm in pore dimension. SANS and USANS have been extensively applied to geomaterials (e.g., Radlinski, 2006; Anovitz and Cole, 2015). Prior to scattering, an H_2O-D_2O mixture can be introduced into the porous material to match the scattering contrast between the connected (fluid-accessible) pores and the mineral matrix, so that the only observed scattering intensity is characteristic of the unconnected (fluid-inaccessible) pores. This technique is known as contrast matching. Here, we rely on scattering length density, SLD, to interpret pore structure. Gu et al. (2015) demonstrated that SLD is sensitive to pores in shales, and the effect of mineral structure is negligible.

We prepared two sets of thin sections, one cut through rock without epoxy impregnation and another cut after impregnation. Both sets were measured before and after contrast matching. The contrast matching experiment was conducted by saturating thin sections with solutions of non-deuterated and deuterated water mixed with the same SLD as the rock matrix (Jin et al., 2011; Gu et al., 2016). Fluid transport in shale rock matrix is dominated by diffu-

sion, while flow in shale microfractures is dominated by advection (Pearson, 1999). Due to the difference in viscosity between water and epoxy, the accessible porosities for different intrusion fluids are different. Based on published observations, we assume that epoxy mainly enters connected microfractures but not matrix pores (Gentier et al., 1989; Nishiyama and Kusuda, 1994). In contrast, water could diffuse into connected microfractures and matrix pores, including small inter-particle, intra-particle and interlayer pores primarily associated with clay minerals (Allen, 1991; Kuila et al., 2014). Water in interlayer space of clay minerals was found to exchange with atmospheric water in a few hours (Savin and Epstein, 1970). Therefore, the water in interlayer space could exchange with the mixture of H_2O-D_2O during contrast matching experiment (saturated in an H_2O-D_2O mixture for 1 week) and the interlayer pores are water-accessible (Allen, 1991; Gu et al., 2015).

Therefore we defined three classes of porosity based on fluid-accessibility: (i) epoxy-accessible pores ($/_{epoxy}$), which is assumed to include mainly microfractures (as show in Fig. 9), (ii) epoxy-inaccessible but water-accessible pores ($/_{water}$), and (iii) fluid-inaccessible pores ($/_{inacc}$), i.e. isolated pores that are not accessible to water after contrast matching.

Because the SLDs of epoxy-filled, H_2O-filled and empty pores are all close to zero, the ''dry" measurements (before contrast matching) on both sets of thin sections (raw and epoxy-impregnated) from the same sample resulted in almost identical scattered neutron intensity. The porosities derived from the ''dry" measurements ($/_{dry}$) include all three classes of porosity (where the three types represent porosities (i), (ii) and (iii) listed above):

$$/_{dry} = /_{epoxy} + /_{water} + /_{inacc} \quad (A1)$$

Water accessible pores, when saturated with such H_2O-D_2O mixture, are undetectable because no scattering occurs from the water-pore interface. However, in the epoxy-impregnated samples, pores that are occupied by epoxy are not accessible to the H_2O-D_2O mixture. Thus, the porosity derived from the ''wet" measurements (after contrast matching) on epoxy-impregnated samples ($/_{wet;\ epoxy\text{-}im}$) includes both fluid-inaccessible and epoxy-accessible porosity:

$$/_{wet;\ epoxy\text{-}im} = /_{inacc} + /_{epoxy} \quad (A2)$$

and the porosities derived from the ''wet" measurements on raw samples ($/_{wet;\ raw}$) include only fluid-inaccessible porosity:

$$/_{wet;\ raw} = /_{inacc} \quad (A3)$$

Thus, a combination of four measurements – on both raw and epoxy-impregnated samples before and after contract matching (''dry" and ''wet") – were used to quantify the three classes of porosity through the solution of linear equations (A1)-(A3).

To assess pores or microfractures larger than 10 μm, we followed Radlinski et al. (2004) and Anovitz et al. (2013) and combined neutron scattering data with autocorrelation data obtained from backscattered electron (BSE) images. In general, the one-point (S_1) and two-point probability function (S_2) in a two-phase random medium can be expressed as:

$$S_1 = \langle f(x) \rangle = / \quad (A4)$$

$$S_2(r) = \langle f(x) f(x+r) \rangle \quad (A5)$$

where angular brackets denote spatial averaging, $f(x)$ is an indicator function, defined as $f(x) = 1$ for the pores and 0 for the solid, $/$ is the porosity, and r is a lag distance. S_2 depends only on the lag distance but not on the specific location of the individual points. At least ten grayscale BSE images magnified between 750× to 5000× for each sample were collected, and then thresholded manually in ImageJ to create a binary image of mineral grains and pores/microfractures (Abramoff et al., 2004, Anovitz and Cole, 2015). The two-point probability function was calculated through the radial integration of the power spectrum of the Fourier Transform of the image (Anovitz et al., 2013). The autocovariance, $v(r)$, and autocorrelation coefficient function, $c(r)$, are linear functions of the two-point probability function:

$$v(r) = S_2(r) - /^2 \quad (A6)$$

$$c(r) = \frac{v(r)}{/(1 - /)} \quad (A7)$$

The normalized scattering intensity is proportional to the Fourier transform of the autocorrelation coefficient function (Debye and Bueche, 1949; Anovitz et al., 2013):

$$I(Q) = 4\pi(\Delta\rho)^2 /(1 - /) \int_0^1 r^2 c(r) \frac{\sin(Qr)}{Qr} dr \quad (A8)$$

Here, $(\Delta\rho)^2$ is the contrast of scattering length density between minerals and pores. By combining the scattering information derived from BSE images with the neutron scattering data, the lower limit of Q can be extended to 10^{-7} Å^{-1}, which corresponds to a length scale of approximately 1 mm. The extrapolation of neutron scattering data with BSE images was applied only to the measurements of dry samples (I_{dry}), and the pores larger than 10 μm calculated from I_{dry} were assumed to be epoxy-accessible.

APPENDIX B. GEOCHEMISTRY OF THE PROTOLITH

For SSHCZO, the parent was estimated from a composite sample of protolith from three boreholes (DC1 under the northern ridge, CZMW2 under the valley, and CZMW8 under the southern ridge as shown in Fig. 1b). The carbonate concentration in protolith from each borehole shows high variability (Brantley et al., 2013). Therefore, the standard deviations of the elements enriched in carbonate minerals such as Ca, inorganic carbon (IC) and Mn were 60–80 percent around the mean. In contrast, the standard deviation around the mean concentration was smaller than 15 percent for all other elements except P, an element found in extremely low concentrations (Fig. B1).

Similar to SSHCZO, the parent composition for ERCZO was determined as the average of the protolith from five boreholes that all retained relatively high S con-

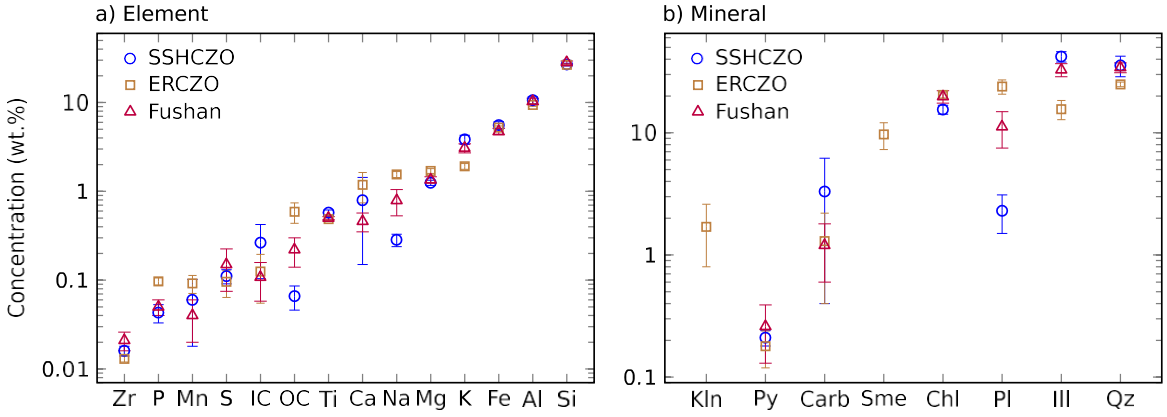

Fig. B1. Elemental (a) and mineral (b) abundance of protolith in the study sites. Mineral compositions were quantified by XRD semi-quantitatively (Qz: quartz, Ill: illite, Pl: plagioclase, Chl: chlorite, Sme: smectite, Carb: carbonate, Py: pyrite, Kln: kaolinite). Pyrite concentrations at SSHCZO and ERCZO were estimated through measurement of total S. Pyrite concentration at Fushan was estimated from the area fractions of the Fe (hydr)oxide framboids in thin sections of the bottom-most shale (see Appendix C). The estimation of parent is discussed in Appendix B.

centrations (W3, W10, W14, W15, and Elder Creek as shown in Fig. 1c). Similar to SSHCZO, the variation of Ca and IC is larger in these samples than for other elements, again likely indicating the heterogeneous distribution of carbonate in the protolith.

The bottom-most sample (Fushan_FSC2_1) from the two valley boreholes at Fushan contained 0.14 wt.% S but was very sand-rich (Fig. B2) and the elemental composition (Fig. S5) differed from all other samples from Fushan. This bottom-most layer was therefore inferred to be a sandstone layer (known to be present in the Kankou Formation) and was not used to estimate parent for the overlying shale. Instead, the parent composition of shale at Fushan was determined as the average of samples from outcrops where visibly unweathered bedrock was exposed. The concentrations of total carbon in the outcrop samples are significantly higher than those in the samples from drilled boreholes and soil pits. The pyrite content was esti-

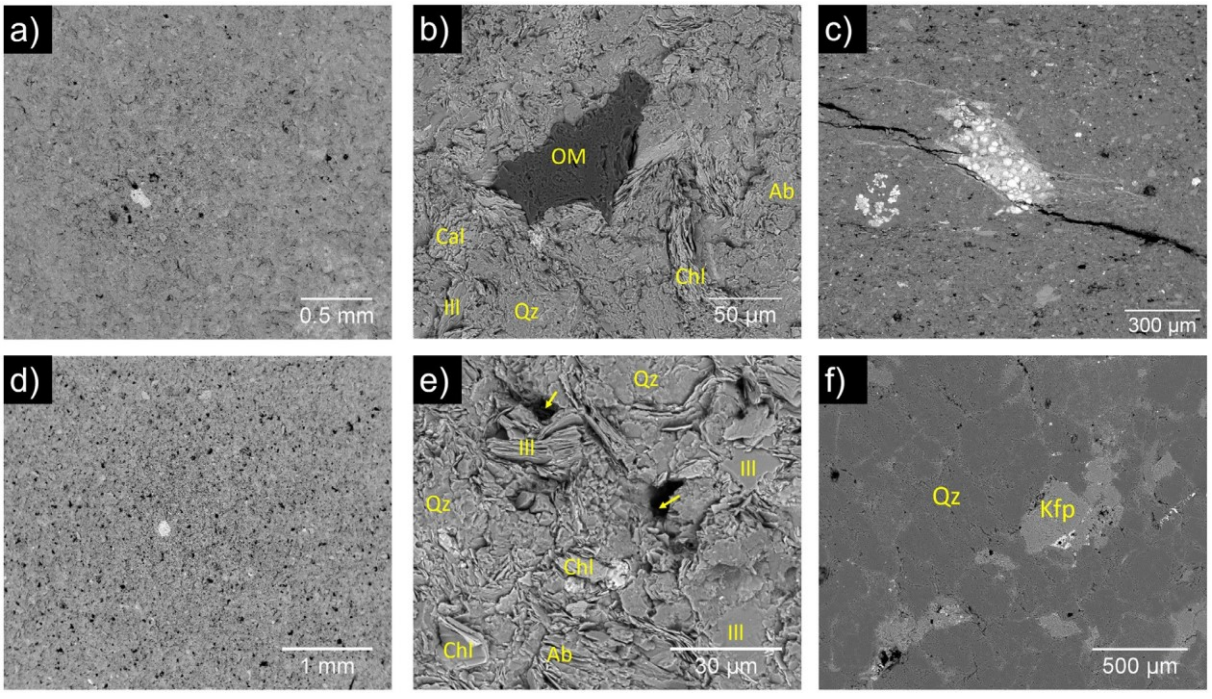

Fig. B2. BSE images of samples from Fushan. Shale samples from outcrops (a, b: Fushan_FSR1 and c: Fushan_FSR6), are less porous than the bottom-most shale sample from the borehole (d, e: Fushan_FSC1_2). A large amount of pyrite framboids was observed in the outcrop sample Fushan_FSR6 (c). The texture of the bottom-most sample from borehole FSC2 (f: Fushan_FSC2_1) is very different from the other shale samples and was assumed to derive from a sandy layer. The pore space in this sandy sample is cemented by K-feldspar and thus the porosity is very low (~1.8% measured by neutron scattering). Mineral labels are Ab: albite; Chl: chlorite; Kfp: K-feldspar; Ill: illite; OM: organic matter; Qz: quartz. The yellow arrows mark some examples of the pore space.

mated as described in Appendix C because of the absence of S in all samples except the sample from outcrop FSR6. The sampled rock chip from one outcrop (Fushan_FSR1) contain similar elemental concentrations, but higher calcium as compared to other outcrop samples (Table 2) and appeared to have fewer dissolution features under SEM (Fig. B2); therefore, the parent calcium concentration (as well as the concentrations of IC and carbonate) was estimated from this outcrop sample.

The elemental abundances in the inferred parent materials from the three sites are similar (Fig. B1). The higher concentrations of organic carbon (OC) in the bedrock from ERCZO and Fushan make the bedrock from these two sites black in color while the bedrock from SSHCZO is olive-gray. The primary minerals identified by XRD in the parent at all three sites are quartz (Qz), plagioclase (Pl), illite (Ill), chlorite (Chl) and carbonate (Carb, including calcite and/or dolomite or ankerite).

A few differences in parent materials among three sites are noted. The shales from ERCZO and Fushan have higher Na and plagioclase concentrations than shale from SSHCZO (Fig. B1). Samples from ERCZO also contain 6–10 wt.% smectite (Sme, identified as Na- montmorillonite (Kim et al., 2014)) and 0–2 wt.% kaolinite (Kln), while neither swelling minerals nor Kln were detected in the parent from SSHCZO (Jin et al., 2010) and samples from Fushan contain <2 wt.% swelling minerals (Fig. S6). Small amounts of OM, pyrite, apatite, Ti oxides, and zir- cons were detected by SEM-EDS in samples at all three sites, but we could not quantify them by XRD.

APPENDIX C. OBSERVATIONS ABOUT SULFUR

Pyrite is the primary sulfur S-bearing mineral identified by SEM-EDS in these shales, with minor occurrences of other sulfides (e.g., sphalerite, chalcopyrite) and rare sulfate (barite) minerals. Pyrite was generally observed as individual euhedral crystals and spheroidal aggregates of pyrite microcrystals, i.e., pyrite framboids (Fig. 3). As oxidation of pyrite and organic matter have been observed to be the deepest weathering reactions in shale (Littke et al., 1991; Chigira and Oyama, 2000; Bolton et al., 2006; Tuttle and Breit, 2009; Brantley et al., 2013; Jin et al., 2013; Lerouge et al., 2018), we define protolith as the zone that shows no pyrite nor organic matter depletion.

In shale samples from SSHCZO, ERCZO and Fushan, we measured total sulfur to infer pyrite concentration more accurately than is possible with other techniques such as XRD. Total S concentration can be detected as low as 0.04 wt.% by using a Leco Carbon/Sulfur Determinator. Although sulfur can also be present in organic matter (OM), OM was only present in relatively low concentrations in the parent shales. In this study we focus on rock chips that do not contain modern soil organic matter and thus we attributed all measured S to inorganic S in pyrite. The presence of very minor barite was observed in only one sample from Shale Hills, and thus did not affect this analysis.

Many lines of evidence suggest that S is present as pyrite and that it is depleted in the upper layers. For example, at all three sites, total sulfur is very low in near-surface rock chips. The samples of rock chips in SSHCZO and ERCZO from shallow depths contain, for example, at least 5-fold lower sulfur than the protolith (Table 2). In addition, pyrite was only observed consistently in SEM in samples from depths where no S depletion was detected. In contrast, in samples from depth intervals that were S-depleted, framboidal Fe (hydr)oxides were observed instead of framboidal pyrite (Fig. 3). The formation of framboidal Fe (hydr)oxides was thus attributed to pseudomorphic transformation of pyrite. For SSHCZO and ERCZO, the depth of S depletion was therefore used to define the regolith-protolith interface.

As discussed above and in the main text, no unequivocal sample of parent material from Fushan was recovered but framboidal Fe (hydr)oxides were observed under SEM in most Fushan shale samples (Fig. 3) and framboidal pyrite were observed in one outcrop sample (Fig. B2). Therefore, the Taiwan protolith was inferred to have contained pyrite framboids by analogy to SSHCZO and ERCZO, and the Fe (hydr)oxide framboids in the Fushan samples were inferred to have all been formed through pseudomorphic transformation. With the defensible assumption that the transformation must be isovolumetric because it was pseudomorphic, we estimated the original pyrite concentration in the protolith. Specifically, the area fractions of the Fe (hydr)oxide framboids in thin sections of the shale from outcrop (Fushan_FSR1) determined by ImageJ (Abramoff et al, 2004), observed equal to 0.1–0.2%, was inferred to equal the original pyrite concentration in protolith, i.e. 0.1–0.2% by volume or 0.1–0.2 wt.% as S. The only shale sample at Fushan containing measured S concentration higher than 0.01 wt.% was the sample from outcrop FSR6 (S: 0.63 wt.%, Table 3), and the amount of pyrite framboids (Fig. B2) observed under SEM in that sample was higher than the amount of pyrite/Fe (hydr)oxide framboids observed under SEM in all other samples from Fushan. Therefore, the high S concentration in that sample was presumed to not represent the whole watershed. Instead, we used a conservative estimation of S concentration in parent as 0.15 ± 0.05 wt.%. Because of the absence of S and the observed Fe (hydr)oxide framboids in all the shale samples at Fushan, we assumed, by analogy with the data from the other two sites, that all samples from drilled boreholes and soil pits were recovered from above the regolith-protolith interface.

APPENDIX D. SUPPLEMENTARY MATERIAL

Supplementary data to this article can be found online at https://doi.org/10.1016/j.gca.2019.09.044.

REFERENCES

Abramoff M. D., Magalhaes P. J. and Ram S. J. (2004) Image processing with Image J. *Biophotonics Intern.* 11, 36–42.

Atkinson B. K. (1984) Subcritical crack-growth in geological-materials. *J. Geophys. Res.* 89, 4077–4114.

Allen A. J. (1991) Time-resolved phenomena in cements, clays and porous rocks. *J. Appl. Crystallogr.* 24, 624–634.

Anders M. H., Laubach S. E. and Scholz C. H. (2014) Microfractures: A review. *J. Struct. Geol.* 69, 377–394.

Anderson S. P. (2019) Breaking it down: Mechanical processes in the weathering engine. *Elements* 15, 247–252.

Anderson S. P., Dietrich W. E. and Brimhall G. H. (2002) Weathering profiles, mass-balance analysis, and rates of solute loss: Linkages between weathering and erosion in a small, steep catchment. *Geol. Soc. Am. Bull.* 114, 1143–1158.

Anderson R. S., Rajaram H. and Anderson S. P. (2019) Climate driven coevolution of weathering profiles and hillslope topography generates dramatic differences in critical zone architecture. *Hydrol. Processes* 33, 4–19.

Anovitz L. M., Cole D. R., Rother G., Allard L. F., Jackson A. J. and Littrell K. C. (2013) Diagenetic changes in macro- to nanoscale porosity in the St. Peter Sandstone: An (ultra) small angle neutron scattering and backscattered electron imaging analysis. *Geochim. Cosmochim. Acta* 102, 280–305.

Anovitz L. M. and Cole D. R. (2015) Characterization and analysis of porosity and pore structures. *Rev. Mineral. Geochem.* 80, 61–164.

Aspandiar M. F. and Eggleton R. A. (2002) Weathering of chlorite: I. Reactions and products in microsystems controlled by the primary mineral. *Clays Clay Miner.* 50, 685–698.

Ayraud V., Aquilina L., Labasque T., Pauwels H., Molenat J., Pierson-Wickmann A. C., Durand V., Bour O., Tarits C., Le Corre P., Fourre E., Merot P. and Davy P. (2008) Compartmentalization of physical and chemical properties in hard-rock aquifers deduced from chemical and groundwater age analyses. *Appl. Geochem.* 23, 2686–2707.

Barker J. G., Glinka C. J., Moyer J. J., Kim M. H., Drews A. R. and Agamalian M. (2005) Design and performance of a thermal-neutron double-crystal diffractometer for USANS at NIST. *J. Appl. Cryst.* 38, 1004–1011.

Bazilevskaya E., Rother G., Mildner D. F. R., Pavich M., Cole D., Bhatt M. P., Jin L. X., Steefel C. I. and Brantley S. L. (2015) How oxidation and dissolution in diabase and granite control porosity during weathering. *Soil Sci. Soc. Am. J.* 79, 55–73.

Behrens R., Bouchez J., Schuessler J. A., Dultz S., Hewawasam T. and von Blanckenburg F. (2015) Mineralogical transformations set slow weathering rates in low-porosity metamorphic bedrock on mountain slopes in a tropical climate. *Chem. Geol.* 411, 283–298.

Bolton E. W., Berner R. A. and Petsch S. T. (2006) The weathering of sedimentary organic matter as a control on atmospheric O_2: II. Theoretical modeling. *Am. J. Sci.* 306, 575–615.

Bourg I. C. (2015) Sealing shales versus brittle shales: a sharp threshold in the material properties and energy technology uses of fine-grained sedimentary rocks. *Environ. Sci. Technol. Lett.* 2, 255–259.

Brantley S. L., Holleran M. E., Jin L. X. and Bazilevskaya E. (2013) Probing deep weathering in the Shale Hills Critical Zone Observatory, Pennsylvania (USA): the hypothesis of nested chemical reaction fronts in the subsurface. *Earth Surf. Processes Landforms* 38, 1280–1298.

Brantley S. L. and Lebedeva M. (2011) Learning to read the chemistry of regolith to understand the critical zone. *Annu. Rev. Earth Planet. Sci.* 39, 387–416.

Brantley S. L., Lebedeva M. I., Balashov V. N., Singha K., Sullivan P. L. and Stinchcomb G. (2017) Toward a conceptual model relating chemical reaction fronts to water flow paths in hills. *Geomorphology* 277, 100–117.

Brantley S. L. and White A. F. (2009) Approaches to modeling weathered regolith. *Rev. Mineral. Geochem.* 70, 435–484.

Brimhall G. H. and Dietrich W. E. (1987) Constitutive mass balance relations between chemical-composition, volume, density, porosity, and strain in metasomatic hydrochemical systems: results on weathering and pedogenesis. *Geochim. Cosmochim. Acta* 51, 567–587.

Chang, C.S., 2000. Study on the subsurface flow dynamics in the hyporheic zone of hapen creek. (Doctoral dissertation, Taiwan University).

Chigira M. (1990) A mechanism of chemical-weathering of mudstone in a mountainous area. *Eng. Geol.* 29, 119–138.

Chigira M. and Oyama T. (2000) Mechanism and effect of chemical weathering of sedimentary rocks. *Eng. Geol.* 55, 3–14.

Clift P. D., Lin A. T. S., Carter A., Wu F., Draut A. E., Lai T. H., Fei L. Y., Schouten H. and Teng L. (2008) Post-collisional collapse in the wake of migrating arc-continent collision in the Ilan Basin, Taiwan. In *SPE436: Formation and Applications of the Sedimentary Record in Arc Continent Collision Zones* (eds. A. E. Draut, P. D. Clift and D. W. Scholl). Geological Society of America, Boulder Co.

Comisky J. T., Newsham K., Rushing J. A. and Blasingame T. A. (2007) A comparative study of capillary-pressure-based empirical models for estimating absolute permeability in tight gas sands. *SPE Annual Technical Conference and Exhibition SPE, Anaheim, California, U.S.A.*

Dadson S. J., Hovius N., Chen H. G., Dade W. B., Hsieh M. L., Willett S. D., Hu J. C., Horng M. J., Chen M. C., Stark C. P., Lague D. and Lin J. C. (2003) Links between erosion, runoff variability and seismicity in the Taiwan orogen. *Nature* 426, 648–651.

Davy C. A., Skoczylas F., Barnichon J. D. and Lebon P. (2007) Permeability of macro-cracked argillite under confinement: Gas and water testing. *Phys. Chem. Earth.* 32, 667–680.

Debye P. and Bueche A. M. (1949) Scattering by an inhomogeneous solid. *J. Appl. Phys.* 20, 518.

Desbois G., Hohne N., Urai J. L., Besuelle P. and Viggiani G. (2017) Deformation in cemented mudrock (Callovo-Oxfordian Clay) by microcracking, granular flow and phyllosilicate plasticity: insights from triaxial deformation, broad ion beam polishing and scanning electron microscopy. *Solid Earth* 8, 291–305.

Eberl D. D. (2003) User's guide to RockJock – a program for determining quantitative mineralogy from powder X-ray diffraction data. *U.S. Geol. Survey, Open-file report*, 03–78.

Emberson R., Hovius N., Galy A. and Marc O. (2016) Chemical weathering in active mountain belts controlled by stochastic bedrock landsliding. *Nat. Geosci.* 9, 42–45.

Eppes M. C. and Keanini R. (2017) Mechanical weathering and rock erosion by climate-dependent subcritical cracking. *Rev. Geophys.* 55, 470–508.

Ferrier K. L. and Kirchner J. W. (2008) Effects of physical erosion on chemical denudation rates: A numerical modeling study of soil-mantled hillslopes. *Earth Planet. Sci. Lett.* 272, 591–599.

Fletcher R. C., Buss H. L. and Brantley S. L. (2006) A spheroidal weathering model coupling porewater chemistry to soil thicknesses during steady-state denudation. *Earth Planet. Sci. Lett.* 244, 444–457.

Fuller T. K., Perg L. A., Willenbring J. K. and Lepper K. (2009) Field evidence for climate-driven changes in sediment supply leading to strath terrace formation. *Geology* 37, 467–470.

Gabet E. J. and Mudd S. M. (2009) A theoretical model coupling chemical weathering rates with denudation rates. *Geology* 37, 151–154.

Gentier S., Billaux D. and van Vliet L. (1989) Laboratory testing of the voids of a fracture. *Rock Mech. Rock Eng.* 22, 149–157.

Glinka C. J., Barker J. G., Hammouda B., Krueger S., Moyer J. J. and Orts W. J. (1998) The 30 m small-angle neutron scattering instruments at the National Institute of Standards and Technology. *J. Appl. Cryst.* 31, 430–445.

Goodfellow B. W., Hilley G. E., Webb S. M., Sklar L. S., Moon S. and Olson C. A. (2016) The chemical, mechanical, and hydrological evolution of weathering granitoid. *J. Geophys. Res. Earth Surf.* 121, 1410–1435.

Gu X., Cole D. R., Rother G., Mildner D. F. R. and Brantley S. L. (2015) Pores in Marcellus shale: A neutron scattering and FIB-SEM study. *Energy Fuels* 29, 1295–1308.

Gu X. and Mildner D. F. R. (2016) Ultra-small-angle neutron scattering with azimuthal asymmetry. *J. Appl. Crystallogr.* 49, 934–943.

Gu X., Mildner D. F. R., Cole D. R., Rother G., Slingerland R. and Brantley S. L. (2016) Quantification of organic porosity and water accessibility in Marcellus shale using neutron scattering. *Energy Fuels* 30, 4438–4449.

Gu X. and Mildner D. F. R. (2018) Determination of porosity in anisotropic, fractal systems by neutron scattering. *J. Appl. Crystallogr.* 51, 175–184.

Harris W. G. and White G. N. (2008) X-ray diffraction techniques for soil mineral identification, in Methods of Soil Analysis Part 5—Mineralogical Methods. *Soc. Am. Book Ser.* 5, 81–115.

Hasenmueller E. A., Gu X., Weitzman J. N., Adams T. S., Stinchcomb G. E., Eissenstat D. M., Drohan P. J., Brantley S. L. and Kaye J. P. (2017) Weathering of rock to regolith: The activity of deep roots in bedrock fractures. *Geoderma* 300, 11–31.

Heap M. J., Baud P. and Meredith P. G. (2009) Influence of temperature on brittle creep in sandstones. *Geophys. Res. Lett.* 36, L19305.

Hinde A. L. (2004) PRINSAS - a Windows-based computer program for the processing and interpretation of small-angle scattering data tailored to the analysis of sedimentary rocks. *J. Appl. Crystallogr.* 37, 1020–1024.

Hren M. T., Hilley G. E. and Chamberlain G. P. (2007) The relationship between tectonic uplift and chemical weathering rates in the Washington cascades: Field measurements and model predictions. *Am. J. Sci.* 307, 1041–1063.

Hsu W. H., Byrne T. B., Ouimet W., Lee Y. H., Chen Y. G., van Soest M. and Hodges K. (2016) Pleistocene onset of rapid, punctuated exhumation in the eastern Central Range of the Taiwan orogenic belt. *Geology* 44, 719–722.

Jacobson A. D., Blum J. D., Chamberlain C. P., Craw D. and Koons P. O. (2003) Climatic and tectonic controls on chemical weathering in the New Zealand Southern Alps. *Geochim. Cosmochim. Acta* 67, 29–46.

Jen C. H., Lin J. C., Hsu M. L. and Petley D. N. (2006) Fluvial transportation and sedimentation of the Fu-shan small experimental catchments. *Quat. Int.* 147, 34–43.

Jones M. J. (1985) The weathered zone aquifers of the basement-complex areas of Africa. *Q. J. Eng. Geol.* 18, 35–46.

Jin L. X., Ravella R., Ketchum B., Bierman P. R., Heaney P., White T. and Brantley S. L. (2010) Mineral weathering and elemental transport during hillslope evolution at the Susquehanna/Shale Hills Critical Zone Observatory. *Geochim. Cosmochim. Acta* 74, 3669–3691.

Jin L. X., Rother G., Cole D. R., Mildner D. F. R., Duffy C. J. and Brantley S. L. (2011) Characterization of deep weathering and nanoporosity development in shale-A neutron study. *Am. Mineral.* 96, 498–512.

Jin L. X., Mathur R., Rother G., Cole D., Bazilevskaya E., Williams J., Carone A. and Brantley S. (2013) Evolution of porosity and geochemistry in Marcellus Formation black shale during weathering. *Chem. Geol.* 356, 50–63.

Katz A. J. and Thompson A. H. (1985) Fractal sandstone pores - implications for conductivity and pore formation. *Phys. Rev. Lett.* 54, 1325–1328.

Kim H., Bishop J. K. B., Dietrich W. E. and Fung I. Y. (2014) Process dominance shift in solute chemistry as revealed by long-term high-frequency water chemistry observations of groundwater flowing through weathered argillite underlying a steep forested hillslope. *Geochim. Cosmochim. Acta* 140, 1–19.

Kline S. R. (2006) Reduction and analysis of SANS and USANS data using Igor Pro. *J. Appl. Crystallogr.* 39, 895–900.

Kuila U. and Prasad M. (2013) Specific surface area and pore-size distribution in clays and shales. *Geophys. Prospect.* 61, 341–362.

Kuila U., McCarty D. K., Derkowski A., Fischer T. B. and Prasad M. (2014) Total porosity measurement in gas shales by the water immersion porosimetry (WIP) method. *Fuel* 117, 1115–1129.

Kuntz B. W., Rubin S., Berkowitz B. and Singha K. (2011) Quantifying solute transport at the Shale Hills Critical Zone Observatory. *Vadose Zone J.* 10, 843–857.

Larsen I. J., Almond P. C., Eger A., Stone J. O., Montgomery D. R. and Malcolm B. (2014) Rapid soil production and weathering in the southern Alps, New Zealand. *Science* 343, 637–640.

Lebedeva M. I., Fletcher R. C., Balashov V. N. and Brantley S. L. (2007) A reactive diffusion model describing transformation of bedrock to saprolite. *Chem. Geol.* 244, 624–645.

Lebedeva M. I., Fletcher R. C. and Brantley S. L. (2010) A mathematical model for steady-state regolith production at constant erosion rate. *Earth Surf. Processes Landforms* 35, 508–524.

Lebedeva M. I. and Brantley S. L. (2017) Weathering and erosion of fractured bedrock systems. *Earth Surf. Processes Landforms* 42, 2090–2108.

Legout C., Molenat J., Aquilina L., Gascuel-Odoux C., Faucheux M., Fauvel Y. and Bariac T. (2007) Solute transfer in the unsaturated zone-groundwater continuum of a headwater catchment. *J. Hydrol.* 332, 427–441.

Leith K., Moore J. R., Amann F. and Loew S. (2014) In situ stress control on microcrack generation and macroscopic extensional fracture in exhuming bedrock. *J. Geophys. Res. Solid Earth* 119, 594–615.

Lerouge C., Robinet J.-C., Debure M., Tournassat C., Bouchet A., Fernandez A. M., Flehoc C., Guerrot C., Kars M., Lagroix F., Landrein P., Made B., Negrel P., Wille G. and Claret F. (2018) A deep alteration and oxidation profile in a shallow clay aquitard: example of the Tegulines Clay, East Paris Basin, France. *Geofluids*.

Lin K.-C., Horng F.-W., Cheng W.-E., Chiang H.-C. and Chang U.-C. (1996) Soil survey and classification of the Fushan Experimental Forest. *Taiwan J. For. Sci.* 11, 159–174.

Lin M. L., Lin C. K. and You M. J. (2001) Vitrinite reflectance as a possible indicator of metamorphic grade and stratigraphic position of formations: a study of Oligocene metapelites in NE Taiwan. *J. Asian Earth Sci.* 19, 223–232.

Lin T.-C., Hamburg S. P., Lin K.-C., Wang L.-J., Chang C.-T., Hsia Y.-J., Vadeboncoeur M. A., McMullen C. M. M. and Liu C.-P. (2011) Typhoon disturbance and forest dynamics: Lessons from a northwest Pacific subtropical forest. *Ecosystems* 14, 127–143.

Littke R., Klussmann U., Krooss B. and Leythaeuser D. (1991) Quantification of loss of calcite, pyrite, and organic-matter due to weathering of toarcian black shales and effects on kerogen and bitumen characteristics. *Geochim. Cosmochim. Acta* 55, 3369–3378.

Ma L., Chabaux F., Pelt E., Blaes E., Jin L. X. and Brantley S. (2010) Regolith production rates calculated with uranium-series isotopes at Susquehanna/Shale Hills Critical Zone Observatory. *Earth Planet. Sci. Lett.* 297, 211–225.

Ma L., Chabaux F., West N., Kirby E., Jin L. X. and Brantley S. (2013) Regolith production and transport in the Susquehanna

Shale Hills Critical Zone Observatory, Part 1: Insights from U-series isotopes. *J. Geophys. Res. Earth Surf.* 118, 722–740.

Maher K. and Chamberlain C. P. (2014) Hydrologic regulation of chemical weathering and the geologic carbon cycle. *Science* 343, 1502–1504.

Merritts D. and Bull W. B. (1989) Interpreting Quaternary uplift rates at the Mendocino triple junction, northern California, from uplifted marine terraces. *Geology* 17, 1020–1024.

Meunier A., Sardini P., Robinet J. C. and Pret D. (2007) The petrography of weathering processes: facts and outlooks. *Clay Miner.* 42, 415–435.

Mildner D. F. R. and Hall P. L. (1986) Small-angle scattering from porous solids with fractal geometry. *J. Phys. D: Appl. Phys.* 19, 1535–1545.

Minasny B., McBratney A. B. and Salvador-Blanes S. (2008) Quantitative models for pedogenesis – A review. *Geoderma* 144, 140–157.

Molnar P., Anderson R. S. and Anderson S. P. (2007) Tectonics, fracturing of rock, and erosion. *J. Geophys. Res. Earth Surf.* 112, F03014.

Moon S., Perron J. T., Martel S. J., Holbrook W. S. and St. Clair J. (2017) A model of three-dimensional topographic stresses with implications for bedrock fractures, surface processes, and landscape evolution. *J. Geophys. Res. Earth Surf.* 122, 823–846.

Morin R. H., Carleton G. B. and Poirier S. (1997) Fractured-aquifer hydrogeology from geophysical logs; The Passaic Formation, New Jersey. *Ground Water* 35, 328–338.

Nadan B. J. and Engelder T. (2009) Microcracks in New England granitoids: A record of thermoelastic relaxation during exhumation of intracontinental crust. *Geol. Soc. Am. Bull.* 121, 80–99.

Navarre-Sitchler A. K., Cole D. R., Rother G., Jin L. X., Buss H. L. and Brantley S. L. (2013) Porosity and surface area evolution during weathering of two igneous rocks. *Geochim. Cosmochim. Acta* 109, 400–413.

Navarre-Sitchler A., Brantley S. L. and Rother G. (2015) How porosity increases during incipient weathering of crystalline silicate rocks. *Rev. Mineral. Geochem.* 80, 331–354.

Nelson P. H. (2009) Pore-throat sizes in sandstones, tight sandstones, and shales. *AAPG Bull.* 93, 329–340.

Nishiyama T. and Kusuda H. (1994) Identification of pore spaces and microcracks using fluorescent resins. *Int. J. Rock Mech. Min. Sci. Geomech. Abstr.* 31, 369–375.

Ougier-Simonin A., Renard F., Boehm C. and Vidal-Gilbert S. (2016) Microfracturing and microporosity in shales. *Earth Sci. Rev.* 162, 198–226.

Oyama T. and Chigira M. (1999) Weathering rate of mudstone and tuff on old unlined tunnel walls. *Eng. Geol.* 55, 15–27.

Pavich M. J. (1986) Processes and rates of saprolite production and erosion on a foliated granitic rock of the Virginia Piedmont. In *Rates of chemical weathering of rocks and minerals* (eds. S. M. Colman and D. P. Dethier). Rates of chemical weathering of rocks and minerals. Academic Press Orlando, FL, pp. 551–590.

Pearson F. J. (1999) What is the porosity of a mudrock? *Geol. Soc. London Spec. Publ.* 158, 9–21.

Radlinski A. P., Ioannidis M. A., Hinde A. L., Hainbuchner M., Baron M., Rauch H. and Kline S. R. (2004) Angstrom-to-millimeter characterization of sedimentary rock microstructure. *J. Colloid Interface Sci.* 274, 607–612.

Radlinski A. P. (2006) Small-angle neutron scattering and the microstructure of rocks. *Rev. Mineral. Geochem.* 63, 363–397.

Rempe D. M. and Dietrich W. E. (2014) A bottom-up control on fresh-bedrock topography under landscapes. *Proc. Natl. Acad. Sci. USA* 111, 6576–6581.

Rempe D. M. (2016) *Controls on critical zone thickness and hydrologic dynamics at the hillslope scale (Doctoral dissertation*. University of California, Berkeley).

Rempe D. M. and Dietrich W. E. (2018) Direct observations of rock moisture, a hidden component of the hydrologic cycle. *Proc. Natl. Acad. Sci. USA* 115, 2664–2669.

Rich C. I. (1968) Hydroxy interlayers in expansible layer silicates. *Clays Clay Miner.* 16, 15–30.

Riebe C. S., Kirchner J. W., Granger D. E. and Finkel R. C. (2001) Strong tectonic and weak climatic control of long-term chemical weathering rates. *Geology* 29, 511–514.

Riebe C. S., Kirchner J. W. and Finkel R. C. (2003) Long-term rates of chemical weathering and physical erosion from cosmogenic nuclides and geochemical mass balance. *Geochim. Cosmochim. Acta* 67, 4411–4427.

Riebe C. S., Hahm W. J. and Brantley S. L. (2017) Controls on deep critical zone architecture: a historical review and four testable hypotheses. *Earth Surf. Processes Landforms* 42, 128–156.

Roden M. K. and Miller D. S. (1989) Apatite fission-track thermochronology of the Pennsylvania Appalachian Basin. *Geomorphology* 2, 39–51.

Rossi A. M. and Graham R. C. (2010) Weathering and porosity formation in subsoil granitic clasts, Bishop Creek Moraines, California. *Soil Sci. Soc. Am. J.* 74, 172–185.

Salve R., Rempe D. M. and Dietrich W. E. (2012) Rain, rock moisture dynamics, and the rapid response of perched groundwater in weathered, fractured argillite underlying a steep hillslope. *Water Resour. Res.* 48, W11528.

Savin S. M. and Epstein S. (1970) The oxygen and hydrogen isotope geochemistry of clay minerals. *Geochim. Cosmochim. Acta* 34, 25–42.

Siame L. L., Angelier J., Chen R. F., Godard V., Derrieux F., Bourles D. L., Braucher R., Chang K. J., Chu H. T. and Lee J. C. (2011) Erosion rates in an active orogen (NE-Taiwan): A confrontation of cosmogenic measurements with river suspended loads. *Quat. Geochronol.* 6, 246–260.

Slim M., Perron J. T., Martel S. J. and Singha K. (2015) Topographic stress and rock fracture: a two-dimensional numerical model for arbitrary topography and preliminary comparison with borehole observations. *Earth Surf. Processes Landforms* 40, 512–529.

Spotila J. A., Bank G. C., Reiners P. W., Naeser C. W., Naeser N. D. and Henika B. S. (2004) Origin of the Blue Ridge escarpment along the passive margin of Eastern North America. *Basin Res.* 16, 41–63.

Stallard R. F. (1995) Tectonic, environmental, and human aspects of weathering and erosion: A global review using a steady-state perspective. *Annu. Rev. Earth Planet. Sci.* 23, 11–39.

Stallard R. F. and Edmond J. M. (1983) Geochemistry of the Amazon: 2. the influence of geology and weathering environment on the dissolved load. *J. Geophys. Res.* 88, 9671–9688.

St Clair J., Moon S., Holbrook W. S., Perron J. T., Riebe C. S., Martel S. J., Carr B., Harman C., Singha K. and Richter D. D. (2015) Geophysical imaging reveals topographic stress control of bedrock weathering. *Science* 350, 534–538.

Sullivan P. L., Hynek S. A., Gu X., Singha K., White T., West N., Kim H., Clarke B., Kirby E., Duffy C. and Brantley S. L. (2016) Oxidative dissolution under the channel leads geomorphological evolution at the shale hills catchment. *Am. J. Sci.* 316, 981–1026.

Ten Cate J. A. and Shankland T. J. (1996) Slow dynamics in the nonlinear elastic response of Berea sandstone. *Geophys. Res. Lett.* 23, 3019–3022.

Thompson A. H., Katz A. J. and Krohn C. E. (1987) The microgeometry and transport properties of sedimentary rock. *Adv. Phys.* 36, 625–694.

Torres M. A., West A. J., Clark K. E., Paris G., Bouchez J., Ponton C., Feakins S. J., Galy V. and Adkins J. F. (2016) The acid and alkalinity budgets of weathering in the Andes-Amazon system: Insights into the erosional control of global biogeochemical cycles. *Earth Planet. Sci. Lett.* 450, 381–391.

Tuttle M. L. W. and Breit G. N. (2009) Weathering of the New Albany Shale, Kentucky, USA: I. Weathering zones defined by mineralogy and major-element composition. *Appl. Geochem.* 24, 1549–1564.

von Blanckenburg F., Hewawasam T. and Kubik P. W. (2004) Cosmogenic nuclide evidence for low weathering and denudation in the wet, tropical highlands of Sri Lanka. *J. Geophys. Res. Earth Surf.* 109, F03008.

Waza T., Kurita K. and Mizutani H. (1980) The effect of water on the subcritical crack-growth in silicate rocks. *Tectonophysics* 67, 25–34.

Weaver C. E. (1955) The distribution and identification of mixed-layer clays in sedimentary rocks. *Clays Clay Miner.* 4, 385–386.

Wells T., Binning P. and Willgoose G. (2005) The role of moisture cycling in the weathering of a quartz chlorite schist in a tropical environment: findings of a laboratory simulation. *Earth Surf. Processes Landforms* 30, 413–428.

West A. J., Galy A. and Bickle M. (2005) Tectonic and climatic controls on silicate weathering. *Earth Planet. Sci. Lett.* 235, 211–228.

West A. J. (2012) Thickness of the chemical weathering zone and implications for erosional and climatic drivers of weathering and for carbon-cycle feedbacks. *Geology* 40, 811–814.

West N., Kirby E., Bierman P., Slingerland R., Ma L., Rood D. and Brantley S. (2013) Regolith production and transport at the Susquehanna Shale Hills Critical Zone Observatory, Part 2: Insights from meteoric Be-10. *J. Geophys. Res. Earth Surf.* 118, 1877–1896.

West N., Kirby E., Bierman P. and Clarke B. A. (2014) Aspect-dependent variations in regolith creep revealed by meteoric Be-10. *Geology* 42, 507–510.

White A. F. and Blum A. E. (1995) Effects of climate on chemical-weathering in watersheds. *Geochim. Cosmochim. Acta* 59, 1729–1747.

White A. F., Bullen T. D., Schulz M. S., Blum A. E., Huntington T. G. and Peters N. E. (2001) Differential rates of feldspar weathering in granitic regoliths. *Geochim. Cosmochim. Acta* 65, 847–869.

White A. F., Schulz M. S., Vivit D. V., Blum A. E., Stonestrom D. A. and Anderson S. P. (2008) Chemical weathering of a marine terrace chronosequence, Santa Cruz, California I: Interpreting rates and controls based on soil concentration-depth profiles. *Geochim. Cosmochim. Acta* 72, 36–68.

Worthington S. R. H., Davies G. J. and Alexander E. C. (2016) Enhancement of bedrock permeability by weathering. *Earth Sci. Rev.* 160, 188–202.

Yesavage T., Fantle M. S., Vervoort J., Mathur R., Jin L. X., Liermann L. J. and Brantley S. L. (2012) Fe cycling in the Shale Hills Critical Zone Observatory, Pennsylvania: An analysis of biogeochemical weathering and Fe isotope fractionation. *Geochim. Cosmochim. Acta* 99, 18–38.

Zachara J., Brantley S., Chorover J., Ewing R., Kerisit S., Liu C. X., Perfect E., Rother G. and Stack A. G. (2016) Internal domains of natural porous media revealed: critical locations for transport, storage, and chemical reaction. *Environ. Sci. Technol.* 50, 2811–2829.

Zhang C. L. and Rothfuchs T. (2008) Damage and sealing of clay rocks detected by measurements of gas permeability. *Phys. Chem. Earth.* 33, S363–S373.

Associate Editor: Christophe Tournassat